HEAT TRANSFER AND MICROSTRUCTURE DURING THE EARLY STAGES OF SOLIDIFICATION OF METALS

By

Cornelius Anaedu Muojekwu

B.Sc., The University of Ife, Nigeria, 1987
M.Sc., The University of Lagos, Nigeria, 1990

A THESIS SUBMITTED IN PARTIAL FULFILLMENT OF
THE REQUIREMENTS FOR THE DEGREE OF
MASTER OF APPLIED SCIENCE (M.A.Sc.)
in

THE FACULTY OF GRADUATE STUDIES
DEPARTMENT OF METALS AND MATERIALS
ENGINEERING

We accept this thesis as conforming

to the required standard

THE UNIVERSITY OF BRITISH COLUMBIA
July 1993

© Cornelius Anaedu Muojekwu, 1993

In presenting this thesis in partial fulfilment of the requirements for an advanced degree at the University of British Columbia, I agree that the Library shall make it freely available for reference and study. I further agree that permission for extensive copying of this thesis for scholarly purposes may be granted by the head of my department or by his or her representatives. It is understood that copying or publication of this thesis for financial gain shall not be allowed without my written permission.

(Signature)

Department of Metals & Materials Engineering

The University of British Columbia
Vancouver, Canada

Date July 22 1993

DE-6 (2/88)

ABSTRACT

The future of solidification processing clearly lies not only in elucidating the various aspects of the subject, but also in synthesizing them into unique qualitative and quantitative models. Ultimately, such models must predict and control the cast structure, quality and properties of the cast product for a given set of conditions. Linking heat transfer to cast structure is an invaluable aspect of a fully predictive model, which is of particular importance for near-net-shape casting where the product reliability and application are so dependent on the solidification phenomena.

This study focused on the characterization of transient heat transfer at the early stages of solidification and the consequent evolution of the secondary dendrite arm spacing. Water-cooled chills instrumented with thermocouples were dipped into melts of known superheats such that unidirectional solidification was achieved. An inverse heat transfer model based on the sequential regularization technique was used to predict the interfacial heat flux and surface temperature of the chill from the thermocouple measurements. These were then used as boundary conditions in a 1-D solidification model of the casting. The secondary dendrite arm spacing (SDAS) at various locations within the casting was computed with various semi-empirical SDAS models. The predictions were compared with experimental measurements of shell thickness and secondary dendrite arm spacing from this work as well as results reported in the literature. The effects of superheat, alloy composition, chill material, surface roughness and surface film (oil) were investigated.

The results indicate that the transient nature of the interface heat transfer between the chill and casting exerts the greatest influence in the first few seconds of melt-mold contact. The interfacial heat flux and heat transfer coefficient exhibited the typical trend common to solidification where the initial contact between mold and melt is followed by a steadily growing gap. Both parameters increase steeply upon contact up to a peak value at a short duration (< 10

s), decrease sharply for a few seconds and then gradually decline to a fairly steady value. Heat transfer at the interface increased with increasing mold diffusivity, increasing superheat, decreasing thermal resistance of the interfacial gap, increasing thermal expansion of the mold, decreasing shrinkage of the casting alloy, decreasing mold thickness and initial temperature, and decreasing mold surface roughness. The secondary dendrite arm spacing decreased with increasing heat flux for the same alloy system and depended on the cooling rate and local solidification time. The secondary dendrite arm spacing was also found to be a direct function of the heat transfer coefficient at distances very near the casting/mold interface.

A three stage empirical heat flux model based on the thermophysical properties of the mold and casting was proposed for the simulation of the mold/casting boundary condition during solidification. The applicability of the various models relating secondary dendrite arm spacing to heat transfer parameters was evaluated and the extension of these models to continuous casting processes was pursued.

Table of Contents

ABSTRACT ii

Table of Contents iv

Table of Tables vii

Table of Figures viii

Nomenclature xi

Acknowledgement xviii

Chapter 1 INTRODUCTION 1

1.1 Fundamentals Of Solidification Processing. 1

1.2 Heat and Fluid Flow During Solidification 4

1.3 Microstructural Evolution during Solidification. 7

1.3.1 Nucleation 7

1.3.2 Dendritic Growth 8

Chapter 2 LITERATURE SURVEY 12

2.1 Solidification Modeling 12

2.2 Heat Flow - Interface Resistance 14

2.3 Heat Flow - Latent Heat Evolution 21

2.3.1 Temperature Recovery Method 24

2.3.2 Specific Heat Method 25

2.3.3 Enthalpy Methods 27

2.3.4 Latent Heat Method 28

2.3.5 The Nature of Latent Heat Evolution 29

2.3.5.1 Cooling Curve Analysis 30

2.4 Fluid Flow During Solidification 33

2.5 Microstructural Evolution 34

2.5.1 Nucleation 35

2.5.2 Growth 37

2.5.2.1 Dendrite Arm Spacing and Coarsening 42

2.6 Coupling Heat Transfer and Microstructural Evolution 50

2.6.1 Complete Mixing Models 51

2.6.2 Solute Diffusion Models 51

Chapter 3 SCOPE AND OBJECTIVES 54

3.1 Objectives/Importance 54

3.2 Methodology 55

Chapter 4 EXPERIMENTAL PROCEDURE AND RESULTS 58

4.1 Design 58

4.2 Instrumentation and Data Acquisition 62

4.3 Dipping Campaigns 63

4.3.1 Thermal Response of the Thermocouples 67

4.4 Metallographic Examination 72

Chapter 5 MATHEMATICAL MODELING 80

5.1 Chill Heat Flow Model 80

5.2 Casting Heat Flow Model 83

5.2.1 Latent Heat Evolution and Fraction Solid 88

5.3 Dendrite Arm Spacing (DAS) Models 90

5.4 Sensitivity Analysis And Model Validation 91

Chapter 6 RESULTS AND DISCUSSION 96

6.1 Heat Flow 96

6.2 Microstructure Formation 101

6.3 Effect of Process Variables 105

6.3.1 Effect of Surface Roughness 105

6.3.2 Effect of Chill Material 109

6.3.3 Effect of Superheat 113

6.3.4 Effect of Alloy Composition 118

6.3.5 Effect of Oil Film 123

6.3.6 Effect of Bath Height 129

6.4 Proposed Empirical Model 132

6.5 Implications for Continuous and Near-Net-Shape Casting 138

Chapter 7 SUMMARY AND CONCLUSIONS/RECOMMENDATIONS 142

REFERENCES 146

APPENDIX A 158

Table of Tables

Table 2.1 Various expressions for heat transfer coefficient 17

Table 2.2 Various expressions for primary dendrite arm spacing 45

Table 2.3 Various expressions for secondary dendrite arm spacing 47

Table 2.4 Complete mixing models for the evaluation of solid fraction 52

Table 4.1 Some details of the experimental design 60

Table 4.2 Thermocouple calibration in boiling water 63

Table 4.3 Properties of the oils used in the experiments 65

Table 4.4 Measured thermocouple response 67

Table 4.5 Typical secondary dendrite arm spacing measurement 75

Table 5.1 Thermophysical Properties Used in the Chill Model 83

Table 5.2 Thermophysical Properties Used in the Casting Model 86

Table 5.3 Input and recalculated interfacial heat flux 94

Table 6.1 Measured and predicted secondary dendrite arm spacing 103

Table 6.2 Measured shell surface roughness for various chill surface microprofiles .. 106

Table 6.3 Measured shell surface roughness for various chill materials 110

Table 6.4 Measured shell surface roughness for various superheats 118

Table 6.5 Measured shell surface roughness for different alloy compositions 120

Table 6.6 Measured shell surface roughness for the four oils 127

Table 6.7 Measured shell surface roughness for different bath heights 129

Table of Figures

Fig. 1.1 Inter-relationship between microstructure and other process variables 4

Fig. 1.2 Schematic diagram of the casting/mold interface 6

Fig. 1.3 Schematic representation of dendritic growth 11

Fig. 2.1 Process understanding and improvement with the aid of modeling 13

Fig. 2.2 Typical variation of heat transfer coefficient with time 19

Fig. 2.3 Variation of interfacial heat flux with time 21

Fig. 2.4 Handling phase change in solidification modeling 23

Fig. 2.5 Variation of specific heat with temperature during solidification 27

Fig. 2.6 Variation of enthalpy with temperature 29

Fig. 2.7 Growth phenomena during solidification 39

Fig. 2.8 Various dendrite coarsening models 44

Fig. 3.1 Schematic illustration of the project methodology 57

Fig. 4.1 Schematic representation of the experimental set-up 59

Fig. 4.2 Operating thermal resistances 61

Fig. 4.3 Variation of the thermal resistances with time 62

Fig. 4.4 Schematic representation of surface microprofile 64

Fig. 4.5 Typical temperature data during casting 68

Fig. 4.6 Effect of surface roughness on measured temperature 69

Fig. 4.7 Effect of chill material on measured temperature 69

Fig. 4.8 Effect of superheat on measured temperature 70

Fig. 4.9 Effect of alloy composition on measured temperature 70

Fig. 4.10 Effect of oil film on measured temperature 71

Fig. 4.11 Effect of bath height on measured temperature 71

Fig. 4.12 Typical micrographs of Al-7%Si alloy 73

Fig. 4.13 Typical measured secondary dendrite arm spacing (SDAS) 76
Fig. 4.14 Effect of surface roughness on measured SDAS 76
Fig. 4.15 Effect of chill material on measured SDAS 77
Fig. 4.16 Effect of super heat on measured SDAS 77
Fig. 4.17 Effect of alloy composition on measured SDAS 78
Fig. 4.18 Effect of oil film on measured SDAS 78
Fig. 4.19 Effect of bath height on measured SDAS 79
Fig. 5.1 Discretization of chill and casting 82
Fig. 5.2 Computer implementation of the models 87
Fig. 5.3 Zones in the effective specific heat method 89
Fig. 5.4 Calculated and measured temperature profiles in the chill 92
Fig. 5.5 Analytical and numerical solutions of infinite slab assumption 93
Fig. 5.6 Calculated and measured temperature profiles in the casting 95
Fig. 5.7 Calculated and measured shell thickness 95
Fig. 6.1 Model predictions - interfacial heat flux and heat transfer coefficient 97
Fig. 6.2 Model predictions - shell thickness and interfacial gap 98
Fig. 6.3 Calculated surface temperature profiles for chill and casting 99
Fig. 6.4 Calculated and measured secondary dendrite arm spacing 104
Fig. 6.5 Effect of surface roughness on heat transfer 107
Fig. 6.6 Effect of surface roughness on solidification and microstructure 108
Fig. 6.7 Effect of chill material on heat transfer 111
Fig. 6.8 Effect of chill material on solidification and microstructure 112
Fig. 6.9 Variation of the chill thermal resistance with time 113
Fig. 6.10 Effect of superheat on heat transfer 116
Fig. 6.11 Effect of superheat on solidification and microstructure 117

Fig. 6.12 Effect of alloy composition on heat transfer 121

Fig. 6.13 Effect of alloy composition on solidification and microstructure 122

Fig. 6.14 Effect of oil film on heat transfer 124

Fig. 6.15 Effect of oil film on solidification and microstructure 125

Fig. 6.16 Surface temperatures of the chill and casting with the oils 126

Fig. 6.17 Effect of bath height on heat transfer 130

Fig. 6.18 Effect of bath height on solidification and microstructure 131

Fig. 6.19 Proposed empirical heat flux model 133

Fig. 6.20 Variation of peak heat flux with some process variables 135

Fig. 6.21 Variation of peak heat flux with other process variables 136

Fig. 6.22 Casting simulation with the empirical model for Al-7%Si 137

Fig. 6.23 Casting simulation with the empirical model for Al-3%Cu-4.5%Si 137

Fig. 6.24 Empirical model applied to twin-roll casting of 0.8%C steel 140

Fig. 1A Schematic illustration of IHCP methods 159

Fig. 2A Schematic illustration of future time assumption 161

Fig. 3A Flow diagram of the sequential IHCP technique 163

NOMENCLATURE

a, a_0, A	constants
a	half width (horizontal) of a V-groove in Table 2.1, m
A	area in Eq. (2.18), m^2
b, b_0, B	constants
Bi	Biot number = hl_c/k
$c, C_0, C_1, \ldots C_{11}$	constants
$c_\alpha, c_e, c_i, c_\gamma, c_0$	composition, %
C_{eff}	effective specific heat capacity, J/Kg.K
C_p	specific heat capacity, J/Kg.K
C_{pseudo}	pseudo specific heat capacity, J/Kg.K
d, d_0	constants
D	diffusion coefficient, m^2/s
DAS	dendrite arm spacing, μm
e, e_0	constants
Fo	Fourier number = $\alpha t/x^2$ for heat conduction or Dt/x^2 for diffusion, m^2/s
f_l	liquid fraction
f_s	solid fraction
g	gravitational acceleration, m^2/s
G	thermal gradient, °C/m
ΔG_A	diffusional activation energy for growth, J
G_c	solute gradient, m^{-1}
ΔG_c^{het}	energy of formation of the critical nucleus, J
G^*	lumped material parameter

h	heat transfer coefficient, $W/m^2.K$
h'	empirical constant in Table 2.1
H	enthalpy, J/kg
H_v	Vickers hardness of the softer solid in a contacting interface in Table 2.1
k	thermal conductivity, W/m.K
k_b	Boltzmann constant in Eq. (2.31) = 1.38054×10^{-23} J/K
k_p	partition coefficient
K	solidification constant in the parabolic shell growth expression, $m/s^{1/2}$
K_1, K_2, K_3, K_4	empirical constants in Eqs. (2.32) and (2.33)
l	length, m
l_c	characteristic length (Volume/Area), m
L	latent heat, J/Kg
L_c	coefficient of thermal contraction for the casting, mm/m
L_m	coefficient of linear thermal expansion for the mold, mm/m
L_v	volumetric latent heat, J/m^3
m	liquidus slope from the phase diagram, K/%
ns	number of temperature sensors
n'	number of surface atoms of the substrate per unit volume of liquid, $atoms/m^3$
N	nucleated particle density, $particles/m^3$
N	number of nodes in Eq. (5.7)
N_s	original heterogeneous substrate density, $substrates/m^3$
Nu	Nusselt number = hl_c/k_f
P	pressure, N/m^2
Pe	Peclet Number = vr/D

Pr	Prandtl Number = α/μ
q	heat flux, W/m^2
Q'	rate of latent heat release, W/m^2
r	radius, m
r	number of future time steps in Appendix A
r^*	radius of critical nucleeus, m
R	growth rate, m/s
R	thermal resistance in Fig. 4.2, $m^2.K/W$
Ra	surface roughness, μm
Re	Reynolds Number = $\rho\ u\ l_c/\mu$
S	shell thickness, m
S_1, S_2	temperature jump distance, m
SC	sensitivity coefficient
S_L	least square function
T	temperature, °C
TC	calculated temperature, °C
TM	measured temperature, °C
T_p	pouring or teeming temperature, °C
$T\uparrow$	temperature of a point midway between a node and the succeeding node, °C
$T\downarrow$	temperature of a point midway between a node and the preceding node, °C
t	time, s
t_f	local solidification time, s
u	velocity along the x-axis, m/s

v	velocity along the y-axis, m/s
V	volume, Kg/m^3
$Vf1$, $Vf2$	volume fractions
w	velocity along the z-axis, m/s
x	distance along the x-axis, m
x_r	distance between roughness peaks of the rougher surface at an interface in Table 2.1
X	chill thickness, m
y	distance along the y-axis, m
z	distance along the z-axis, m
α	thermal diffusivity, m^2/s
β	constant
ε	thermal emissivity
γ	interfacial energy, N/m
Γ	Gibbs-Thomson coefficient, K.m
λ_1	primary dendrite arm spacing, μm
λ_2	secondary dendrite arm spacing, μm
μ	dynamic viscosity, Kg/m.s
μ_2	nucleation constant, $m^{-3}.K^{-2}$
π	22/7
ρ	density, Kg/m^3
σ	Stefan-Boltzmann constant = 5.669×10^{-8} $W/m^2.K^4$
θ	angle between the vertical and the gap region of a V-groove in contact with a melt, $^\circ$

Θ	inverse of the time constant $(\frac{hA}{\rho V C_p})$, s^{-1}
ζ	constant

Subscripts

c	relating to casting
c	relating to capillarity in Eq. (2.40)
c	relating to the critical value in Table 2.2
cc	relating to cooling curve
ch	relating to the chill
ch/c	relating to chill/casting interface
chs	relating chill surface
cs	relating to casting surface
e	relating to eutectic
eff	relating to an effective value
eq	relating to an equivalent value
f	relating to cooling fluid
g	relating to the interfacial gap
i	generic index for item or point
k	relating to kinetics in Eq. (2.40)
l	relating to the liquid
L	relating to the liquidus
max	relating to the maximum value
n	relating to the nucleus
0	relating to the initial or original value
r	relating to radiation in Eq. (2.3)

s	relating to solid
s	relating the solute in Eq. (2.40)
S	relating to the solidus
shell	relating to the solidified shell
sl	relating to solid/liquid interface
t	relating to the dendrite tip
t	relating to thermal in Eq. (2.40)
x	relating to the x-axis
y	relating to the y-axis
z	relating to the z-axis
zc	relating to the zero curve in Eq. (2.19)
α	relating to ferrite
γ	relating to austenite
∞	relating to the ambient or surrounding

Supercripts

a	exponent in Eq. (6.4)
b	exponent in Table 2.1 and Eq. (6.4)
c	exponent in Eq. (6.4)
d	exponent in Eq. (6.5)
e	exponent in Eq. (6.5)
f	exponent in Eq. (6.5)
i	time index in Appendix A (i=1,2,.....r)
j	space index in Appendix A (j=1,2,....ns)
m	time index for estimating heat flux (m=1,2.....t_T)
n	relating to the n'th time

$n_1, n_2, \ldots\ldots\ldots, n_8$	exponents
x	exponent in Eq. (2.27)
y	exponent in Eq. (2.27)

Acknowledgement

I would like to dedicate this work to the late Dr. P.E. Anagbo whose encouragement and assistance were instrumental to my studies at U.B.C., and to my CREATOR who has been making my life a continuing miracle.

My gratitude goes to my supervisors, Dr. I.V. Samarasekera and Dr. J.K. Brimacombe, for their invaluable counsel and for providing the research assistantship that supported this study. The CONTA IHCP code provided by Dr. J.V. Beck is gratefully acknowledged. I also acknowledge the assistance of Neil Walker, Peter Musil and other MMAT technical staff in carrying out this research. My appreciation goes to my family, my friends and colleagues for their priceless support and solidarity.

Cornelius Anaedu Muojekwu

July 1993

Chapter 1

INTRODUCTION

1.1 Fundamentals Of Solidification Processing.

Solidification can be defined as the transformation from a liquid phase to a solid phase or phases. The phenomena associated with the process of solidification are complex and varied. It is especially difficult to conceive of the initial stages of the process, when the first crystals or center of crystallization appears. Genders[1] proposed his solidification theory in 1926 but it was Chalmers et al.[2] that later attempted to offer a comprehensive qualitative and quantitative understanding of this theory.

Chalmers and co-workers considered the instantaneous structure of liquid near its melting point as one in which each atom is part of a "crystal-like cluster or micro-volume", orientated randomly and with "free space" between it and its neighboring clusters. These clusters would form and disperse very quickly through the transfer of atoms from one to another by movement across the intervening free space. With reference to the extensive thermodynamics work of Gibbs[3], they conceived of the possibility of clusters of all possible structures existing in the liquid near its melting point, such that those of lowest free energies become more stable and are favoured during nucleation. While each atom in the liquid is at a free energy minimum, these minima are nonetheless higher than those of the solid during nucleation. This accounts for the evolution of the latent heat of fusion. So long as the clusters are below a certain critical size (embryo) corresponding to the liquidus temperature, they cannot grow and no tangible solid is formed. However, if the thermal condition is such that the critical size is less than the largest cluster size, then nucleation occurs and the supercritical clusters (now nuclei) grow into crystals.

The above consideration formed the basis of the usual conception of solidification as a dual process of *nucleation* and *growth*. Ever since, solidification phenomena have been studied from three major perspectives:

1. Atomic Level; usually dominated by the atomic processes by which nucleation and growth occurs. Emphasis has been on atomic sites (crystal structure), nucleation type and rate, atomic defects etc.

2. Microscopic Level; dominated by microstructural evolution and growth. Such topics as phases and microstructures, interfacial phenomena, growth pattern, grain size and density, microscopic defects, etc, have been studied.

3. Macroscopic Level; where the flow of liquid metal and the extraction of heat from the solidifying casting predominate. Emphasis has been on fluid flow and heat transfer, macrostructure, shell thickness and pool profile, surface characteristics, shape, macroscopic defects, stress distribution, etc.

Solidification modeling based exclusively on any of these three levels is important, but an integrated approach that couples the different levels will be an invaluable tool for the optimization of the solidification process. As far back as 1964, Chalmers[2] recognized this when he noted in the preface to his book; "Principles Of Solidification", that the rapid progress made in elucidating the various separate aspects of solidification has not been matched by application of this knowledge to the problems encountered in industry. Of course, substantial progress has since been made in terms of application of solidification knowledge but the pool of knowledge remains so distant from application.

It is strongly believed, therefore, that the future of solidification processing and modeling lies not only in understanding the various aspects of the subject, but also in coupling most of the different approaches and models into some uniquely comprehensive, qualitative and

quantitative packages. Such packages must allow for extensive prediction and control of structure, quality and properties of the solidified product, once the solidification conditions and parameters are known. It is envisaged that in the distant future, a casting operator should be able to establish a production route through a systematic material/process selection data base, once the casting quality and service requirements are known. This could be achieved if each of the routes in Fig. 1.1 could be replaced by quantitative models linking the various stages in the production schedule.

In addition, the present trend towards near-net-shape casting minimizes or eliminates the need for mechanical working of manufactured components and, often, the separate heat-treatment procedures. Therefore, the principal and enormous task of creating the required microstructure which determines the product quality, rests squarely on the solidification process. Thus, the reliability of the product is now solely dependent on the solidification phenomena. It is then obvious that any successful development of near-net-shape casting will depend critically on the understanding and application of fundamental knowledge of solidification carried into the rapid solidification range. It is envisaged that the usefulness of this kind of knowledge will require some definite links between the separate processes that contribute to solidification. Of particular importance in this regard is the link between the microstructure and hence product quality, and other aspects of solidification such as fluid flow, heat transfer, nucleation and growth processes, as well as defects.

This work focuses on the coupling of heat transfer phenomena and the resultant microstructure at the early stages of solidification in low melting point alloys. Dendrite arm spacing (DAS) is used as a measure of the degree of fineness of the microstructure. The evolution of the desired microstructure is ultimately linked to all the processes that contribute to solidification, and the microstructure can be predicted if the quantitative relationships between it and the other processes are known.

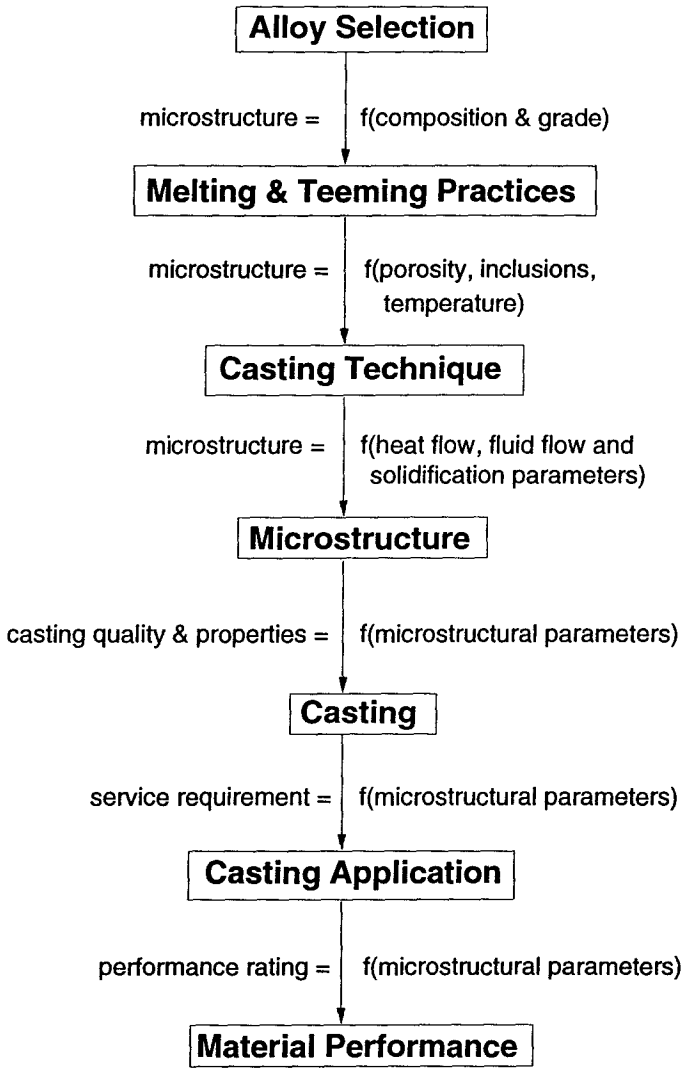

Fig. 1.1 Schematic illustration of the inter-relationship between the microstructure and other process variables.

1.2 Heat and Fluid Flow During Solidification

During solidification of metal on a substrate surface, the overall heat flow is a function of three major thermal resistances: the mold resistance, the interface resistance and the casting resistance. These resistances reduce the overall heat flow during casting. In most casting processes, it is desirable to control these resistances in order to optimize the solidification process. The casting resistance usually depends on the shell thickness which in turn depends

on the mold and interface resistances. The mold resistance can be controlled by adequate choice of mold material, mold dimensions and cooling method. The characterization of the interfacial resistance has always been a major source of uncertainty in the modeling of any solidification process. This resistance is a time-dependent variable particularly at the initial stages. The transient nature of interfacial resistance during casting is attributed to the dynamics of the metal/mold contact surface or surfaces.

In general, the metal/mold interface may exist in three major forms[4] - (a) clearance gap, (b) conforming contact or, (c) non-conforming contact as illustrated in Fig. 1.2. There could be a combination of these states at each stage of the solidification process. Each of these states affects the interface resistance by a different amount.

In the case of conforming contact, perfect contact could be assumed such that heat transfer across the interface becomes a classical heterogeneous thermal contact problem. The thermal conductance in the interface is expressed in terms of thermal conductivities of the media in contact, the real area in contact, number of contact spots per unit area, actual surface profiles, etc. For nonconforming contact, interfacial oxide films and mold coatings together with the factors mentioned above are limiting factors to interfacial heat transfer.

When the surfaces of the metal and mold are separated by a gap of finite thickness, the heat transfer across this gap most often limits the effectiveness of heat transfer between the metal and the mold. Surface interactions, geometric effects, transformations of metal and mold materials are some of the factors that contribute to gap formation. Once the gap is formed, heat transfer across the gap could occur in any of the three modes of heat transfer: conduction, convection and radiation. The extent of each mode is controlled by the gap width, the composition of the gap and the temperature of the two surfaces separated by the gap.

Fluid flow during casting results from either induced or natural forces. Within the bulk liquid region, the teeming mechanism and any form of stirring or vibration are the major sources of induced forces that affect fluid dynamics during casting. Natural forces which originate from thermal gradients, solute gradients, surface tension and transformation can also create significant fluid flow within a casting.

Convection induced by fluid flow influences solidification at both the macroscopic and microscopic levels. At the microscopic level, it can change the shape of the isotherms and reduce the thermal gradients within the liquid region. Even if this does not dramatically modify the overall solidification, the local solidification conditions, macrosegregation, and the microstructure itself can be greatly affected by convection[5]. Within the mushy zone, volume changes during solidification can drag the fluid in (or out) of the interdendritic region and ultimately lead to microporosity formation.

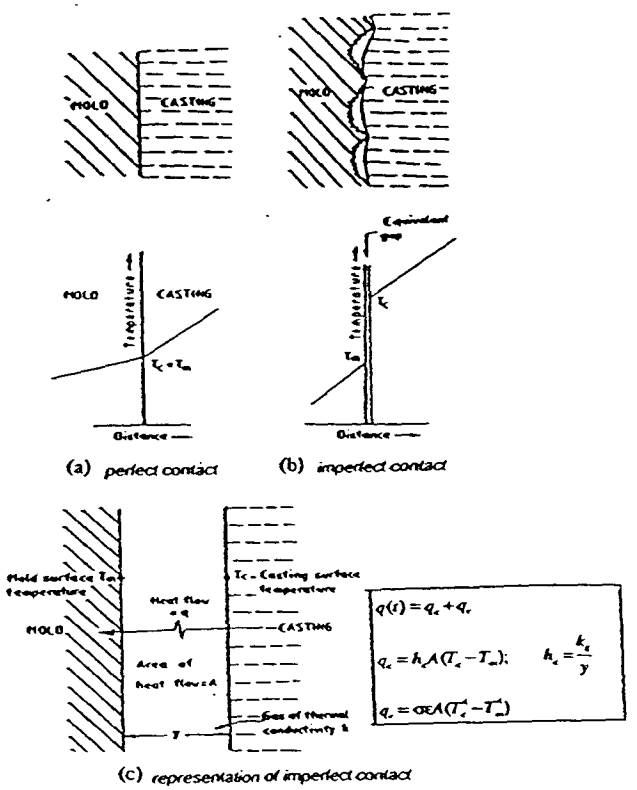

Fig. 1.2 Casting/Mold interface[6].

1.3 Microstructural Evolution during Solidification.

Microstructural evolution during casting has been a subject of great interest to researchers for some time. The degree of fineness of the microstructure determines the quality and properties of the cast component. The goal of most practical casting processes is to obtain fine isotropic crystals such that segregation, porosity, and other defects are substantially reduced. Microstructural evolution is dependent on the dual process of nucleation and growth.

1.3.1 Nucleation

Nucleation may be defined as the formation of new phase (solid in the case of solidification) in a distinct region separated by a discrete boundary or boundaries. With respect to kinetics, nucleation can be classified either as continuous or instantaneous. Continuous nucleation assumes that nucleation occurs continuously once the nucleation temperature is reached while instantaneous nucleation assumes that all nuclei are generated at the same time at a given nucleation temperature. Based on the nucleation sites, two distinct types of nucleation are known: homogeneous and heterogeneous nucleation. Homogeneous nucleation occurs when all locations have an equal chance of being nucleation sites. On the other hand, heterogeneous nucleation occurs when certain locations are preferred sites. In most practical castings, the nucleation process is invariably heterogeneous; points on the substrate surface and any inhomogeneities in the bulk liquid being preferred sites.

Not all the physical features which determine the properties of a surface for heterogeneous nucleation of a phase are understood. In terms of surface matching, the concept of coherency is important[7]. A coherent interface is one in which matching occurs between atoms on either side of the interface. If there is only partial matching, the interface is considered to be semi-coherent. The ratio of the lattice parameter of the crystal being nucleated to that of the substrate is used as a measure of surface matching. Coherent surfaces are characterized by a single source of strain energy at the interface (strain due to misfit) and allow for good wettability.

On the other hand, semi-coherent interfaces are characterized by both misfit and dislocation strains, and therefore reduce the wettability of the surface by molten metal. Furthermore, charge distribution which leads to some electrostatic effects can influence the choice of nucleation sites[7].

1.3.2 Dendritic Growth

Once solid nuclei have been formed, they will grow provided the thermodynamic conditions (mainly energy reduction) are fulfilled. In terms of the nature of transformation, two main types of growth morphology have been identified[8] - eutectic and dendritic. Eutectic growth involves the transformation of liquid simultaneously into two solids while dendritic growth involves transformation into a single solid phase.

With respect to the solid/liquid interface geometry, growth can be dendritic, planar, cellular, lamellar or even armophous. Dendritic growth is by far the most common growth morphology in alloys[9] except for the case of eutectics where cellular growth predominates.

A dendrite element is defined as that portion of a grain at the completion of solidification which is surrounded largely by an isoconcentration surface. Depending on the nucleation and heat flow conditions, dendritic growth could be equiaxed or columnar. Columnar dendritic growth is mainly solute diffusion controlled while equiaxed dendritic growth is heat and/or solute diffusion controlled. Therefore, dendritic growth can be heat flux, solute flux, or heat and solute flux controlled. The shape of the dendrites has been found to depend on the heat flow conditions, small undercooling resulting in cylindrical dendrites while large undercooling produces spherical dendrites[10].

The first set of dendrites grows parallel to the direction of heat flow (more pronounced in the case of columnar growth) and are termed 'primary dendrites'. These dendrites subsequently become preferred sites for further nucleation and growth, leading to branching.

Growth stops when the dendrite tip encounters a barrier in its path, usually other dendrites. The idealized final form of the dendrite elements consists of primary, secondary, tertiary, quaternary and more arms as illustrated in Fig. 1.3. It is to be noted that there is a strong competition among the different arms and only the relatively larger ones survive at the end of solidification; the others shrink and eventually disappear as a result of coarsening.

The driving force for arm coarsening is the reduction in total surface energy in the system which acts through the Gibbs-Thomson effect at curved surfaces. Thus, solid surfaces of different curvatures, both positive and negative, establish different liquid concentrations at their interfaces and diffusion in the liquid from high to low solute regions results in morphological changes. The coarsening effect is more pronounced in secondary and higher order arms, than in the primary arms. This is because the primary dendrites are more geometrically constrained, thereby reducing the effectiveness of coarsening phenomena. It has been established that for most solidification processes, the coarsening phenomenon rather than the initial dendrite arm, is the overiding factor that controls the final dendrite arm spacing[11]. Hence, the secondary dendrite arm spacing is a better indication of local heat flux and solute flux conditions during solidification.

The dendrite arm spacing (DAS) is a fundamental characteristics of microstructure and has been used over the years as a measure of fineness and, hence, quality of cast products. Both primary and secondary dendrite arm spacings have been employed to quantify the degree of fineness of microstructure. Dendrite arm spacing has been linked empirically to other solidification parameters such as dendrite tip velocity, cooling rate, temperature gradient in solidifying material, local solidification time and distance from the chill surface.

The importance of DAS and its suitability as an efficient structural parameter for process-structure and structure-property relations in cast products have been illustrated by various researchers[12-19]. It has been shown that the dendrite arm spacing can be related to the following:

(i) tensile properties of a casting[12,13] (ultimate tensile strength, yield strength, percent elongation, etc)

(ii) fractography of unidirectionally solidified alloys[11,14] (crack length, percentage elongation to failure, micro-hardness and impact energy)

(iii) defects[15-17] (segregation, porosity, inclusion)

(iv) heat treatment characteristics of casting[11] (homogenization)

(v) subsequent mechanical working of casting[11] (extrusion)

(vi) corrosion behavior of casting[18,19]

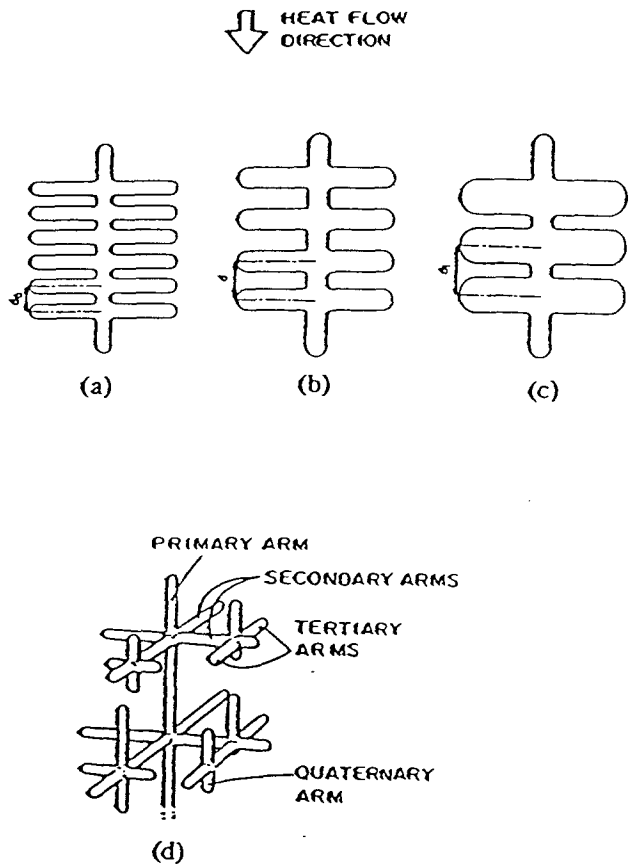

Fig. 1.3 Schematic illustration of dendritic growth[11]. An initial dendrite arm spacing, d_o, is formed early during solidification (a). Subsequently, some of the arms disappear (b & c), so that the dendrite arm spacing increases to the final size, d_f (c). The possible dendritic structure at the end of solidification is represented in (d).

Chapter 2

LITERATURE SURVEY

2.1 Solidification Modeling

The understanding and control of complex processes such as solidification are often achieved through a rigorous application of analysis and synthesis, a procedure known as process modeling[20]. Process modeling could be defined as a comprehensive elucidation of a process or its component part in both qualitative and quantitative terms such that the process or its part could be better understood, controlled or improved. The basic steps in process modeling are illustrated in Fig. 2.1. It is a dual process of analysis and synthesis that involves a combination of two main tools[21]:

(i) experimental procedures (observations and measurements in one or more of the following: laboratory, existing process, pilot plant and physical model)

(ii) mathematical modeling

The first step is to break down the problem into its component parts that are sufficiently detailed to allow a comprehensive study of the fine details using the above modeling tools. Following this step of analysis of individual building blocks of the process, the process is then synthesized by incorporating these blocks into a model of the entire process. Now, the process is better understood and its behavior in practice can be predicted. It is then possible to control, modify and improve the process. The process can equally be scaled to other sizes or the improved understanding of the process can be applied to develop a wholly new one.

Solidification phenomenon has benefitted from all the basic tools of process modeling[20]. Observations and measurements yield the fundamental understanding and knowledge, but

mathematical models provide the framework to assemble and apply this knowledge quantitatively, for a deeper understanding, control and improvement of the process. Hence, mathematical modeling is a very powerful tool in quantitative process analysis and synthesis[21].

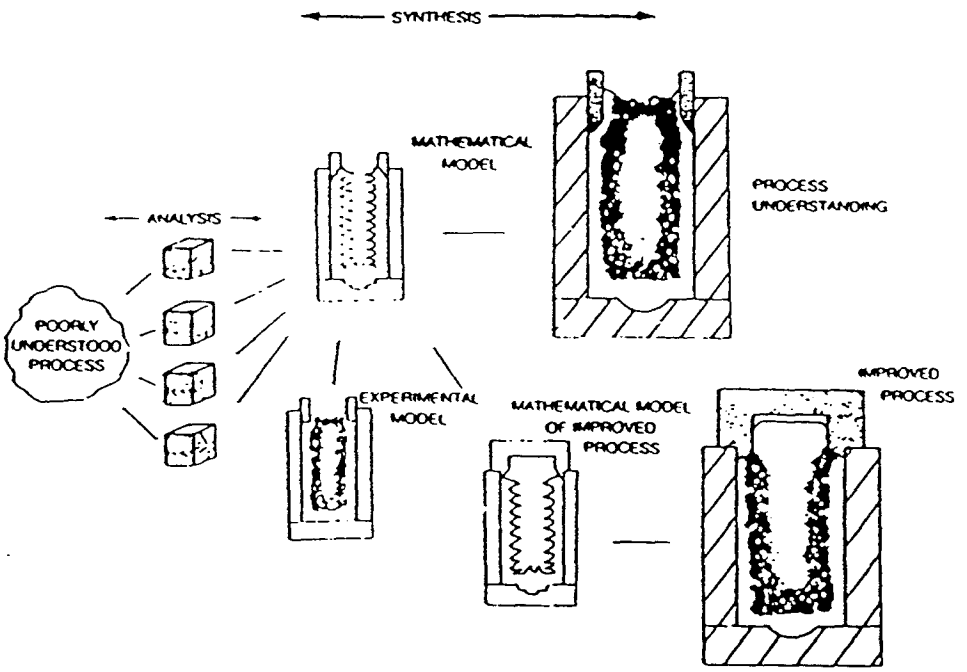

Fig. 2.1 Schematic illustration of process understanding and improvement with the aid of modeling[20].

Based on the above, it is now widely accepted that a complete model for the simulation of solidification[22] should include both the macroscopic modeling (heat transfer, fluid flow, stress distribution, macrostructure and macro-defects) and microscopic modeling (microstructure, microsegregation, microporosity and other micro-defects).

From a mathematical viewpoint, solidification modeling has been directed towards a search for analytical and numerical solutions to the continuity equations in the presence of a phase change[5]. Analytical solutions have been applied to a limited number of simplified cases[7] (mainly lumped capacity approximation, semi-infinite and finite slab analyses). The numerical

solution techniques include the finite difference methods[23,24] (FDM), the finite element methods[25] (FEM), the boundary element method[26] (BEM), the control volume method[27] (CVM) and the direct finite difference method[28] (DFDM)

Whatever numerical technique is chosen for any particular problem, the efficiency of the solution is limited by three main factors[4,5]:

(1) the characterization of the interfacial resistance between the casting and the mold or other external cooling device.

(2) the treatment of the latent heat release and the subsequent evolution of the microstructure.

(3) the treatment of accompanying fluid flow during solidification.

2.2 Heat Flow - Interface Resistance

As mentioned in Chapter 1, the characterization of interfacial heat transfer resistance during solidification has always been a major source of uncertainty in modeling of any solidification process. The study of metal/mold interfacial heat transfer is very important in two respects[29]:

(i) for promoting the accuracy of numerical heat transfer simulation

(ii) for improving casting quality through better control of metal/mold thermal resistance.

The problem here is to obtain a solution to Newton's law of cooling;

$$q = h(T_c - T_m) \tag{2.1}$$

For most casting processes, the variables in Equation (2.1) - the heat transfer coefficient (h), the temperature of casting (T_c) and the mold temperature (T_m) must be determined at the interface. However, surface measurements have serious experimental impediments. Firstly,

the physical situation at the interface may be unsuitable for attaching a sensor. Secondly, the accuracy of the measurement may be seriously impaired by the presence of a sensor. Therefore, it is preferable to measure accurately the temperature history at an interior location and to estimate the surface condition from this measurement. This technique has become known as the *inverse heat conduction problem (IHCP).*

IHCP techniques have been applied extensively in characterizing the interface resistance in solidification modeling[30]. The numerical techniques involve the use of either the heat flux (discrete values or specified functions) boundary condition or the heat transfer coefficient (discrete values or specified functions) boundary condition. The basic assumption in either case is that heat transfer conditions on both sides of the interface are exactly the same. In other words a quasi-steady state exists at the interface, there is no heat source, heat sink or accumulation across the interface. Pehlke et al.[4] suggested a criterion to estimate the degree to which a quasi-steady state assumption is valid across an interface of finite thickness y_i. This criterion is the square root of the dimensionless Fourier number;

$$\sqrt{Fo} = (\alpha t)^{1/2}/y_i \qquad > \quad 1.0 \tag{2.2}$$

where α is the average thermal diffusivity across the interface and y_i is the interface thickness.

In many heat transfer problems that attain steady state equilibrium, it has become customary simply to assign a constant heat transfer coefficient. However, it has since been realized that the interfacial heat transfer is a time-dependent variable. The transient nature of interfacial heat transfer is attributed to the dynamics of the casting/mold contact. As stated earlier, the casting/mold interface often assumes a complex combination of finite gap, conforming and non-conforming contacts during solidification. Although the flow of heat near the interface is microscopically 3-dimensional, the overall heat transfer coefficient across such an interface from a macroscopic standpoint may be written as the sum of three components[4]:

$$h = h_s + h_g + h_r \tag{2.3}$$

where h_s is the part due to solid conduction through the points in contact, while h_g and h_r denote the contributions of gas conduction and radiation across the void spacing surrounding the contact points.

Using measured temperatures in both casting and mold together with analytical and/or numerical solutions, several researchers have attempted to quantify the transient interfacial heat transfer coefficient[6,29,31-47]. Earlier, several workers have proposed the use of a constant time-averaged h to account for the transient nature of the interfacial heat flow[31-33]. Others[34-38] derived more specific expressions for h as summarized in Table 2.1.

A review of the early studies on the interfacial resistance[6,29,31-47] shows that such factors as casting and mold geometry, mold surface roughness, contact pressure, time after teeming, thermal characteristics of casting and mold, mold coatings and nature of contact between casting and mold are known to affect the interfacial resistance. Tiller[34] observed that h decreases with time from a peak value attained at contact.

Using a chill immersion technique, Sun[35] observed that h increases linearly with time which is exactly opposite to Tiller's result. The immersion technique used by Sun enabled a continuous rise in h with time due to increased contact pressure as the casting contracts towards the chill and the chill expands towards the casting. Levy et al.[38] used a similar geometry to show that improved thermal contact could be achieved between casting and mold by utilizing a forced fit technique where the contraction and expansion of the mold are used to prevent gap formation.

Sully[39] found that the heat transfer coefficient during solidification of metals can exhibit features of the Sun model[35] and the model due to Tiller[34]. He found that in most cases, h rises rapidly to a peak value and then declines to a low steady value under conditions where the casting contracts away from the mold.

Table 2.1 The various expressions for evaluation of heat transfer coefficient.

Reference	Expression for h	Remark
34	$h = \frac{h'}{2\sqrt{t}}$	receding interface
35	$h = a + bt$	increasing contact pressure
36	$h = A\frac{k_m}{x_r}\sqrt{(P/H_v)}$	only h_s was considered
37	$h = C\sqrt{Ra^{-b}}$	h increases with increasing surface smoothness of the mold
6	$h = \frac{k}{a}\left(\frac{r\sin\theta}{\bar{y}} + \frac{a - \sin\theta}{y_f}\right) = \frac{k}{y_{eq}}$	h_r neglected
-	$h = \frac{k_g}{(x_g + s_1 + s_2)}$	only h_g is considered
-	$h = \frac{\sigma(T_c + T_m)(T_c^2 + T_m^2)}{\left(\frac{1}{\varepsilon_c} + \frac{1}{\varepsilon_m} - 1\right)}$	only h_r is considered

Studies on the effect of contact pressure on the heat transfer coefficient have been conducted by several investigators[36,40,41]. It has been found that interfacial heat transfer coefficient is proportional to the square root of contact pressure[36].

Studies have also been undertaken on the effect of surface microprofile mainly in terms of roughness and surface coatings[33,35,39,42-44]. It was found that the heat transfer coefficient increases with increasing surface smoothness. In the case of surface coating, the heat transfer

coefficient depends on the thermal conductivity, thickness and surface smoothness of the coating material[39,42-44]. It increases with increasing conductivity of coating, decreasing thickness of coating and increasing surface smoothness of coating.

Suzuki et al.[45] measured the heat transfer coefficient between melt and chill by dropping liquid tin on a cylindrical chill made of different materials (brass, stainless steel, chromium-plated brass and nickel-plated brass). They claimed that the heat transfer coefficient does not depend on the thermal properties of the chill materials but presumably on the wettability between melt and chill.

In a recent work, Sharma et al.[6] proposed that an actual mold could be conceived to be a combination of v-grooves having different groove parameters such that the overall heat transfer coefficient of the surface can be calculated as series/parallel combinations of the constituent v-grooves. They proposed that the variation of h with time generally exhibits three distinct regions as illustrated in Fig. 2.2. From the time of initial contact (stage I), h rises rapidly to a peak value and decreases rapidly in a fluctuating manner. In stage II, h is constant or fluctuates around a mean value. Stage III depends on the extent of contact pressure; h remains fairly constant if the contact pressure is constant but increases if the contact pressure is increased and decreases if the interface recedes.

Most of the recent IHCP techniques utilize the heat flux boundary condition. Earlier, Jacobi[46] has used a time dependent interfacial heat flux such that when this transient heat flux is divided by the estimated temperature drop across the interface, the transient interfacial heat transfer coefficient is obtained.

Pehlke et al.[4,29,47] did a comprehensive study of the heat transfer and solidification of aluminum and copper bronze using a water cooled copper chill. They successfully characterized the metal/chill contact phenomena and gap formation by using transducers. They also simulated

the effect of chill location on melt/chill contact and found that a sizeable gap forms when the chill is on top of the melt while the melt and chill exhibit some form of non-conforming contact in the case when the chill is located below the melt. Their numerical analysis involves an extensive use of the 1-D inverse heat conduction technique based on the nonlinear estimation method of Beck[48].

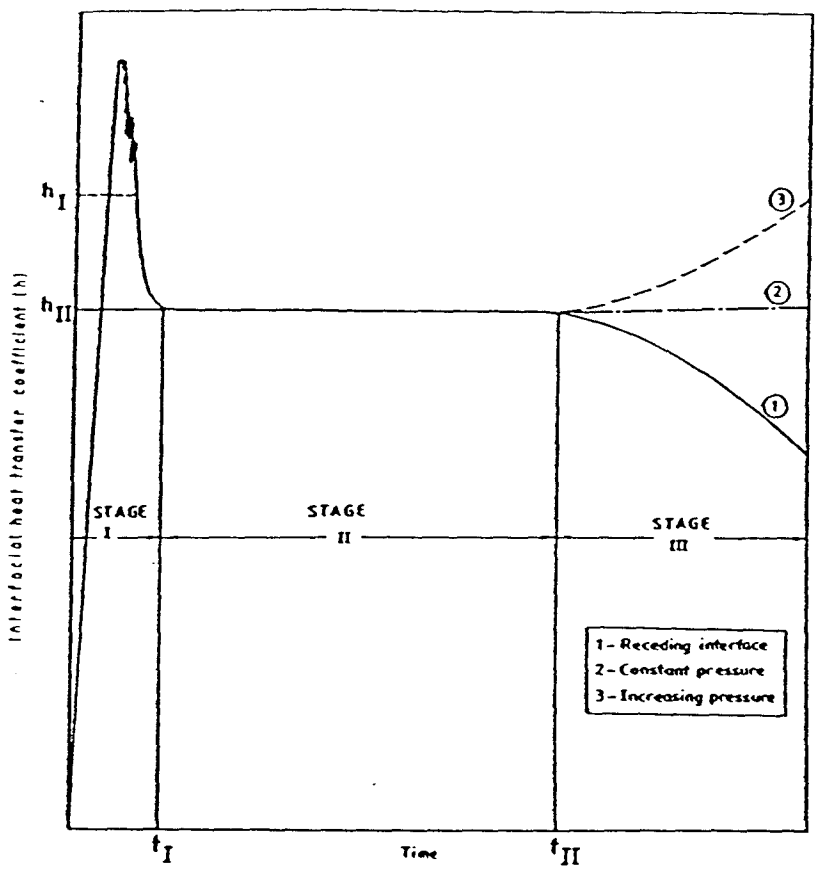

Fig. 2.2 Schematic illustration of the typical variation of heat transfer coefficient (h) with time during solidification[6].

In a recent study by Kumar and Prabhu[49] using the same technique as Pehlke and co-workers, it was shown that the maximum interfacial heat flux between a chill and solidifying metal could be represented as a power function of the chill thickness and chill thermal diffusivity:

$$q_{max} = C_1(X/\alpha)^{n_1} \tag{2.4}$$

Furthermore, they found that the heat flux after the maximum value could also be expressed as a power function of the thermal diffusivity and time in the form:

$$(q/q_{max})\alpha^{0.05} = C_2 t^{n_2} \tag{2.5}$$

The constants, C_1 and C_2 were found to be dependent on the casting composition for the aluminum and copper alloys studied[49]. Therefore, the interfacial heat flux should depend not only on the thermophysical properties of the mold material but also on the properties of the casting alloy. Bamberger et al.[50] found that for the same mold and casting conditions, the interfacial heat flux depends on the alloy composition for Al-Si alloys. A typical heat flux profile is shown in Fig. 2.3. It is observed that the heat flux profile follows the same trend as the heat transfer coefficient (See Fig. 2.2).

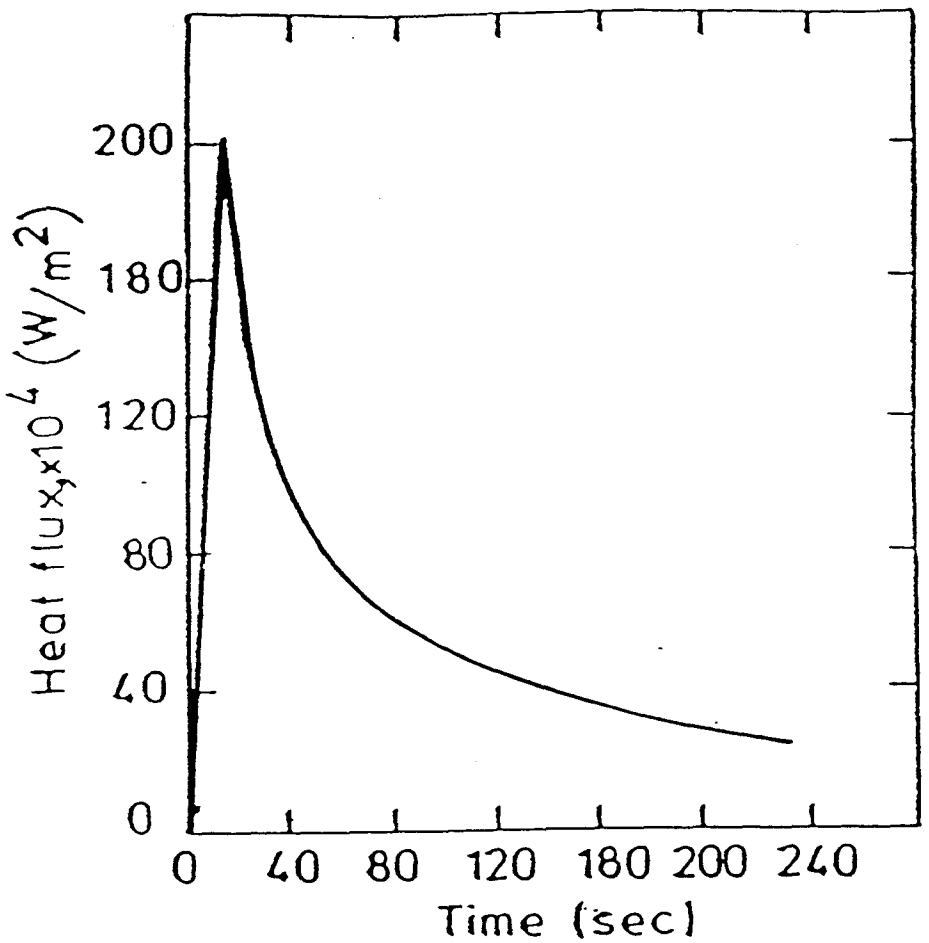

Fig. 2.3 Estimated heat flux profile for 50 x 50 x 50 mm copper chill without coating and Al-13.2% Si alloy[42].

2.3 Heat Flow - Latent Heat Evolution

The energy conservation equation for a solidifying material is given by:

$$\frac{\partial}{\partial x}\left(k\frac{\partial T}{\partial x}\right)+\frac{\partial}{\partial y}\left(k\frac{\partial T}{\partial y}\right)+\frac{\partial}{\partial z}\left(k\frac{\partial T}{\partial z}\right)+Q' = \rho C_p\frac{\partial T}{\partial t} \qquad (2.6)$$

where, ρ, C_p and k assume the values of the particular phase or phases prevailing at a given temperature and location in the casting. The source term, Q', describes the rate of latent heat evolution during any liquid-solid transformation and may be written as

$$Q' = \rho L \frac{\partial f_s}{\partial t} \tag{2.7}$$

The solution to Eq. (2.7) has been of great interest to researchers of solidification and other fields where phase change occurs. The problem is two fold; (a) how is the latent heat actually released in practice, and (b) how should the latent heat phenomena be accounted for in a mathematical model?

In terms of continuity at the interface, two major techniques can be identified from the literature[5] - (i) the 1-domain and (ii) 2-domain or front tracking technique. These are illustrated in Fig. 2.4. The 1-domain techniques assume that the solid and liquid phases constitute the same medium, with average thermal properties defined at each node as a function of temperature. This method is computational simpler since the phase boundary is not explicitly defined. This is advantageous in handling problems where the phase change region is a volume (such as the mushy zone) rather than a surface (such as isothermal transformation front). The most common 1-domain methods include the temperature recovery methods, the specific heat methods, the enthalpy methods, the latent heat methods, and other hybrids of the three.

The 2-domain or front tracking techniques assume that the solid and liquid phases are two separate media. Accordingly, continuity equations are applied separately to each medium together with a specified set of equations for the interface between them. These techniques are more complicated with respect to computing and are best suited for isothermal transformation or transformations involving isolated cells or dendrites. The common 2-domain methods include the line tracking methods[51,52], spatial transformation method[53] and spatial grid deformation

methods[54,55].

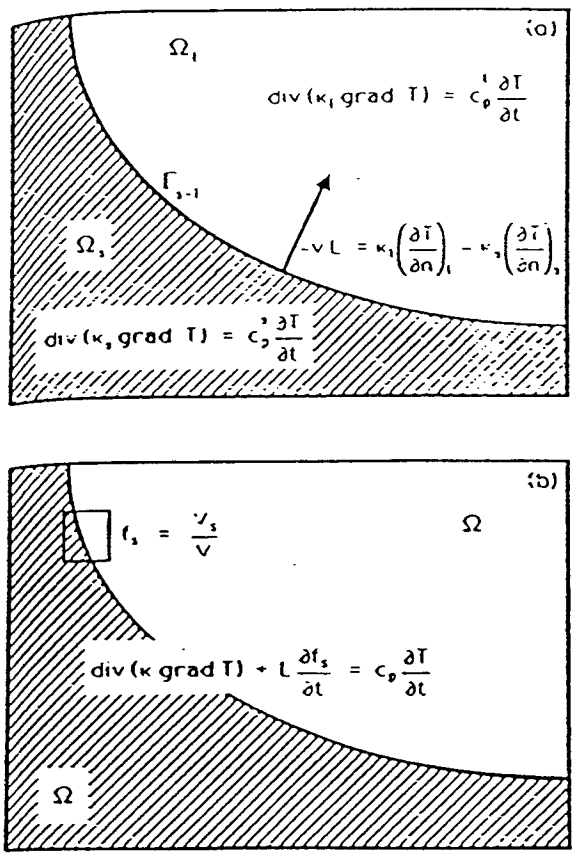

Fig. 2.4 Schematic representation of phase change handling in heat flow modeling of solidification[5]; (a) front tracking or 2-domain method, (b) 1-domain method.

Poirier and Salcudean[56] reviewed the various numerical methods used in mathematical modeling of phase change in liquid metals based on :

(a) the ability to solve multidimensional problems

(b) ease of implementation

(c) ability to account adequately for the mushy region

They concluded that the 1-domain techniques are simpler, easier to use and are better suited for handling transformations with an appreciably mushy region commonly encountered in solidifying metal alloys. This conclusion agrees with that of other researchers in the field of solidification[5]. Hence, emphasis here is on the 1-domain techniques.

2.3.1 Temperature Recovery Method

Sometimes referred to as a postiterative method, the temperature recovery technique was first reported by Dusinbere[57] and later by Doherty[58] who used it in a FDM solution of isothermal transformation. It has since be applied to non-isothermal cases[59] and also incorporated into FEM solutions[60]. In this method, the temperature of the node at which phase change is occurring, is set back to the phase change temperature and the equivalent amount of heat is added to the enthalpy budget for that node. Once the enthalpy budget equals the latent heat for the volume associated with that node, the temperature is allowed to fall according to the heat diffusion. This could be represented mathematically by

$$T_{node} = T \qquad T > T_L \tag{2.8a}$$

$$T_{node} = T_L - (\Delta H/L)\Delta T \qquad T_S \leq T \leq T_L \tag{2.8b}$$

$$T_{node} = T \qquad T < T_S \tag{2.8c}$$

The main advantage of this method is that conservation of energy is always ensured. However, the technique is known to produce undesired 'wiggles' or 'false eutectic plateaus' that result from energy conservation since any finite volume has a constant temperature during

isothermal solidification[5]. The method has also been shown to be very sensitive to the size of the time step[56]. Furthermore, the errors in the approximation are more magnified in the vicinity of the mushy zone than in the single phase regions[56].

2.3.2 Specific Heat Method

Probably the most commonly used method in solidification modeling, the specific heat technique is attributed to Hashemi and Sliepcevich[61], who introduced it in an implicit FDM code. It was later adopted to FEM formulation[62]. The procedure is to assign a pseudo specific heat to the region where the phase change is occurring.

Substituting Eq. (2.7) into Eq. (2.6) above and re-arranging, the following is obtained:

$$\begin{aligned} \frac{\partial}{\partial x}\left(k\frac{\partial T}{\partial x}\right)+\frac{\partial}{\partial y}\left(k\frac{\partial T}{\partial y}\right)+\frac{\partial}{\partial z}\left(k\frac{\partial T}{\partial z}\right) &= \rho C_p\frac{\partial T}{\partial t}-\rho L\frac{\partial f_s}{\partial t} \\ &= \rho\frac{\partial T}{\partial t}\left(C_p-L\frac{\partial f_s}{\partial T}\right) \end{aligned} \tag{2.9}$$

If a pseudo specific heat is defined as

$$C_{pseudo} = C_p - L\frac{\partial f_s}{\partial T} \tag{2.10}$$

then Eq. (2.9) becomes

$$\frac{\partial}{\partial x}\left(k\frac{\partial T}{\partial x}\right)+\frac{\partial}{\partial y}\left(k\frac{\partial T}{\partial y}\right)+\frac{\partial}{\partial z}\left(k\frac{\partial T}{\partial z}\right) = \rho C_{pseudo}\frac{\partial T}{\partial t} \tag{2.11}$$

Eq. (2.11) is the mathematical expression of the specific heat method.

The accuracy of the method depends on the technique of solving Eq. (2.7), that is, the evolution of the solid fraction. Furthermore, it is difficult to ensure energy conservation[5] using

the specific heat method since no condition is generally imposed on Eq.(2.11). The simplest procedure is to assume a linear release of the latent heat which results in the following expressions:

$$C_{node} = C_p \qquad T > T_L \tag{2.12a}$$

$$C_{node} = C_p + L/\Delta T \qquad T_S \le T \le T_L \tag{2.12b}$$

$$C_{node} = C_p \qquad T < T_S \tag{2.12c}$$

This is the well known "*apparent specific heat method*". The main disadvantage of this technique lies in the discontinuity in specific heat at both the liquidus and solidus temperatures. A different method referred to as the "*effective specific heat method*" was proposed by Poirer and Salcudean[56]. In the effective method, a temperature profile is assumed between nodes and instead of calculating an apparent capacity based on the nodal temperature, an effective capacity is calculated based on an integration through the nodal volume. For a linear temperature distribution, the effective capacity method can be represented by

$$C_{node} = C_p \qquad T >> T_L \tag{2.13a}$$

$$C_{node} = C_{eff} = \left\{ \int C_p dV \right\} / V \qquad T_S + \zeta \le T \le T_L + \zeta \tag{2.13b}$$

$$C_{node} = C_p \qquad T << T_S \tag{2.13c}$$

where ζ is a number that accounts for the effect of the surrounding nodes on the nodal volume of interest and is dependent on the node size. This method allows a node with a volume covering two regions (liquid and mushy, or mushy and solid) to balance the effect of each region. It has been shown that this particular ability reduces the possibility of either over estimating or under estimating the effect of latent heat. It also eliminates the discontinuity at the liquidus and solidus temperatures associated with the apparent heat method[56]. A typical variation of specific heat with temperature utilizing the apparent and effective methods is shown in Fig.2.5.

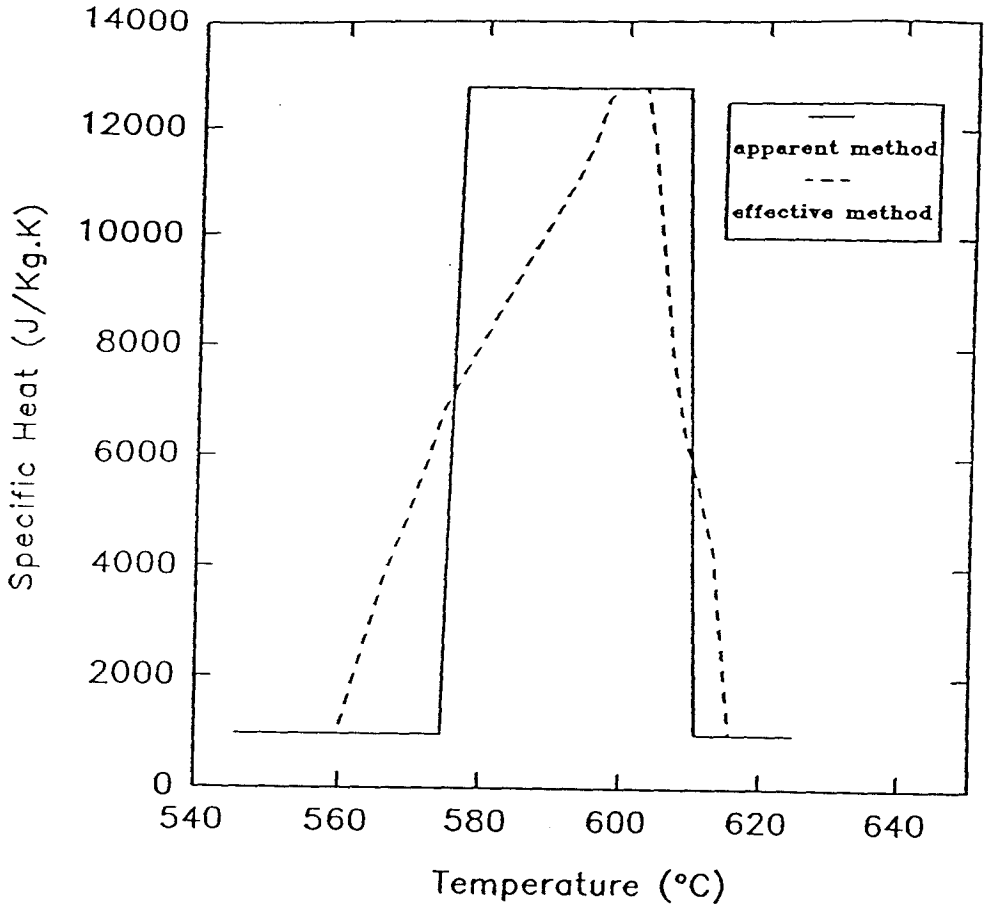

Fig. 2.5 Calculated variation of specific heat with temperature for apparent and effective specific heat methods for a Al-7%Si alloy.

2.3.3 Enthalpy Methods

Most of the pioneering work on this method were based on finding solutions to nonlinear equations using the implicit FDM scheme[63-65]. To date, both explicit and implicit FDM and FEM solutions based on the enthalpy method have been obtained[66-68]. A hybrid of the enthalpy and apparent heat capacity methods has also been proposed with a novel three-time level FDM scheme[69].

The method is based on the formulation of the right hand side of Eq.(2.9) in terms of enthalpy instead of specific heat and temperature. Recalling Eq.(2.9) and rearranging, the following is obtained

$$\frac{\partial}{\partial x}\left(k\frac{\partial T}{\partial x}\right)+\frac{\partial}{\partial y}\left(k\frac{\partial T}{\partial y}\right)+\frac{\partial}{\partial z}\left(k\frac{\partial T}{\partial z}\right) = \rho C_p\frac{\partial T}{\partial t}-\rho L\frac{\partial f_s}{\partial t}$$

$$= \rho\frac{\partial}{\partial t}(C_pT-Lf_s) = \rho\frac{\partial H}{\partial t} \qquad (2.14)$$

where $H = C_pT-Lf_s$ (2.15a)

or $\int_0^T dH = \int_0^T C_p dT - L\int_{f_s(T=0)}^{f_a(T=T)} df_s$ (2.15b)

Thus $H(T) = \int_0^T C_p dT + L(1-fs) \qquad (f_s=1.0 \quad \text{at} \quad T=0)$ (2.15c)

The enthalpy method has some obvious advantages over the specific heat method. First, it ensures energy conservation at all times since the enthalpy is a direct dependent variable in the energy equation. Secondly, there is no discontinuity at either the liquidus or solidus temperatures since any solidification path is characterized strictly by a decreasing enthalpy even with recalescence. However, the enthalpy method is more difficult to implement with existing standard codes and in most cases has been known to produce 'wiggles' or 'false eutectic plateaus in the cooling curves just like the temperature recovery method[5]. The typical enthalpy profile using this method is shown in Fig.2.6

2.3.4 Latent Heat Method

This method involves the solution of Eq.(2.6) without any transformation; the latent heat is neither incorporated into the specific heat nor the enthalpy budget. Eq.(2.7) is solved directly at each time step and substituted into Eq.(2.6). The method ensures energy conservation and is sometimes referred to as the solidification kinetics method[22]. A typical enthalpy profile

using this method is also depicted in Fig.2.6.

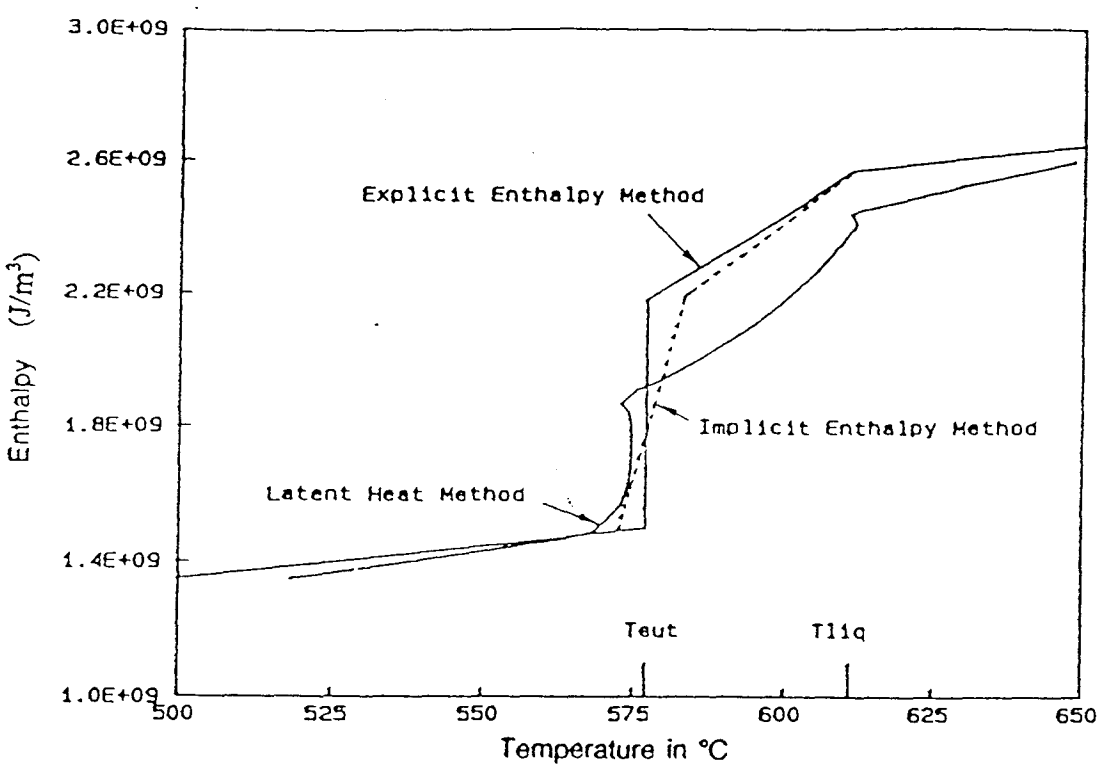

Fig. 2.6 Calculated variation of enthalpy with temperature for enthalpy and latent heat methods for a Al-7%Si alloy[22].

2.3.5 The Nature of Latent Heat Evolution

The four methods discussed above are merely the techniques of handling latent heat release during mathematical modeling of solidification. The larger question now is how this latent heat is actually released during solidifcation.

Two major procedures have been adopted in determining the actual nature of latent heat release:

(1) cooling curve analysis

(2) nucleation and growth laws.

Only the cooling curve analysis technique will be discussed while the nucleation and growth laws will be taken up under microstructural evolution.

2.3.5.1 Cooling Curve Analysis

Experimental cooling curves can be used to obtain pertinent information on the actual nature of latent heat release during solidification. This has been done by performing experiments on lumped parameter systems[22,70] with minimal temperature gradients since they allow for simplified analysis. A solidifying metal can be treated in this way if its Biot number is less than 0.1

$$Bi = \frac{hL_c}{k} < 0.1 \tag{2.16}$$

For any casting that satisfies the above criterion, the basic energy conservation can be written as

$$\frac{hA}{V}(T_\infty - T) + Q' = \rho C_p \frac{dT}{dt} \tag{2.17}$$

In the single phase region (either liquid or solid), there is no heat source term such that the above equation becomes

$$\frac{dT}{dt} = \frac{hA}{\rho V C_p}(T_\infty - T) = \Theta(T_\infty - T) \tag{2.18}$$

where Θ is the inverse of the time constant. It is noted that dT/dt is simply the cooling rate which can be obtained by immersing a thermocouple into the liquid or solid phase.

In one of the cooling curve analysis techniques sometimes referred to as the zero curve method[22], the latent heat released up to a time, t, is approximated by

$$L(t) = \int_o^t \left[\left(\frac{dT}{dt} \right)_{cc} - \left(\frac{dT}{dt} \right)_{zc} \right] \tag{2.19}$$

where $(dT/dt)_{zc}$ is known as the zero curve and is obtained by simply joining the dT/dt obtained for the liquid phase to that obtained for the solid phase. Once the L(t) is known, the determination of the cooling rate as a function of time becomes trivial. However, the above equation is unique to the particular cooling rate obtained in a given experiment. For a more general application, the rate of evolution of the solid fraction for a particluar alloy system should be known. The solid fraction up to time, t, can be obtained as follows

$$f_s(t) = \frac{L(t)}{L} \tag{2.20}$$

By interpolation of experimental data at various cooling rates, it was found that df_s/dt varies not only with time but also with the cooling rate[22] such that

$$\frac{df_s}{dt} = \left(a_o \frac{dT}{dt} + b_o \right) t + c_o \left(\frac{dT}{dt} \right)^2 + d_o \left(\frac{dT}{dt} \right) + e_o \tag{2.21}$$

By performing a series of experiments in a lumped system with a given alloy, the constants a_0 to e_0, can be evaluated. The expression for df_s/dt given by Eq.(2.21) is valid for a given alloy under all conditions including the practical non-lumped systems.

A similar technique recently published[70], utilizes an artificial variation of Θ across the solidification regions (liquid, mushy and solid) to estimate the amount of latent heat released up to a given time. For a linear variation of Θ

$$\Theta_L = \left(\frac{dT}{dt}\right) / (T_\infty - T) \qquad T > T_L \tag{2.22a}$$

$$\Theta = \Theta_L + \frac{T_L - T}{T_L - T_S}(\Theta_S - \Theta_L) \qquad T_S \le T \le T_L \tag{2.22b}$$

$$\Theta_S = \left(\frac{dT}{dt}\right) / (T_\infty - T) \qquad T < T_S \tag{2.22c}$$

Once Θ is known, the variation of latent heat with temperature can be evaluated from

$$\frac{L df_s}{dT} = C_p\left(1 + \Theta\left(\frac{T - T_\infty}{dT/dt}\right)\right) \tag{2.23}$$

By solving Eq.(2.23) for various measured temperatures, an empirical relationship between latent heat release and casting temperature can be established. This relationship could be of the form:

$$\frac{L df_s}{dT} = a + bT + cT^2 + dT^3 + \ldots. \tag{2.24}$$

Equation (2.24) is valid for a given alloy under all conditions including the practical non-lumped systems since the latent heat release is expressed only as a function of casting temperature. Once Eq.(2.24) is evaluated, the heat source term can be calculated easily from

$$Q' = \rho L \frac{df_s}{dT}\frac{dT}{dt} \tag{2.25}$$

The evolution of the solid fraction given by either method can then be handled in a mathematical model via the specific heat, enthalpy or latent heat methods.

2.4 Fluid Flow During Solidification

The handling of fluid flow in modeling non-stationary problems such as solidification is rather difficult because the regions (liquid and mushy) within which fluid flow have to be considered, changes continuously with time. As discussed in section 1.2, fluid flow in casting can originate from two main sources - induced and natural forces.

Three major approaches have been adopted in modeling the effect of fluid flow in solidification simulation:

(a) the effect of fluid flow is incorporated into the heat flow model by simply increasing the thermal conductivity by an artificial amount.

$$k_{eff} = ak \tag{2.26}$$

(b) the fluid flow pattern is replaced by a liquid region where complete mixing is assumed, plus a boundary layer whose thickness is estimated by a dimensional analysis. For instance, the Nusselt number is often expressed in terms of flow parameters and is used to determine the heat transfer coefficient between a fluid and a solid surface. Such an expression can be in the form:

$$\mathrm{Nu} = \frac{hL_c}{k_f} = a(\rho u D/\mu)^x (\alpha/\mu)^y = aRe^x Pr^y \tag{2.27}$$

(c) the fluid flow is more precisely calculated from the Navier Stokes equations

$$\rho\frac{Du}{Dt} = \rho g_x - \frac{\partial P}{\partial x} + \mu\left(\frac{\partial^2 u}{\partial x^2} + \frac{\partial^2 u}{\partial y^2} + \frac{\partial^2 u}{\partial z^2}\right) \tag{2.28a}$$

$$\rho\frac{Dv}{Dt} = \rho g_y - \frac{\partial P}{\partial y} + \mu\left(\frac{\partial^2 v}{\partial x^2} + \frac{\partial^2 v}{\partial y^2} + \frac{\partial^2 v}{\partial z^2}\right) \tag{2.28b}$$

$$\rho\frac{Dw}{Dt} = \rho g_z - \frac{\partial P}{\partial z} + \mu\left(\frac{\partial^2 w}{\partial x^2} + \frac{\partial^2 w}{\partial y^2} + \frac{\partial^2 w}{\partial z^2}\right) \tag{2.28c}$$

and the energy conservation equation for incompressible flow given by

$$\rho C_p\left(u\frac{\partial T}{\partial x}+v\frac{\partial T}{\partial y}+w\frac{\partial T}{\partial z}\right)=k\left(\frac{\partial^2 T}{\partial x^2}+\frac{\partial^2 T}{\partial y^2}+\frac{\partial^2 T}{\partial z^2}\right)+\left(u\frac{\partial P}{\partial x}+v\frac{\partial P}{\partial y}+w\frac{\partial P}{\partial z}\right)+\mu\Phi \qquad (2.29)$$

In 2-domain methods, the Navier-Stokes equations are solved only within the liquid region as the velocity field is set equal to zero at the moving solid/liquid interface. In the 1-domain methods, a fixed grid is defined for the entire system and several procedures have been developed to solve the Navier-Stokes equations in solidifying metals and alloys[5]. Morgan[71] set the velocity field to zero as soon as a certain solid fraction is reached. Gartling[72] progressively increases the viscosity μ in the equation as solidification proceeds. More recently, methods that progressively decrease the velocity field within the mushy zone have been developed[73,74]. In one analysis[74], the average velocity field within the mushy zone can be represented by:

$$v_{eff}=f_s v_s+(1-f_s)v_l \qquad (2.30)$$

2.5 Microstructural Evolution

Microstructure formation during the solidification of alloys is of prime importance for the control of the properties and quality of cast products. In order to predict the properties and the soundness of a casting, empirical methods or trial-and-error approaches have been adopted over the decades. However, due to the complex interactions occurring during solidification, these methods have limited use and hardly can be extended to other solidification conditions. Furthermore, they usually give very little insight into basic mechanisms of solidification. This is particularly the case in equiaxed microstructure formation where nucleation, growth kinetics, solute diffusion and grain interactions have to be considered simultaneously with heat diffusion[75].

As stated in the last chapter, the evolution of solidification microstructures is dependent on the operating nucleation and growth phenomena. The degree of fineness of the microstructure determines the quality and properties of the cast component. The goal of most practical casting

processes is to obtain fine isotropic crystals such that segregation, porosity, and other defects are substantially reduced. Exceptions are precision materials with little or no grain boundaries such as fine wires and extremely thin plates or ribbons/wafers, produced by such unidirectional casting techniques as the O.C.C[76]. These materials are mainly used as lead frames and bonding wires in such appliances as acoustic equipments and memory disks of computers. For these applications, long unidirectionally solidified columnar crystals are preferable, and the fewer the number of crystals, the higher the quality of the cast component.

2.5.1 Nucleation

The classical theory of nucleation is based on the extensive thermodynamic treatment of Gibbs[3]. Gibbs analyzed the transformation of a liquid to a solid phase, taking into account the change of free energy between phases and the free energy change created by the introduction of the new surfaces.

Kinetically, nucleation is a statistical process. A nucleation event may require a long period of time, say one per day, or the nucleation rate may be several hundred per second. The undercooling required for nucleation to occur plays an important role in the nucleation process. Undercooling can originate from either a thermal or constitutional gradient. According to Volmer and Weber[77], two statistical probabilities can be considered:

(a) the probability that an embryo will grow to the critical dimension of a nucleus and

(b) the statistical probability of an atom joining the critical nucleus by transfer from the liquid in a diffusion process.

The nucleation rate is that at which nuclei of critical dimension r^* are converted into stable nuclei of radius, $r>r^*$, by atom attachment from the liquid. This rate is proportional to the product of the two probabilities, (a) and (b).

The rate of heterogeneous nucleation can be written as

$$\frac{\partial N}{\partial t} = n'\gamma \exp\left(-\frac{\Delta G_c^{het}}{k_b T}\right)\exp\left(-\frac{\Delta G_A}{k_b T}\right) \tag{2.31}$$

Taking into consideration that the initial nucleation site density N_s within and around the melt will decrease as nucleation proceeds, Hunt[71] suggested an approximation to the above equation in the form

$$\frac{\partial N}{\partial t} = (N_s - N)K_1 \exp\left(-\frac{K_2}{(\Delta T)^2}\right) \tag{2.32}$$

where $K_1 = \dfrac{n'D_l}{d^2(N_s - N)}$

and $D_l \approx d^2\gamma \exp\left(-\dfrac{\Delta G_A}{k_b T}\right)$

and $K_2 = (\Delta T_n)^2 \ln(N_s K_1)$

Equation (2.32) is based on the assumption of *instantaneous nucleation*, that is, all nuclei are generated at the same time once the critical nucleation temperature is reached. It predicts the same final grain density irrespective of the cooling rate. Experimental results[5,22] have shown that both undercooling and grain density increase with increasing cooling rate. It has been suggested[22] that although most of the variables in the Hunt Model affect nucleation rate, only the initial number of available sites N_s will determine the final grain size. Thus a direct relationship between N_s and the cooling rate is expected. It has been proposed that this relationship can be described by a parabolic equation of the form[22]:

$$N_s = K_3 + K_4\left(\frac{dT}{dt}\right)^2 \tag{2.33}$$

There are two possible explanations for the increase of the number of sites with cooling rate. The first is that because higher undercoolings are reached at higher cooling rates, different

types of nuclei become active, thus increasing the overall number of sites. Secondly, higher undercoolings are associated with a smaller critical radius which in turn results in an increase in the number of active sites.

Other investigators[75,79] assume that nucleation occurs continuously once the nucleation temperature is attained - *continuous nucleation*. Oldfield[79] proposed a parabolic dependence of the number of active nuclei on the undercooling:

$$N = \mu_2(T_n - T)^2 \tag{2.34}$$

which gives a nucleation rate of

$$\frac{\partial N}{\partial t} = -2\mu_2(T_n - T)\frac{\partial T}{\partial t} \tag{2.35}$$

It may be noted that the above is an empirical relationship derived from experimental data on cast iron. It is seen that nucleation rate is a function of both undercooling and cooling rate. Thevoz et al.[75] extended this approach by assuming that at a given undercooling, ΔT, the grain density is given by the integral of the nucleation site distribution from zero to ΔT

$$N = \int_0^{\Delta T} f(\Delta T)d(\Delta T) \tag{2.36}$$

The new grain density is updated at each time step as a function of undercooling with the final grain density corresponding to the onset of recaslescence.

2.5.2 Growth

In metallic systems, growth of the solid from liquid at moderate cooling rates has been observed to occur in three main regimes[9]: planar, dendritic and cellular as illustrated in Fig.

2.7 (a). With respect to the resulting microstructure, growth can either be eutectic or dendritic[8] as depicted in Fig. 2.7 (b). Dendritic growth is by far the most common growth mode in alloys that are not pure eutectics[7,9].

Depending upon the nucleation and heat flow conditions, the growth process could result in either equiaxed crystals (freely growing into an undercooled melt) or columnar crystals (growing into a positive temperature gradient). In the case of equiaxed growth, latent heat created during growth at the solid/liquid interface flows from the interface into the melt (the temperature gradient in the liquid, G_l, is negative) while in the case of columnar growth, heat flows from the liquid into the solid[8] (G_l is positive).

The theories of dendritic growth are based on the same continuity equations, in particular those of heat and solute diffusion which control the macroscopic aspects of solidification. However, unlike macroscopic solidification, a stationary state is considered in this case and additional phenomena such as capillarity, local equilibrium of the various phases and possible kinetic effects may be taken into account. As stated earlier, dendritic growth can be controlled by heat flux, solute flux or both. Columnar dendritic growth is mainly solute diffusion controlled and is common in alloys. On the other hand, equiaxed dendritic growth is heat and/or solute diffusion controlled and can occur in both alloys and pure metals.

Many experimental measurements on free dendritic growth in undercooled melts have been carried out[9]. The early experiments were performed on (a) pure metals[2,80-84] (Sn, Ni, Co, Pb, Ge, Bi), (b) binary alloys[2,83] (Pb-Sn, Ni-Cu) and (c) non-metals[2,85] (P, ice). Also, a great deal of effort[86-88] has been devoted to experimental observations and measurements on a low melting point transparent "plastic crystal", succinonitrile, $NC\text{-}CH_2\text{-}CN$, which facilitates direct observation. Furthermore, some work has been done on constrained or unidirectional dendritic growth in a number of alloy systems[89-96]. All these efforts have provided both morphological and empirical details of dendritic growth, furnishing information on dendrite

tip radius, tip velocity, side branch formation , arm spacing, remelting of dendrite arms, coarsening kinetics, the influence of thermal gradient (G_l), the cooling rate and local solidification time[2,80-97].

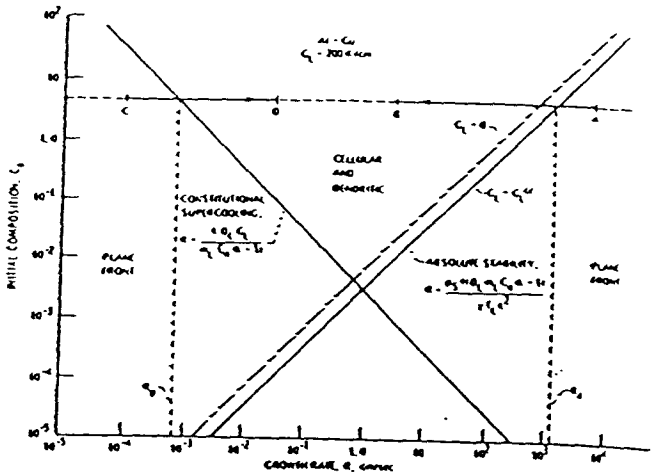

(a)

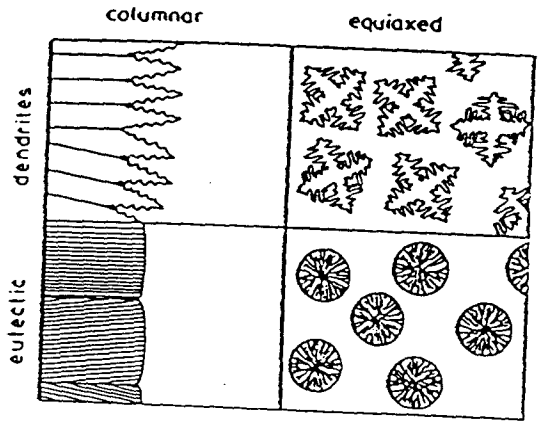

(b)

Fig. 2.7 Growth phenomena during solidification (a) growth regimes[9], (b) growth microstructures[8].

Observations on succinonitrile dendrites[86-88] have shown that the tip regions of dendrites are bodies of revolution very closely approximating a parabola. The cross-section is nearly circular and approximates a body of nearly perfect axi-symmetry. Small undulations appear near the tip which rapidly lengthen into side branches. The point behind the tip, at which the first distinguishable branch appears, varies slowly with the amount of melt supercooling.

Dendritic growth can therefore be considered to proceed by three separate growth processes[7]:

(a) the initial propagation of the primary dendrite stem

(b) evolution of dendrite branches

(c) coarsening and coalescence of dendrite stem and arms.

The initial propagation of the primary dendrite stem is dependent on the stability of the dendrite tip. An early analysis of the growth of a phase by diffusion was made by Zener[98] based on the solid state transformation of ferrite (α) growing from austenite (γ) in the Fe-C system. Assuming the α phase to be a disc with a spherical edge maintained at a radius, r, during transformation, the interface growth velocity can be expressed as:

$$v_t = \frac{D\Omega^2}{2\Gamma} \tag{2.37}$$

where $\Omega = \dfrac{c_i - c_\gamma}{c_i(1-k_p)} = \dfrac{\Delta T}{(\Delta T + m c_\gamma)(1-k_p)}$

and $k_p = \dfrac{c_\alpha}{c_\gamma}$

so that $v_t \propto \Delta T^2$

Following this type of analysis, many studies involving the mathematical description of a branchless geometrical form growing at a constant rate and shape have been carried out[99-104]. The results of these theories express the axial dendritic growth velocity as a power function of undercooling

$$v_t = \beta G^*(\Delta T)^b \tag{2.38}$$

Hence, the driving force for dendritic growth is the tip undercooling. Ivantsov[102] gave a mathematical analysis of the relation of the dendritic growth rate to undercooling in the form:

$$\Omega = \frac{\Delta T}{(\Delta T + m c_0)(1 - k_p)} = Pe \exp(Pe) E_i(Pe) = f(Pe) \tag{2.39}$$

where the Peclet number, $Pe = \frac{v_t r_t}{2D}$

and $E_i(Pe) = \int_{Pe}^{\infty} (e^{-a}/a) da$

Equation (2.39) permits the calculation of the Peclet number, or the product, $v_t r_t$, as a function of undercooling. The tip undercooling is made up of four components[8,9] - thermal (ΔT_t), solutal (ΔT_s), capillarity (ΔT_c) and kinetics (ΔT_k) undercooling, such that

$$\Delta T = \Delta T_t + \Delta T_s + \Delta T_c + \Delta T_k \tag{2.40}$$

In the analysis of Burden and Hunt[89], and later modified by Laxmanan[9], the total tip undercooling, assuming a negligible kinetic effect, is given by

$$\Delta T = \frac{D_l G_l}{R} - \frac{R m_l c_0 (1 - k_p) r_t}{D_l} - k_p G_l r_t + \frac{2\gamma T_L}{\rho_s L r_t} \tag{2.41}$$

The dendrite tip radius, r_t, is estimated from one of the available stability models[99-101,105]. For example, Mullins and Sekerka[100] proposed that a marginally stable state is achieved at the dendrite tip when the tip radius r_t is equal to the perturbation wavelength λ such that

$$r_t = \lambda = 2\pi\sqrt{\left(\frac{\Gamma}{mG_c\xi_c(Pe)-G}\right)} \tag{2.42}$$

Equations (2.39) - (2.42) could then be combined to obtain solutions that give values of the dendrite tip radius, r_t, the dendrite tip velocity, v_t, and the tip undercooling, ΔT.

A knowledge of the growth law of the dendrite tip, that is, the relationship between v_t, r_t and ΔT is not in itself sufficient to predict the final microstructural features and the cooling curves since one still needs to predict how the solid fraction behind the tip changes with temperature. Dendritic growth involves the advance of the dendrite tip into the liquid, and as solidification proceeds, perturbations around the tip may lead to branching. The branching is made more complicated by secondary processes of coarsening and coalescence which determine the final spacing between the dendrite arms. This spacing determines ultimately the distribution of solute on a macro-scale.

2.5.2.1 Dendrite Arm Spacing and Coarsening

Many studies have been made of the "as-solidified" microstructures of binary alloys in order to determine experimentally the interdependence of dendrite arm spacings and solidification parameters[99,106-108]. Also, many analytical solutions have been developed to relate the dendrite arm spacing to solidification variables. In both the theoretical and experimental efforts, a number of solidification parameters have been found to influence the dendrite arm spacing. These include: the temperature gradient near the solidification front, growth rate of the dendrite tip, dendrite tip radius, cooling rate, extent of the mushy zone and the time spent in the mushy zone.

The fineness of the dendritic structure that forms originally has little or no influence on the final dendrite arm spacing due to the coarsening and coalescence phenomena which change the secondary and higher order arms more than the primary arms due to geometrical constraints. The dendrite arms respond to changes in the solidification parameters mentioned above by enlarging their size, merging with others, remelting, shrinking or completely detaching from the parent arm.

Five different models have been proposed to underpin the mechanisms that influence the final dendrite arm spacing as illustrated in Fig. 2.8. These include:

(i) Radial Remelting (Model I): A fine dendritic arm is surrounded by two coarser, identical arms. The smaller arm becomes thinner with time due to lateral dissolution, and shrinks back while the other two arms slightly increase in radius.

(ii) Neck Remelting (Model II): A neck forms at the root of a dendrite arm surrounded by two larger arms. By further remelting at the neck of the arm and freezing at lower curvature sites, the arm becomes disconnected from the main dendrite and gradually spheroidizes.

(iii) Axial Remelting (Model III): A finer dendrite arm surrounded by two coarser arms of equal radii gradually shrinks back at constant radius by dissolution at its tip while the radii of the two coarser arms increase.

(iv) Tip Remelting and Coalescence (Model IV): The tip of two equal arms dissolve and shrinks at constant radii while the concavity between them gradually fills in.

(v) Coalescence (Model V): During the later stages of solidification, juxtaposed arms that have coarsened enough may come into contact with each other and coalesce. The coalescence occurs by preferential solidification in regions of low or negative curvature.

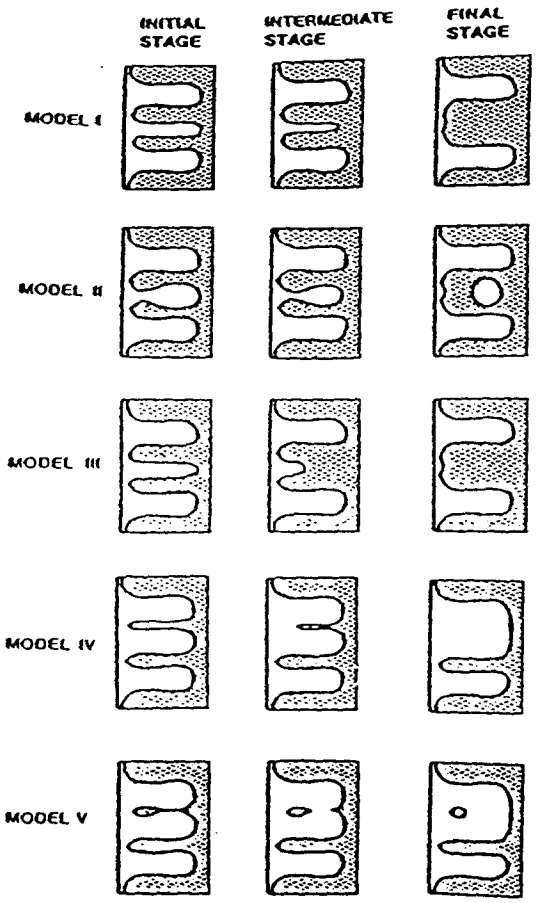

Fig. 2.8 Schematic representation of the different dendrite coarsening models[12].

Most of the theoretical and experimental results have established that the primary dendrite arm spacing (λ_1) could be expressed empirically as:

$$\lambda_1 = C_3 G^{-n_3} R^{-n_4} \tag{2.43}$$

Some of the various theoretical analyses and experimental results are summarized in Table 2.2. It is clear that none of these results have universal application. The form of the

final equation in the theoretical analysis is dependent on the mathematical approximations employed, and on the physical model or models assumed (Models I-V). It is further noted that these analytical theories are based on isolated dendrites.

Table 2.2 Various expressions for the constants used in the evaluation of primary dendrite arm spacing.

Model	n_3	n_4	constant C_3
Trivedi[109]	0.5	0.5	$17.8\sqrt{\frac{D_l\Gamma}{r_t}}$
Hunt[110]	0.5	0.25	$2\sqrt{2}\,[D_l\Gamma\{m(1-k_p)c_0+k_pG_tD_lv_t^{-1}\}]^{1/4}$
Kurz and Fisher[111]	1.0	1.0	$\sqrt{\frac{6(v_t\Delta T_0-G_tD_l)(G_tD_l-k_pv_t\Delta T_0)}{(1-k_p)^2}}$, $v_t < v_c/k_p$
"	0.5	0.25	$4.3\left\{\frac{D_l\Gamma\Delta T_0}{k_p}\right\}^{1/4}$, $v_t > v_c/k_p$
An and Liu[112]	0	0	$2.38\sqrt{\frac{D_lL\Gamma(1-k_p)}{G_tD_l+m(1-k_p)v_tc_0}}$, $v_t < v_c/k_p$
"	0.5	0.25	$1.34\sqrt{L}(D_l\Gamma k_p\Delta T_0)^{1/4}$, $v_t > v_c/k_p$
Rhotagi et al.[93]	0.5	0.5	$\sqrt{8D\Delta T}$
Experimental[106]	0.72	0.24-0.26	29.0 - 34.0 {manganese steel (0.59-1.48%C, 1.10-1.14%Mn)}
Experimental[107]	0.5	0.36- 0.5	30.5 - 56.5 {Al-Cu alloys (2.4-10.1%Cu)}
Experimental[92]	0.45	0.75	{Pb-Sb alloys (5-10%Sb)}

For n_3=n_4 in Eq. (2.43) above, the product of the tip growth rate (R) and the temperature gradient (G) can be represented by one term - the cooling rate since

$$\text{cooling rate} = \frac{\partial T}{\partial t} = \left(\frac{\partial T}{\partial x}\right)\left(\frac{\partial x}{\partial t}\right) = GR \tag{2.44}$$

Then equation (2.43) becomes

$$\lambda_1 \quad \text{or} \quad \lambda_2 \quad = \quad C_4\left(\frac{\partial T}{\partial t}\right)^{-n_5} \tag{2.45}$$

Eq. (2.45) has been used extensively to predict both primary and secondary dendrite arm spacing by many researchers in the field[107,109]. It has been observed that $n_3 \approx n_4$ for secondary arm spacings moreso than for primary spacings[106], thereby making Eq. (2.45) more valid for estimating λ_2 than for λ_1. However, it is noted that the equation does not explicitly incorporate coarsening and coalescence which are the dominant factors in determining the final value of λ_2. Equation (2.45) indicates that the dendrite arm spacing decreases with increasing cooling rate at a given location.

As far back as 1966, Bower et al.[94] have shown that the secondary dendrite arm spacing (λ_2) is proportional to a certain power of local solidification time based on curve-fitting with a variety of experimental results[113-115],

$$\lambda_2 = C_5(t_f)^{n_6} \tag{2.46}$$

Many theoretical models have been developed to account for this result. As in the case of primary dendrites, these models are limited by their mathematical approximations and the physical models used in their derivation. Some of these theoretical models and selected experimental results are summarized in Table 2.3.

These expressions have since been used to predict DAS once the local solidification time is known. The local solidification time is defined as the time spent in the mushy zone,

that is, the time required for the temperature at a point in the liquid metal to pass from the liquidus to the solidus temperature. It is often measured but can also be calculated with great difficulty (the liquidus is difficult to pinpoint) from a heat transfer model of the casting process.

Table 2.3 The various expressions for the constants used in the evaluation of secondary dendrite arm spacing.

Model	n_6	constant C_5
Kattamis et al.[96]	1/3	$\left\{\dfrac{\gamma_{sl} D T_L}{L m C_l (1-k_p)\phi(f_s)^2 \ln(1-f) f}\right\}^{1/3}$
Fuerer and Wunderlin[116]	1/3	$\left\{\dfrac{166\Gamma D_l \ln(c_e/c_0)}{m(k_p-1)(c_e-c_0)}\right\}^{1/3}$
Kirkwood[117]	1/3	$\left\{\dfrac{128 D_l \gamma_{sl} T_L \ln(c_e/c_0)}{L_v m(k_p-1)(c_e-c_0)}\right\}^{1/3}$
Mortensen[118]	1/3	$\left\{\dfrac{27\Gamma D_l}{4c_l(-m)(1-k_p) f_s (1-\sqrt{f_s})}\right\}^{1/3}$
Voorhees[119]	1/3	$\left\{\dfrac{8T\alpha_l D \gamma_{sl} f_s}{9L[DL/C_p-(1-k_p)m c_l \alpha_l]}\right\}^{1/3}$
Experimental[50]	0.43	11.5-15.3 x 10^6 Al-Si alloy (3.8-9.7% Si)
Experimental[94]	0.39	7.5 x 10^6 Al-4.5% Cu alloy

Wolf and Kurz[120] have shown that an equivalent expression can be obtained by correlating the macroscopic shell growth with DAS. Employing the square root time law for shell growth,

$$S = K\sqrt{t} \tag{2.47}$$

the relation between DAS and cooling rate {Eq. (2.45) above}, an analytical solution from Szekely et al.[121] and other assumptions, they obtained the following expression for DAS:

$$\lambda_2 = C_4\left(\frac{4t}{BK^2}\right)^{n_5} \approx C_4\left(\frac{t_f}{T_L - T_S}\right)^{n_5} \tag{2.48}$$

where $B = \frac{\rho_s L}{k_s}$

Based on the same kind of derivations and assumptions, the secondary dendrite arm spacing has also been related to the distance from the chill surface by the following expression[107,122]

$$\lambda_2 = C_6(S)^{n_7} \tag{2.49}$$

where $C_6 = C_5\left\{2\frac{(K_L - K_S)}{K_{shell}^3}\right\}^{(1/3)}$

and $n_7 = 2/3$

With either of the models, it is possible to predict DAS by simply solving the heat transfer equations to obtain the solidification time or shell thickness at various distances from the chill. However, the characterization of various constants for each alloy system still constitute a major barrier to this laudable goal.

Another fundamental work in coupling the microstructure with heat transfer and fluid flow is the recent one by Hills[123]. Employing Eq. (2.45) with $n_5 = 1/3$, and the relationship between the cooling rate at the critical region just behind the dendrite tips and the growth rate,

$$\frac{dT}{dt} = -\frac{\rho L}{k_s}R^2 \tag{2.50}$$

Hills obtained expressions that directly linked the dendrite arm spacing to known heat transfer parameters. For castings in a mold without convective cooling, DAS could be expressed as a function of shell thickness, solidification time, and the ratio of heat absorbing powers of solidifying metal and mold material in the form:

$$\lambda_2 = \frac{1.35 C_4 H^*}{\beta^{3/4}(\alpha_s T_L)^{\frac{1}{3}}}(P^* t)^{\frac{2}{3}} \tag{2.51}$$

where

$$H^* = \frac{L}{C_s T_L}$$

$$P^* = \frac{k_s \rho_s C_s}{k_m \rho_m C_m}$$

$$\beta = f(P^*, H^*)$$

In the case of convective cooling conditions, the temperature of the fluid can be used as a zero reference temperature such that DAS can be expressed as a function of interfacial heat transfer coefficient, solidification time, and the ratio of heat absorbing powers of solidifying metal and mold material in the form:

$$\lambda_2 = C_4 \left[\frac{L \rho_s k_s}{h^2 T_L^2} \right]^{\frac{1}{3}} \exp\left[0.53 \left(\frac{Y^*}{\sqrt{H^*}} \right)^{\frac{1}{2}} \right] \tag{2.52}$$

where $$Y^* = \frac{\varepsilon}{(H^* + 0.55 H^{*(1/4)} \sqrt{\varepsilon})}$$

and $$\varepsilon = \frac{h^2 t}{\rho_s k_s C_p}$$

Hills[123] further linked the dendrite arm spacing to segregation and interdendritic fluid flow. Hills model is unique in that it links DAS to distance from chill surface, solidification time, heat transfer coefficient and other characteristics of the mold and casting.

2.6 Coupling Heat Transfer and Microstructural Evolution

Section 2.5.2.1 has presented the interdependence between macroscopic heat transfer during solidification and microstructural evolution. It is obvious that the phenomena (heat and mass transport) at the dendrite tip control the dynamics of the mushy zone which in turn affect events in the single phase regions (liquid and solid). The final dendrite arm spacing has been expressed as a function of microscopic parameters (tip radius, temperature near the tip, tip velocity, tip undercooling) as well as macroscopic parameters (fraction solid, local solidification time, shell thickness and heat transfer coefficient).

Microscopic and macroscopic models can be coupled via an appropriate determination of solid fraction at any stage in the solidification process. This is often achieved by evoking a solute diffusion model. The distribution of solute between the solid and liquid is influenced by the diffusion of solute in the liquid, diffusion in the solid, convection, turbulence and physical effects involving the incorporation of atoms into an advancing interface. The solute rejected into the liquid during solidification builds up a boundary layer near the solidification front. The actual transfer of solute to the solid is related to the solute content in the liquid near the interface.

Solute diffusion models are mainly of two types depending on the assumptions employed in the solution of mass transport during solidification;

(a) complete mixing models

(b) diffusion models

2.6.1 Complete Mixing Models

Two basic assumptions are made in the formulation of these models:

(i) dendrite tip undercooling is negligible such that the liquid to solid transformation begins and ends at the equilibrium liquidus and solidus temperatures respectively.

(ii) there is complete mixing in the liquid even in the vicinity of the dendrite tip such that no concentration gradient exists in the liquid.

The expressions for the fraction solid obtained from some of the commonly used complete mixing models are shown in Table 2.4. These models are at best first approximations and are very useful for columnar growth in most solidification processes where the cooling rate is not high enough to produce any appreciable undercooling. It is worth noting that equilibrium transformation is an uphill task since thermodynamic considerations require a temperature gradient between the two phases for transformation to proceed.

2.6.2 Solute Diffusion Models

Solute diffusion models take into account the dendrite tip undercooling and solute concentration gradient in the liquid during solidification. The aim is to obtain the solid fraction as a function of not only the temperature but also the dendrite tip velocity. The models are very useful for modeling equiaxed growth and have been used for columnar growth under conditions of rapid cooling[5].

For columnar growth, the commonly used solute models[126-128] are mere derivations of the complete mixing models discussed above. This is due to the fact that the region of non-complete mixing is limited to a small liquid region near the dendrite tip. In one such model[126], the Scheil relationship truncated at the dendrite tip was applied to study columnar-to-equiaxed transition. Although such an approach has the advantage of being easily implemented in heat flow calculations, it does not satisfy an overall solute flux balance[5].

Another model[127] takes into account the solute layer close to the dendrite but only along the growth direction with an assumption that the fraction solid increases linearly with time. Kurz et al.[128] proposed a model based partly on the Brody and Flemings[95] derivations. They assumed that beyond a certain concentration and a corresponding solid fraction, there is complete mixing and incomplete mixing below this point.

Table 2.4 The various complete mixing models for the evaluation of fraction solid during solidification.

Model	Solid Fraction (f_s)
Lever Rule	$\frac{1}{1-k_p}\left(\frac{T_L-T}{T_L-T_S}\right)$
Scheil's Model[124]	$1-\left(\frac{T-T_S}{T_L-T_S}\right)^{\frac{1}{1-k_p}}$
Clyne and Kurz[125]	$\frac{1}{1-2Fo'k_p}\left[1-\left(\frac{T-T_s}{T_L-T_S}\right)^{\left(\frac{1-2Fo'k_p}{1-k_p}\right)}\right]$ where $Fo' = Fo[1-\exp(-Fo^{-1})]-0.5\exp(-0.5Fo^{-1})$ and the Fourier Number, $Fo=\frac{D_s t_f}{x^2}$
Brody and Flemings[95]	$1-\left[\frac{c_s(k_p-1)-ac_0k_p}{k_pc_0\{k_p(1-a)-1\}}\right]^{\frac{1}{1-k_p}}$ where $a=\frac{D_lG_l}{m_lv_lc_0}$

For equiaxed growth, the solid fraction is simply the product of grain density and the grain volume. If the grain is considered to be a sphere, then the basic equation for the solute model is given by

$$f_s(x,t) = N(x,t)\frac{4}{3}\pi r^3(x,t) \tag{2.53}$$

The above equation can be solved easily for equiaxed eutectics by evaluating N(x,t) and r(x,t) from nucleation and growth laws. However, the solution is complicated for equiaxed dendritic solidification since a dendritic grain is not fully solid within the mushy zone. In this case, the solid fraction expression becomes a function of the dendritic grain fraction (f_g) and an internal solid fraction (f_i). For example, in the model developed by Rappaz and Thevoz[129,130], the total solid fraction was assumed to be composed of two components:

(i) the internal volume fraction which depends on the variation of temperature with time

(ii) the grain volume fraction that depends on the kinetics of the dendrite tip

Under these conditions, the total volume fraction is given by

$$\Delta f_s(x,t) = \Phi(x,t)\,(T^{t+\Delta t} - T^t + \Omega(x,t)v_t(\Delta T^t)\Delta t) \tag{2.54}$$

where $$\Phi(x,t) = \frac{N(x,t)\frac{4}{3}\pi r^3 f(Pe)}{m c_0(1-k_p)}$$

and $$\Omega(x,t) = \frac{N(x,t)4\pi r^2 f(Pe)\,(c-c_0)}{c(1-k_p)}$$

and $$f(Pe) = 1 + \frac{3}{2Pe} + \frac{1}{Pe^2} + \frac{1}{4Pe^3} + \ldots$$

Chapter 3

SCOPE AND OBJECTIVES

3.1 Objectives/Importance

It is evident that the evolution of the desired microstructure during casting is ultimately linked to all processes that contribute to solidification, such as heat and mass transfer and fluid flow. Furthermore, the casting properties which determine the suitability of a cast product for a given application are strongly dependent on the microstructure. An efficient solidification model that links the microstructure to known casting conditions, coupled with structure-property models, will be invaluable in the following respects:

(i) appropriate selection of casting parameters for a given set of properties and applications or conversely, prediction of expected microstructure and consequently, casting properties for a given set of casting conditions.

(ii) contribution to the development of nondestructive testing techniques to evaluate the dendrite arm spacing variations within a casting and correlate with other property measurements as a quality control tool.

This work focuses on the coupling of heat transfer phenomena and the resultant microstructure at the early stages of solidification. There are three main objectives of this endeavor:

(1) To characterize the transient heat flux, heat transfer coefficient and shell growth at the very early stages of solidification utilizing dip experiments;

(2) To characterize the evolution of the dendritic structure in terms of the secondary dendrite arm spacing during this period;

(3) To establish models and/or validate existing models that directly link the microstructure, particularly the dendrite arm spacing to known heat transfer parameters.

The ability to define processing conditions to obtain an optimum microstructure in the solidified material is the key aspect of the design of many technologically important processes, including casting, welding, single crystal preparation and rapid solidification techniques. For dendritic solidification, the microstructure is often quantified in terms of the dendrite arm spacing. The difficulties of modeling dendritic solidification are due mainly to the fact that heat and mass transport equations have to be solved simultaneously at three levels- the microscopic dendrite tip, mushy zone and the single phase domain (liquid or solid). At the dendrite tip, nucleation and growth phenomena influence the latent heat and solid fraction evolution. At the mushy zone, heat and mass transport are influenced by the solid fraction and the coarsening phenomena. The single phase domain is mainly controlled by the local cooling rate which in turn depends on the events at the other zones and the boundary surfaces.

3.2 Methodology

Unidirectional solidification was chosen for this study because of its simplicity and the fact that it promotes the growth of dendrites in a single direction of heat flow. The characterization of the dendrite arm spacing is thus easier. A dipping mechanism was chosen over the usual teeming technique in an attempt to reduce the influence of convection that results from pouring. Furthermore, dipping is conceived to be a better simulation of some casting processes (such as melt drag in near-net-shape casting) where the mold moves to make the initial contact with the molten metal.

In dip experiments as in many dynamic heat transfer situations, the heat transfer parameters at the surface are easier to determine from transient measurements at one or more interior locations. Such problems are classified as inverse heat conduction problems (IHCP) which, as

mentioned earlier, alleviate the difficulties associated with surface measurements. The general methodology consists of four stages as illustrated in Fig. 3.1 - design and fabrication, mathematical modeling, experimental campaigns and process analysis.

The first stage involved the design, fabrication and instrumentation of a practical unidirectional solidification apparatus based on the dipping mechanism. A water cooled chill instrumented with thermocouples and mobile to permit dipping into a melting chamber was desired. Two mathematical models were developed to simulate heat transfer in the chill and casting respectively. A third model was applied to the prediction of secondary dendrite arm spacing (SDAS) from known heat transfer parameters. Then experimental campaigns were undertaken utilizing four different chill materials dipped into Al-Si alloy melt (3-7 %). The following variables were investigated - chill material, chill surface roughness, superheat, alloy composition, bath height and oil film. Finally, the results of the experiments were analyzed and model predicted values were compared with measurements.

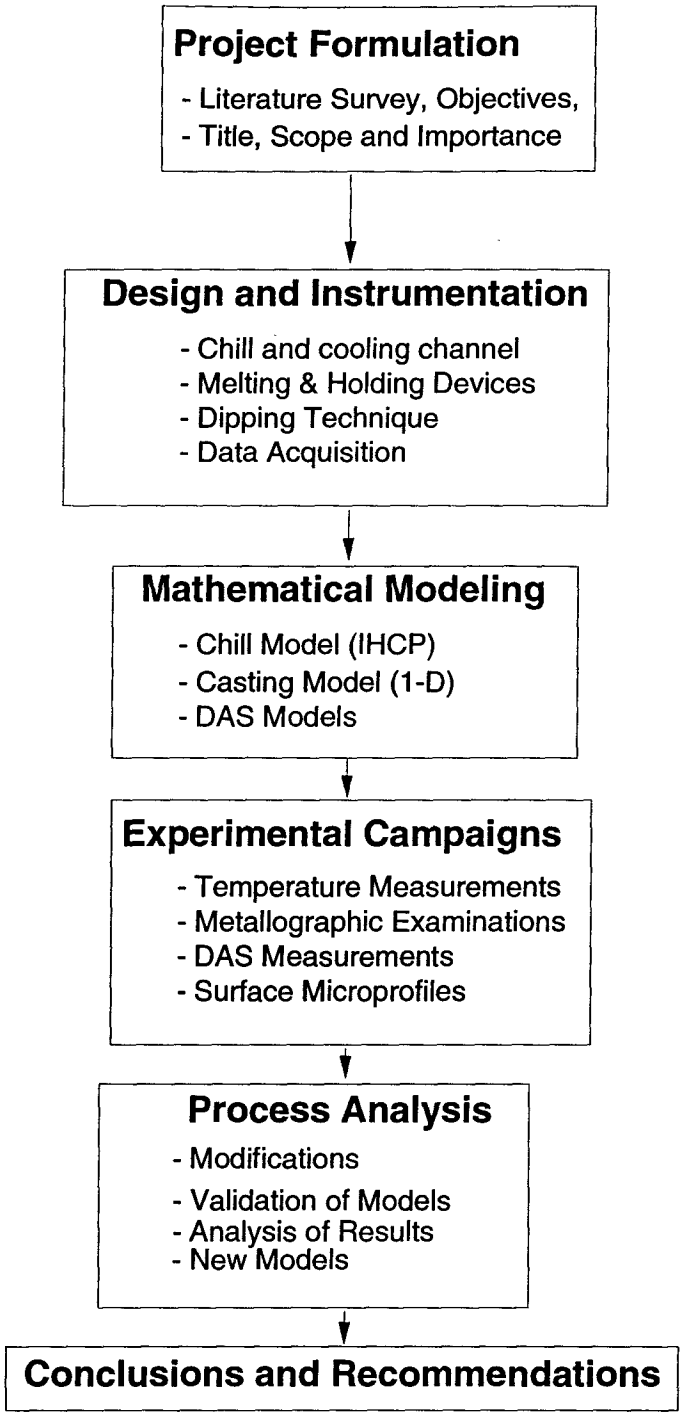

Fig. 3.1 Schematic illustration of the project methodology.

Chapter 4

EXPERIMENTAL PROCEDURE AND RESULTS

The experimental part of this work was carried out in three steps:

(i) design, fabrication and instrumentation of mold and cooling systems

(ii) dipping campaigns

(iii) metallographic examination and DAS measurements

4.1 Design

The experimental apparatus is shown schematically in Fig. 4.1. The apparatus was made up of four major parts - the melting chamber, the chill, the cooling and the data acquisition systems. The cooling system consisted of a rectangular water channel connected to two 13mm diameter water pipes serving as the inlet and outlet for the cooling water. The top plate was fabricated out of transparent plexiglas to allow direct observation of water flow and had six 3.1mm diameter holes to permit the passage of thermocouples from the chill to the data acquisition system. The bottom plate of the water channel had a threaded hole at its center such that the chill could be screwed into it. The chill was essentially an insulated cylindrical metallic rod with exposed ends. A small part of the upper half (6.35mm) was threaded to fit into the bottom plate of the cooling channel.

Commercial purity copper rod was used as the chill for most of the experiments. Cast iron, brass (70%Cu-30%Zn) and low carbon steel rods were used to study the effects of different chill materials on heat transfer and cast structure. For each experiment, the chill was insulated with 2mm thick fiberfrax that was held in place with 5μm iron wires tied tightly around the chill (fiberfrax of original thickness 5mm compacts to a final thickness of 2mm after fastening). In order to ensure good adherence between the solidified shell and the chill, two small pieces of

steel plate (20mm x 2.5mm x 0.5mm) were tied around the chill with thin iron wires (10μm thick) and the protruding ends (about 5mm) were bent into an L-shape to serve as hooks. The solidified shell adhered to these hooks and also to the thermocouple in the melt, such that the shell could be lifted with the chill assembly. It was confirmed from calculations and measurements that these hooks did not affect heat transfer and microstructure in any tangible way.

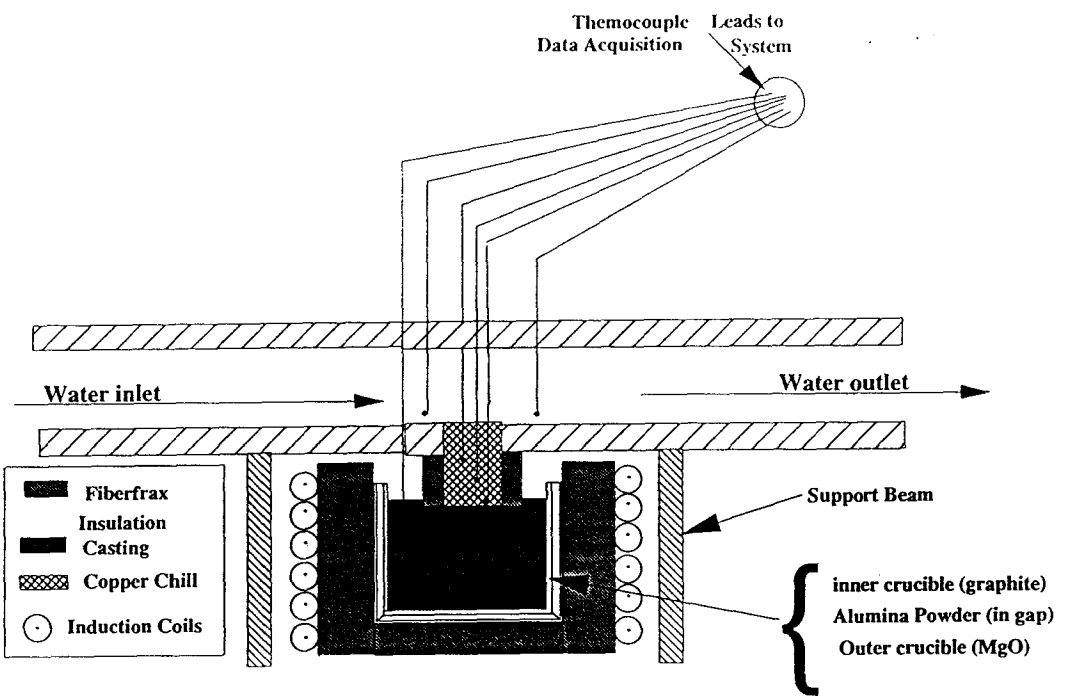

Fig. 4.1 Schematic representation of the experimental set-up.

A Phillips high frequency coreless induction furnace (0-12KW power, 0-110KHz) was utilized for melting. A graphite crucible was used both as the container for the casting and as a susceptor of the electromagnetic field. The graphite crucible was insulated by inserting it into a MgO crucible of slightly larger dimensions and packing any available space between them

with fine particles of alumina. Furthermore, the outer MgO crucible was wrapped with 5mm thick layer of fiberfrax. Preliminary measurements indicated that the heat losses from the insulated surfaces accounted for less than one percent of the total heat loss by the solidifying metal.

Al-Si alloys were melted in a graphite crucible and the water-cooled chill was dipped into the melt at a known superheat while the data acquisition system recorded the temperature profiles at various locations in the chill and solidifying metal. Details of the equipment are summarized in Table. 4.1.

Table 4.1 Some details of the experimental design.

Component	Material	Dimension
Cooling Channel (Rectangular Box)	Top Plate:plexiglas Other Sides:stainless steel	Outside: 300mm x 65mm X 62mm Water Channel: 285mm x 52 mm x 12.7 mm
Chill (Cylindrical Rod)	Commercial purity copper, cast iron, 70%Cu-30%Zn brass, low carbon steel.	Diameter: 28.6mm Height: 28.6mm
Induction Unit	Coil: 9mmϕ Cu tube	Internal Diameter: 95mm Height: 165mm No. of Turns: 10
Crucible	Graphite	Internal Diameter: 35mm Thickness: 10mm Height: 15 mm
Thermocouples	Chromel-Alumel Type K	Diameter: 20μm Average Bead Diameter: 1mm
Data Acquisition	Notebook on Compaq or Metrabyte	Frequency: 2Hz
Casting Alloys	Al - 7% Si Al - 5% Si Al - 3% Si	-

Consider the electrical analogue shown in Fig. 4.2 in which it is desired that $R_{ch/c} >> R_{f/ch} + R_{ch}$, i.e. $R_{f/ch}$ and R_{ch} have to be minimized. This was achieved by a proper design of the cooling water channel since the chill resistance, R_{ch}, was limited by the chill thermal conductivity and the chill height. The cooling water channel was designed to ensure the following:

(i) enough water velocity such that $h_f >> h_c$.

(ii) fully developed flow near the chill surface

(iii) no appreciable recirculation or stalling near the chill surface.

These goals were attained with the dimensions given in Table 4.1 and a water velocity of 2.0 m/s such that the thermal resistance at the chill/casting interface constituted more than 70% of the total resistance for the whole duration of an experiment. A typical variation of the thermal resistances during solidification is presented in Fig.4.3 for Al-7%Si and copper chill.

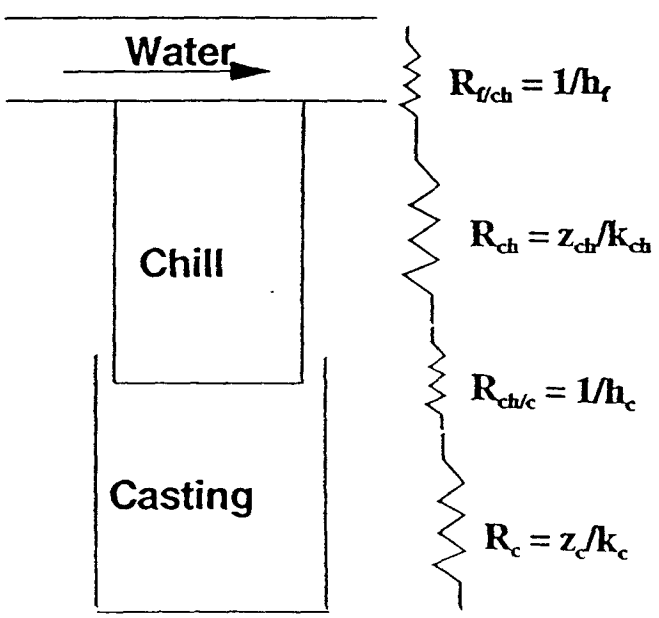

Fig. 4.2 Schematic illustration of the operating thermal resistances.

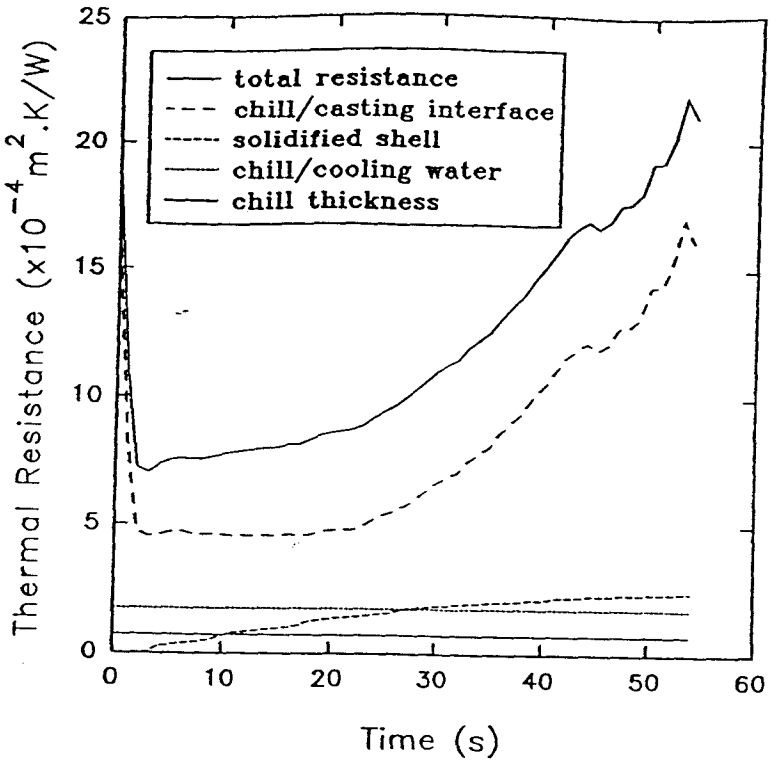

Fig. 4.3 Estimated variation in thermal resistances for Al-7% Si alloy and copper chill.

4.2 Instrumentation and Data Acquisition

The chill was instrumented with three thermocouples located at 1.6mm, 3.2mm and 22.2mm respectively from the hot face. The thermocouples with the beads bent into a slight L-form, were tightly secured in place in 2mm holes drilled at the center of 6.4mm diameter screws. The screws were made of the same material as the chill and were tightened until the the thermocouple beads could no longer move. A fourth thermocouple (in stainless steel sheath) attached to the chill insulation monitored the casting temperature at a preset location (12mm from chill /casting interface).

For each experiment, the thermal responses of the thermocouples were recorded with either a COMPAQ Type 18 computer (with 32-channel data board) or a Metrabyte Computer

(128-channel board) using Notebook 3.1 software. Preliminary measurements were made to determine the experimental time step and the frequency of data acquisition. An experimental time step of 0.5s (2Hz frequency) was finally adopted since no significant loss in the general trend of the thermal responses was observed within this time interval. The thermocouples were calibrated by immersing them into two mediums of known temperature - melting ice/water mixture and boiling water. The thermal response and standard deviations from the boiling water test is shown in Table 4.2. The approximate response time of the thermocouples was estimated from this test as 0.13s. It is noted that chromel-alumel thermocouple (type K) used for the experiments has a design specification of $\pm 2.2°C$ error limit between 0°C and 1250°C, with the upper end of the error operating at lower temperatures[131].

Table 4.2. Thermal response of four thermocouples (TC1-TC4) during calibration in boiling water ($B.P. \approx 100°C$ at 1 atm. pressure).

Time (s)	Temperature (°C)			
	TC1	TC2	TC3	TC4
5	101.3	101.3	102.5	102.5
10	101.3	102.4	101.3	101.3
15	101.2	101.3	101.3	102.5
20	102.6	101.3	101.3	102.5
25	101.3	102.5	101.3	101.3
Mean	101.6	101.8	101.6	102.1
Standard Deviation	0.5	0.6	0.5	0.6
Error	1.6	1.8	1.6	2.1

4.3 Dipping Campaigns

The chill surface was polished with different grades of abrasive paper or was filed in order to obtain various degrees of surface texture. The surface roughness and surface microprofiles

were measured with a digital Talysurf 5 System[132], a stylus-type device that is capable of measuring both the roughness and waviness components of the surface texture. Although surface roughness can be measured in terms of amplitude parameters (measure of the vertical displacements of a given profile) or spacing parameters (measures of the irregularity spacings along the surface, irrespective of the amplitude of these irregularities), the arithmetic mean of the departures of the amplitude profile from the mean line (Ra in μm) is the universally recognized, and most used, international parameter of roughness[132]. Hence, surface roughness was quantified in terms of the Ra values in this study. With reference to Fig. 4.4, Ra is defined as:

$$Ra = \frac{1}{l}\int_0^l Y(x)dx \tag{4.1}$$

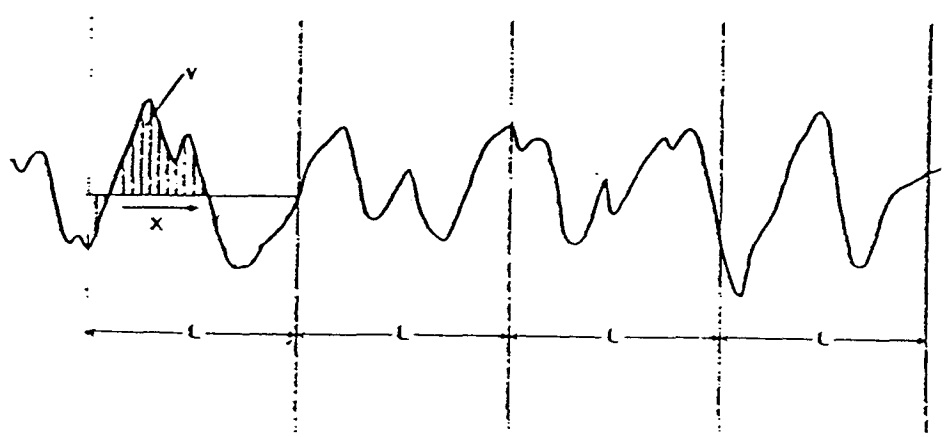

Fig. 4.4 Schematic representation of surface microprofile measurement.

Before each dipping campaign, the chill surface was prepared to obtain the desired roughness before dipping. In some of the experiments, a thin film of oil was applied uniformly to the chill surface before dipping. The properties of the oils used are shown in Table 4.3. The

chill and cooling system was meticulously sealed with liquid silicone to prevent water leaks. The data acquisition was turned on after running the cooling water through the cooling channel for a few minutes. Each thermocouple response was compared with a measurement made with a high-accuracy hand held digital thermometer[131] (Omega CL23 calibrator / thermometer). Faulty contacts were revealed at this stage and were corrected immediately.

Table 4.3 Properties of the oils used in the experiments.

Properties	Canola	HEAR	Steelskin	Blachford	
Viscosity @ 38°C (SUS)	160	185	200	214	
Flash Point (°C)	>315	>300	226	200	
Fire Point (°C)	>360	>350	252	-	
Boiling Point (°C)					
Start	205	215	170	-	
20%	280	280	230	-	
50%	315	320	300	-	
90%	335	335	330	-	
Fatty Acid Content					Carbon Chain**
Palmitic (%)	5.3	3.2	2.9	4.2	C16:0
Oleic (%)	57.7	14.9	40.3	61.5	C18:1
Linoleic (%)	23.6	15.1	27.1	19.6	C18:2
Linolenic (%)	9.2	9.3	26.0	9.7	C18:3
Eicosenoic (%)	0.7	8.2	0.3	0.7	C20:1
Erucic (%)	0.3	45.2	0.1	0.6	C22:1
Others (%)	3.2	4.1	3.3	3.7	-

** C18:1 implies 18 carbon atoms with one double bond in the chain.

Small pieces of the alloy to be cast were weighed (the weight depends on the desired bath height) and placed inside the graphite crucible. Three Al-Si alloys were utilized: Al-7%Si, Al-5%Si and Al-3%Si. The induction machine was started and melting was achieved within a few minutes; further heating raised the temperature of the melt well above the desired superheat.

The induction machine was turned off while a thermocouple encased in a mullite tube and connected to the high-accuracy hand held digital thermometer was immersed in the melt to monitor the superheat. The oxide layer at surface of melt was scooped off manually before dipping since attempts to reduce oxidation either by argon blowing or by addition of Na_2AlF_3 did not yield positive result due to the high oxidation rate of aluminum alloys.

Once the desired superheat was attained, the chill/casting contact was achieved by dipping the chill and cooling channel assembly into the melt to a predetermined depth. Different depths were experimented with and it was observed that the thermal response was more stable within a range of 2mm - 8mm. At depths less than 2mm, it appears that the thin surface oxide was not displaced enough to allow for a good initial chill/melt contact. At depths greater than 8mm, excessive burning of the fiberfrax insulation on the chill was noticed, leading to an increase in transverse heat transfer. Hence, the chill depth inside the melt was maintained at approximately 5mm throughout the experiments. Three different dipping methods were tested - placing the chill/cooling system assembly on preset beams, using clamps to hold the assembly in place, and the use of a laboratory jack. No significant difference was observed between the thermal response of the three methods. Hence, the first of the three methods was adopted.

The casting and chill were left in contact for about 60 seconds for each experiment. The solidified shell thickness was measured after cooling to room temperature. The surface roughness of the solidified shell was also measured with the Talysurf 5 System[132]. To ensure the reproducibility of results, at least two trials were conducted for each set of conditions. The results were observed to be reasonably reproducible as illustrated by Table 4.4 with standard deviations ranging from 0.7 to 4.9.

Table 4.4 The measured thermal response at one location for three trials under the same condition.

Time (s)	Trial 1 (°C)	Trial 2 (°C)	Trial 3 (°C)	Mean (°C)	Standard Deviation
0	15.3	17.7	16.5	16.5	1.0
5	66.5	70.0	58.3	64.93	4.9
10	120.5	121.7	119.3	120.5	1.0
15	130.2	133.7	136.2	133.4	2.5
20	142.2	150.7	143.6	145.4	3.7
25	147.1	151.9	147.1	148.7	2.3
30	148.5	148.3	143.6	146.8	2.2
35	147.1	148.4	142.2	145.9	2.6
40	143.4	145.9	141.0	143.4	2.0
45	135.0	139.9	135.0	136.6	2.3
50	118.1	127.9	123.2	123.1	4.0
55	115.7	113.3	112.9	114.0	1.2
60	114.6	113.3	112.9	113.6	0.7

4.3.1 Thermal Response of the Thermocouples

The thermal responses obtained for the dipping campaigns are as shown in Figures 4.5 to 4.11. It is apparent that the temperature at a given location in the chill rises steeply upon contact with the melt up to a peak value and then decreases as solidification progresses until a fairly steady state value is attained. On the other hand, the temperature at given location in the casting decreases continuously with time as indicated in Fig. 4.5. The temperature profile in the chill decreases with increasing roughness of the chill surface (Fig. 4.6) and decreasing thermal diffusivity of the chill material (Fig. 4.7). Increasing the superheat increases the temperature at a given location in the chill as depicted in Fig. 4.8. The temperature profile in the chill increases with decreasing silicon content (Fig. 4.9). The effect of the oils on the temperature profile in the chill is depicted in Fig. 4.10. The four oils utilized in this study decreases the chill temperature for a few seconds (< 10 s) but finally increase this temperature

beyond the value attained with no oil. Canola and HEAR oils appear to influence the chill temperature more than the other two. The chill temperature also decrases with decreasing bath height as shown in Fig. 4.11. The reason for each of the observed results are discussed later in Chapter 6.

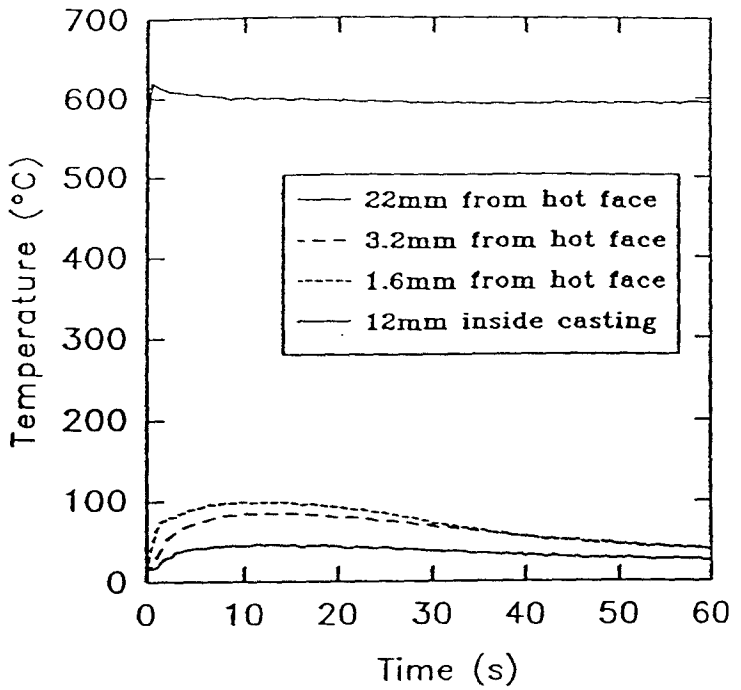

Fig. 4.5 Typical temperature data during the casting campaigns for Al-7%Si alloy and copper chill.

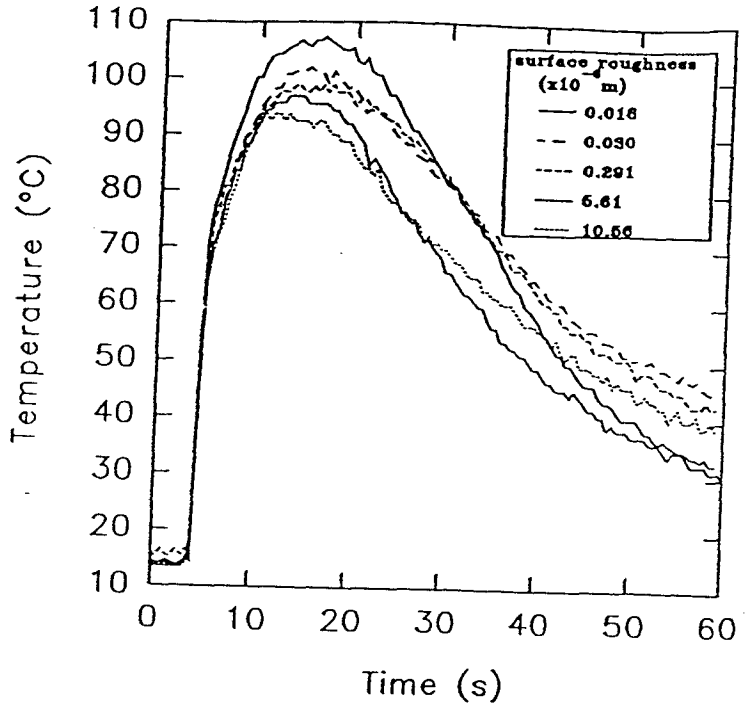

Fig. 4.6 **Effect of surface roughness on measured temperature response of the chill (copper) at 1.6mm from chill/casting interface for Al-7%Si alloy.**

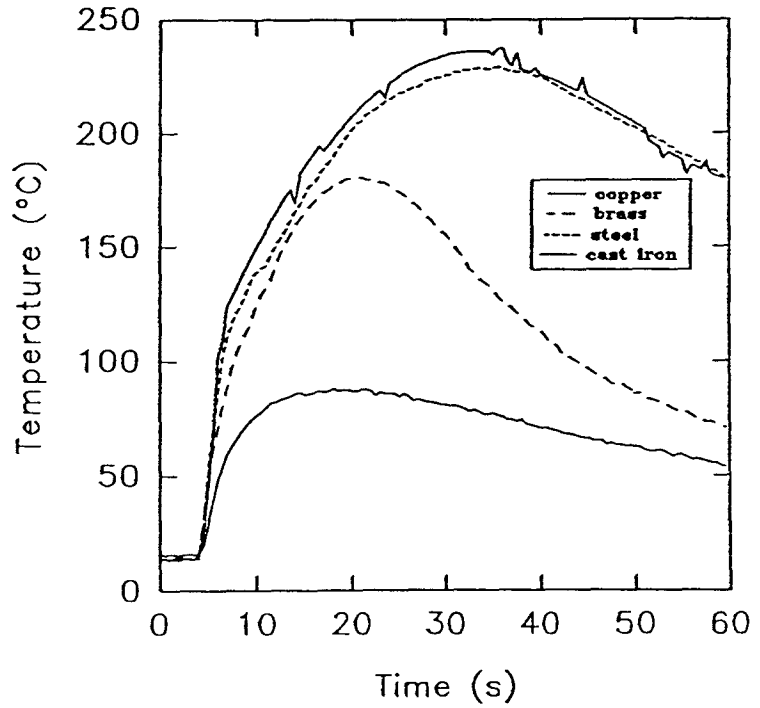

Fig. 4.7 **Effect of chill material on measured temperature response of the chill at 1.6mm from chill/casting interface for Al-7%Si alloy.**

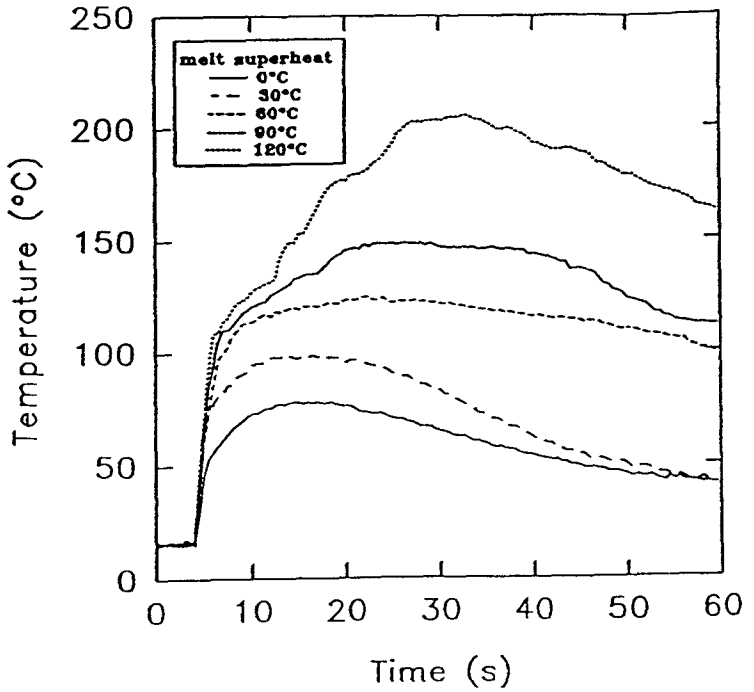

Fig. 4.8 **Effect of superheat on measured temperature response of the chill (copper) at 1.6mm from chill/casting interface for Al-7%Si alloy.**

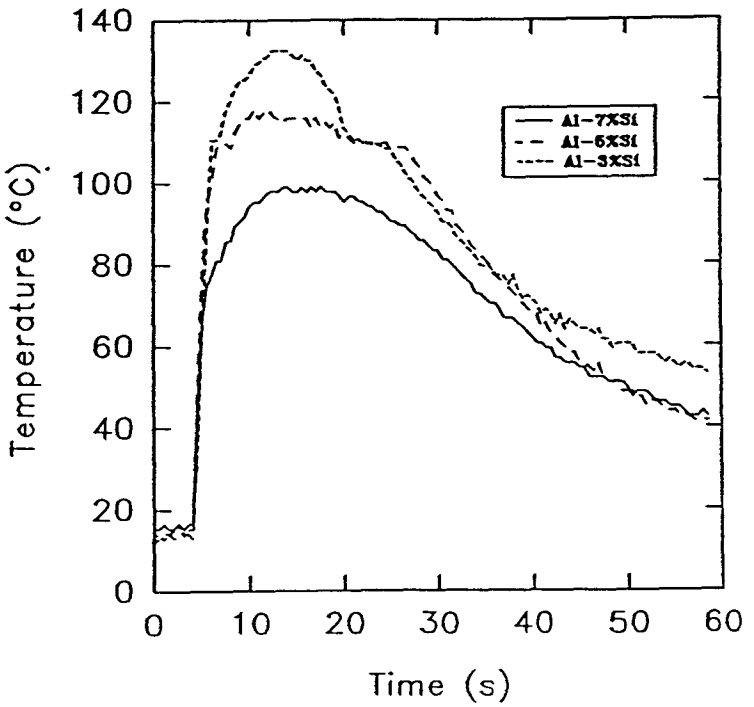

Fig. 4.9 **Effect of alloy composition on measured temperature response of the chill (copper) at 1.6mm from chill/casting interface.**

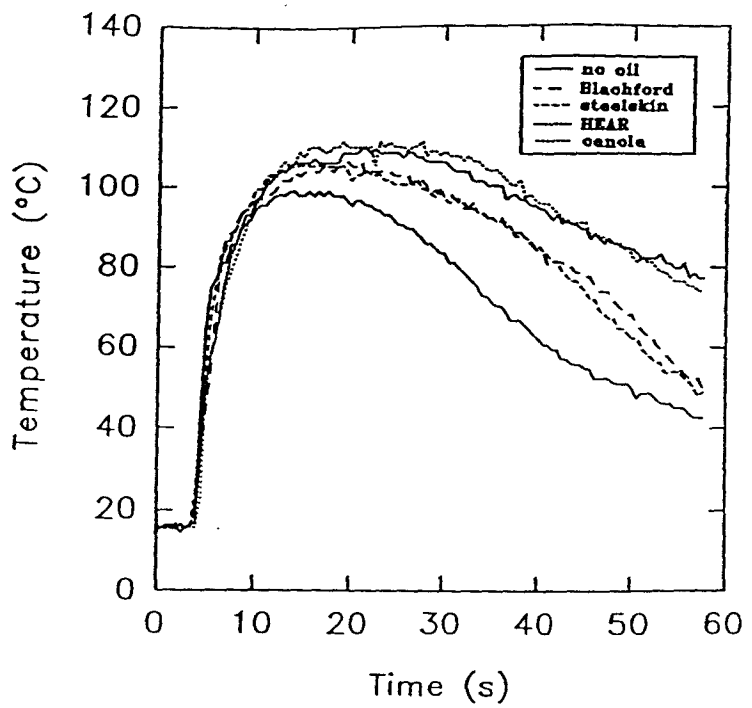

Fig. 4.10 **Effect of oil film on measured temperature response of the chill (copper) at 1.6mm from chill/casting interface.**

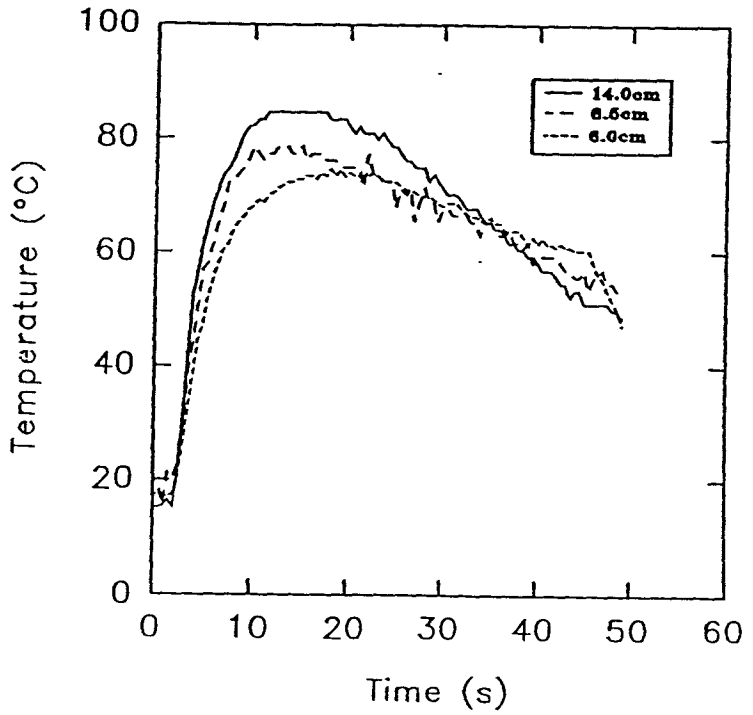

Fig. 4.11 **Effect of bath height on measured temperature response of the chill (copper) at 1.6mm from chill/casting interface for Al-7%Si alloy.**

4.4 Metallographic Examination

Longitudinal specimens were cut from the center of the solidified shells for metallographic examination. The specimens were mounted, ground and polished to 0.06μm surface finish. The Al-Si alloys were etched in Kellers reagent (1%HF-1.5%HCl-2.5%HNO_3-95%H_2O) for about 30 seconds to reveal the dendritic solidification structure. The specimens were then examined with a metallurgical microscope and micrographs taken at various distances from the shell/chill interface. Typical micrographs are depicted in Fig. 4.12.

The secondary dendrite arm spacing were measured from magnified micrographs or metric microscope utilizing a combination of the two common DAS counting methods - the line intercept and individual arm counting methods.

In the line intercept method, a line parallel to the primary arms was drawn and the number of secondary arms were counted along one side of this line for short intervals of length (l). At least five measurements were made at any given distance from the surface. The average secondary dendrite arm spacing (SDAS) at a given mean distance is then given by

$$SDAS(\bar{l}) = \left(\frac{l}{\text{No. of Secondary Arms}} x \frac{1}{\text{Magnification}} \right) \tag{4.2}$$

In the individual arm counting method, the primary arms were identified and the distance between the centers of adjacent secondary arms was measured. At least five measurements were made at a given distance from the surface and the average of these measurements was taken as the secondary arm spacing at the given location. Results of a typical SDAS measurement together with the associated standard deviation is shown in Table 4.5. Figure 4.13 shows a typical variation of measured secondary dendrite arm spacing with distance from surface. The effects of various variables on SDAS are depicted in Figs. 4.14 to 4.19.

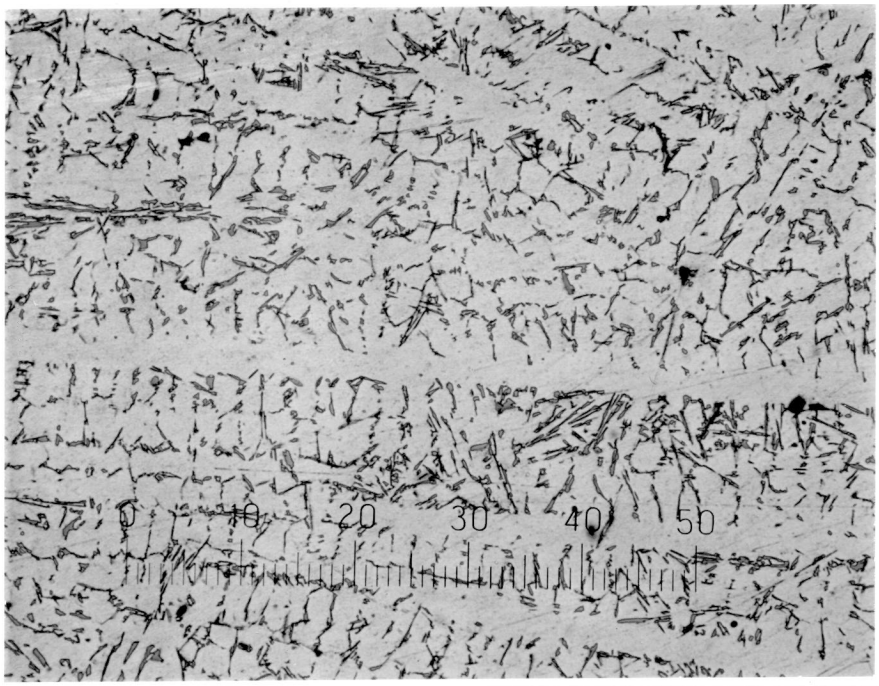

(a)

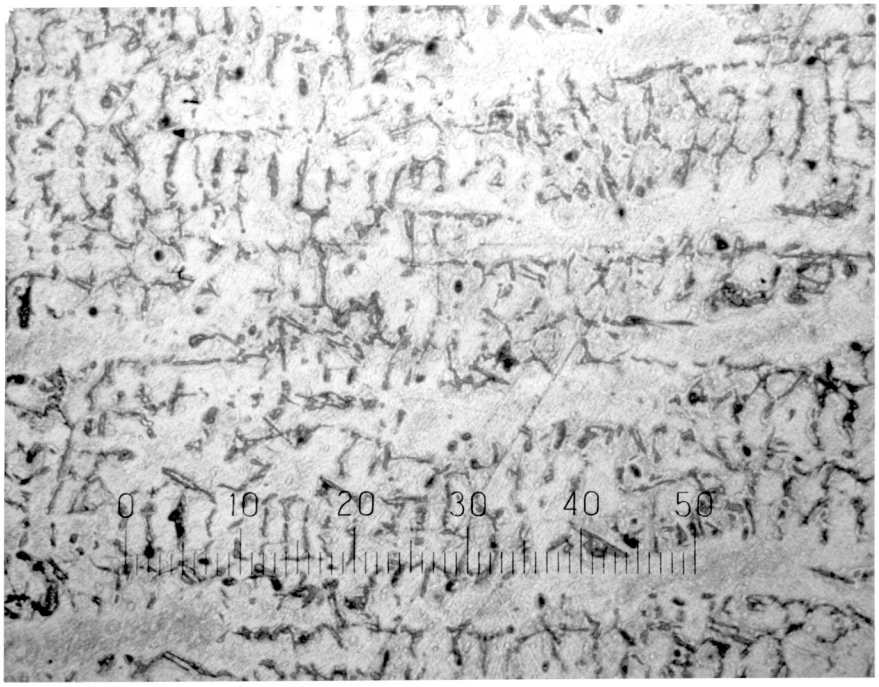

(b)

Fig. 4.12 Typical micrographs of the castings (etched in Kellers reagent, each scale reading represents 0.02mm) - (a) Al-7%Si alloy and copper chill, (b) Al-7%Si alloy and cast iron chill.

It is apparent that the SDAS increases with increasing distance from the interface. SDAS increases with increasing roughness of the chill surface (Fig. 4.14) and decreasing thermal diffusivity of the chill material (Fig. 4.15). Increasing the superheat decreases the SDAS at a given location in the casting as depicted in Fig. 4.16. SDAS at a given location increases with decreasing silicon content (Fig. 4.17). The effect of the oils on SDAS is depicted in Fig. 4.18. The four oils utilized in this study appear not to have considerable effect on the SDAS at distances near the surface (< 10 mm) but decreases the SDAS at distances further away from the interface. Changes in bath height have no tangible effect on the measured SDAS as shown in Fig. 4.19. The reason for each of the observed results are discussed later in Chapter 6.

Table 4.5 Typical secondary dendrite arm spacing measurements for copper chill.

	Measured SDAS (μm)									
Shell (mm)	1	2	3	4	5	6	7	Mean	Std.**	% Error
		Surface Roughness = 0.018 μm								
4.0	20.00	16.70	18.75	21.40	16.00	20.00	19.00	18.84	0.18	20.0
8.0	41.7	38.90	33.30	35.00	33.30	37.50	35.00	36.39	0.29	17.8
12.0	42.90	41.60	42.90	43.30	45.00	45.00	43.30	43.43	0.11	10.0
16.0	41.80	46.00	54.00	50.00	50.00	51.00	53.30	49.44	0.40	20.0
20.0	61.00	65.00	62.50	63.00	62.50	63.30	62.50	62.83	0.11	8.2
		Surface Roughness = 0.0304 μm								
18.60	18.60	20.00	26.30	22.20	22.90	22.90	25.00	22.56	0.25	20.4
40.00	40.00	38.75	38.70	40.00	41.67	40.00	42.00	40.16	0.12	10.7
48.00	48.00	42.90	42.00	45.00	45.70	47.50	46.70	45.40	0.21	13.5
53.00	53.00	52.50	46.70	46.70	52.00	53.30	53.30	51.07	0.28	15.5
55.00	55.00	57.50	60.00	65.00	60.00	62.00	63.30	60.40	0.32	16.1
		Surface Roughness = 0.291 μm								
27.00	27.00	27.50	22.50	25.00	30.00	32.50	33.30	28.26	0.36	22.6
50.00	50.00	44.30	44.00	42.50	45.00	50.00	50.00	46.54	0.31	17.0
48.50	48.50	46.00	50.00	57.50	53.20	54.50	57.50	52.46	0.41	20.3
60.00	60.00	60.00	62.00	61.00	55.00	60.00	61.00	59.86	0.21	12.1
70.00	70.00	62.00	63.30	63.30	63.30	65.00	62.50	64.20	0.25	13.4

** Std stands for standard deviation

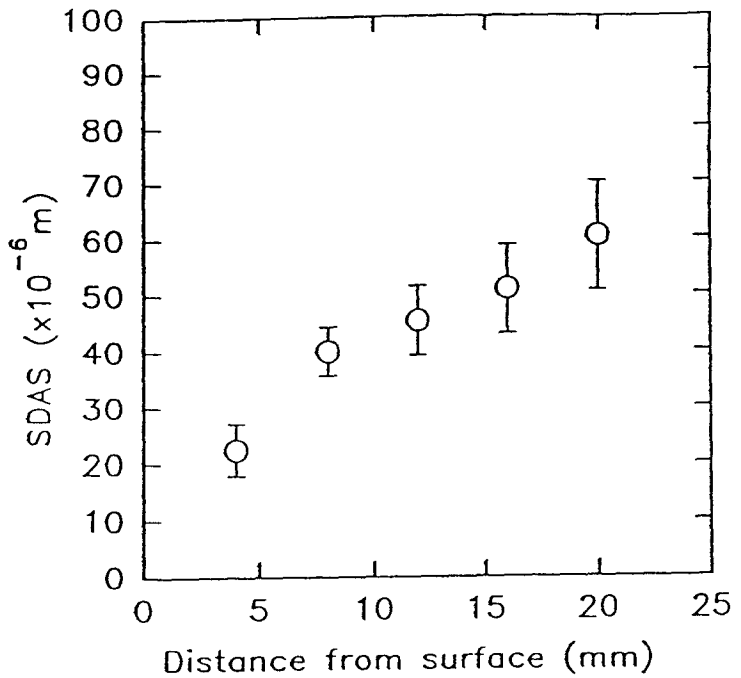

Fig. 4.13 **Typical measured secondary dendrite arm spacing with corresponding error bars for Al-7%Si alloy and copper chill.**

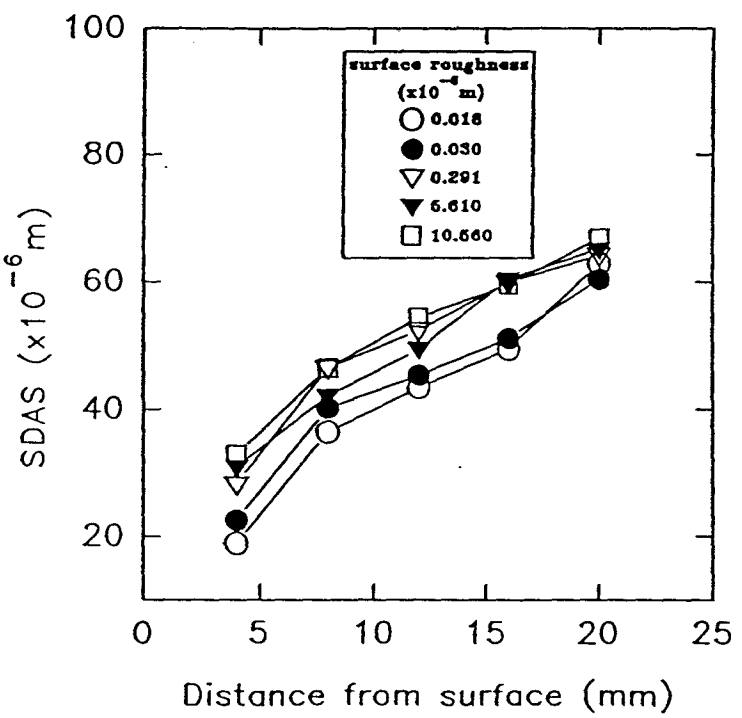

Fig. 4.14 **Effect of surface roughness on measured secondary dendrite arm spacing for Al-7%Si alloy and copper chill.**

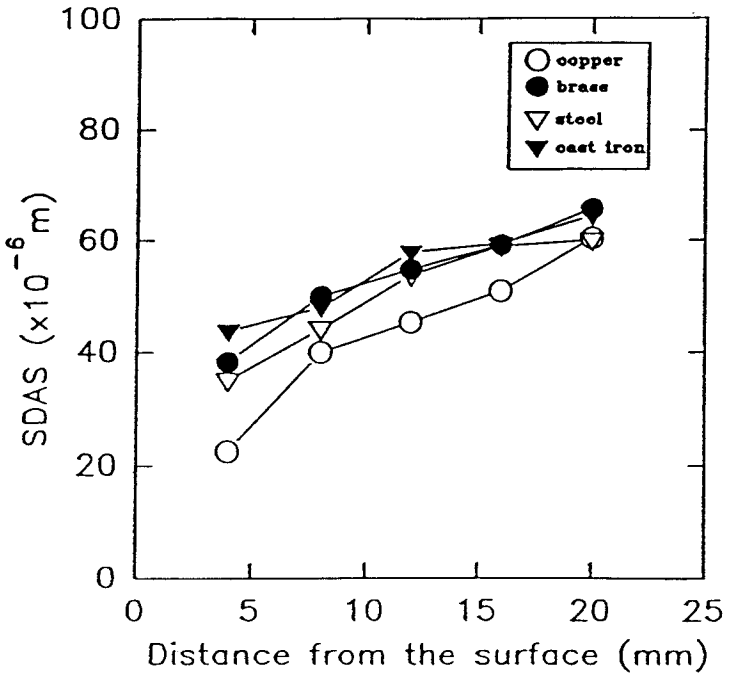

Fig. 4.15 **Effect of chill material on measured secondary dendrite arm spacing for Al-7%Si alloy.**

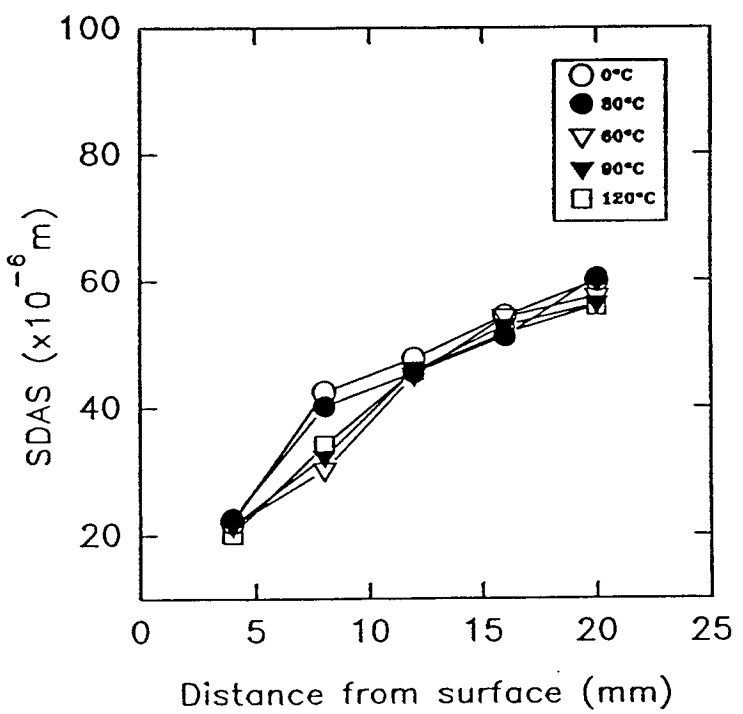

Fig. 4.16 **Effect of superheat measured secondary dendrite arm spacing for Al-7%Si alloy and copper chill.**

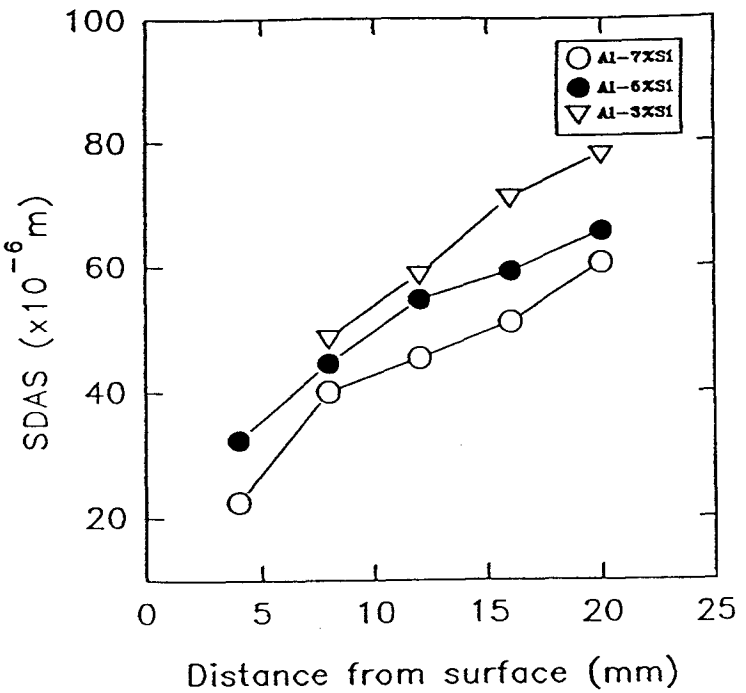

Fig. 4.17 **Effect of alloy composition on measured secondary dendrite arm spacing for copper chill.**

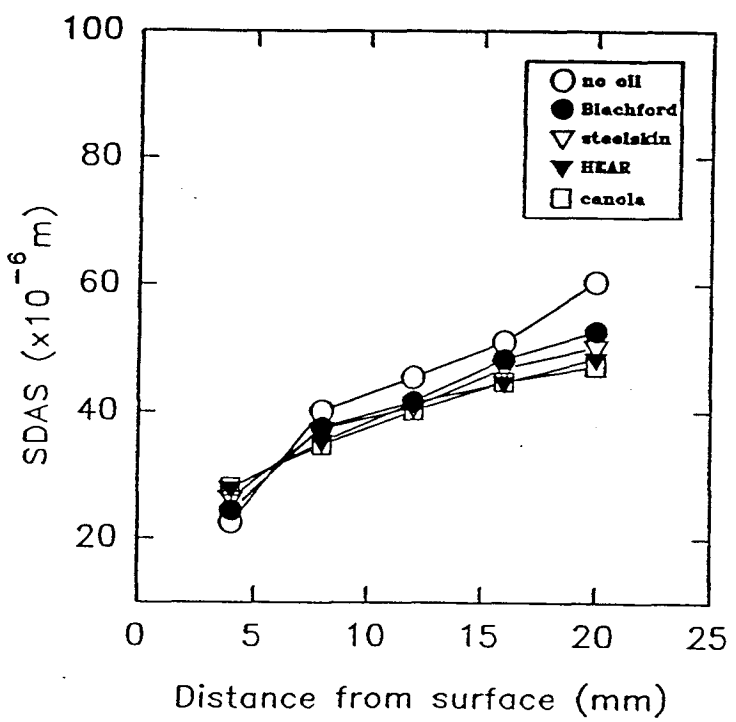

Fig. 4.18 **Effect of oil film on measured secondary dendrite arm spacing for Al-7%Si alloy and copper chill.**

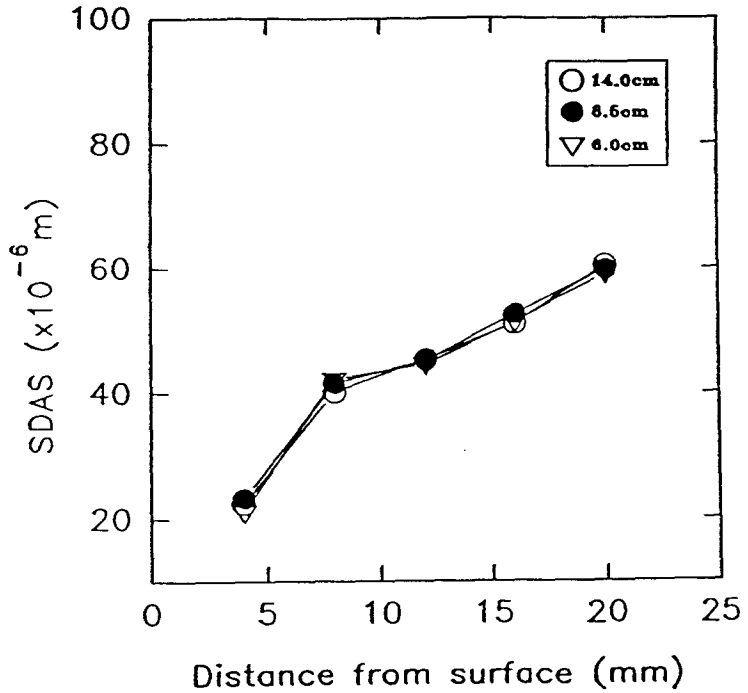

Fig. 4.19 Effect of bath height on measured secondary dendrite arm spacing for Al-7%Si alloy and copper chill.

Chapter 5

MATHEMATICAL MODELING

5.1 Chill Heat Flow Model

With adequate insulation on the cylindrical surface of the chill, heat flow through the chill could be reasonably approximated to a one-dimensional heat transfer problem. Thermal analysis of the chill involves the following steps:

(i) heat transfer from solidifying shell to the chill hot face. The mode of heat transfer here could be convection, radiation or conduction depending on the form of contact between the solidifying shell and the chill which determines the existence of an air gap between them.

(ii) heat transfer through the chill thickness by conduction.

(iii) heat transfer from the chill cold face to the cooling fluid mainly by convection.

The governing equation for the chill heat flow model is therefore

$$\frac{\partial}{\partial z}\left(k\frac{\partial T}{\partial z}\right)=\rho C_p\frac{\partial T}{\partial t} \tag{5.1}$$

<u>Initial and Boundary Conditions</u>

1. Initial temperature of the chill is specified ($l_{ch/c} < z < l_{ch}$, $0 < r < r_0$, t=0)

$$T = T_0 = \text{constant} \tag{5.2}$$

2. At the chill hot face ($z = l_{ch/c}$, $0 < r < r_0$, t)

$$-k\frac{\partial T}{\partial z}=q_c(t)=h_c(t)\,(T_{cs}-T) \tag{5.3}$$

3. At the chill cold face ($z = l_{ch}$, $0 < r < r_0$, t)

$$T = T_{ch}(t) \tag{5.4}$$

Equation (5.1) was solved numerically using implicit finite difference equations based on the Crank-Nicolson method which has a second-order accuracy in both space and time. To provide this accuracy, the finite difference approximations were developed at the midpoint of the time increment ($\Delta t/2$). The chill was discretized into N nodal points of width Δz as shown in Fig. 5.1, such that a typical interior node (i.e. $2 \le i \le N$) yields the following expression for a time step Δt:

$$\frac{\alpha\Delta t}{2\Delta z^2}T_{i-1}^{n+1} - \left\{1 + \frac{\alpha\Delta t}{\Delta z^2}\right\}T_i^{n+1} + \frac{\alpha\Delta t}{2\Delta z^2}T_{i+1}^{n+1} = \frac{\alpha\Delta t}{2\Delta z^2}T_{i-1}^{n} - \left\{\frac{\alpha\Delta t}{\Delta z^2} - 1\right\}T_i^{n} + \frac{\alpha\Delta t}{2\Delta z^2}T_{i+1}^{n} \tag{5.5}$$

At the chill hot face, Eq. (5.3) becomes

$$-\left\{1 + \frac{\alpha\Delta t}{\Delta z^2}\right\}T_1^{n+1} + \frac{\alpha\Delta t}{\Delta z^2}T_2^{n+1} = \frac{2\Delta t}{\rho C_p \Delta z}q_c^{n+1} - \left\{\frac{\alpha\Delta t}{\Delta z^2} - 1\right\}T_1^{n} + \frac{\alpha\Delta t}{\Delta z^2}T_2^{n} \tag{5.6}$$

At the chill cold face, Eq. (5.4) remains unchanged. The unknown heat flux, q_c^{n+1}, is best associated with the midpoint of the time step from the present time, t^n, to the future time, t^{n+1}. The temperatures are all known at time t^n and are needed at time t^{n+1}.

Equations (5.5) and (5.6) were solved using the non-linear inverse heat conduction technique based on Beck's method[133,134]. This technique employs the least square minimization with regularization approach to obtain values of $q_c(t)$ and nodal temperatures in the chill (See APPENDIX A). The measured temperature at 22.2mm from the hot face was used as a boundary condition while the thermocouple readings at 1.6mm and 3.2mm were used as interior temperature profiles respectively. The model output at each time step includes the following: the interfacial heat flux, temperature distribution in the chill, the difference between calculated

and measured temperatures at the thermocouple locations, and the root mean square of these differences. The thermophysical properties employed in this model are summarized in Table 5.1.

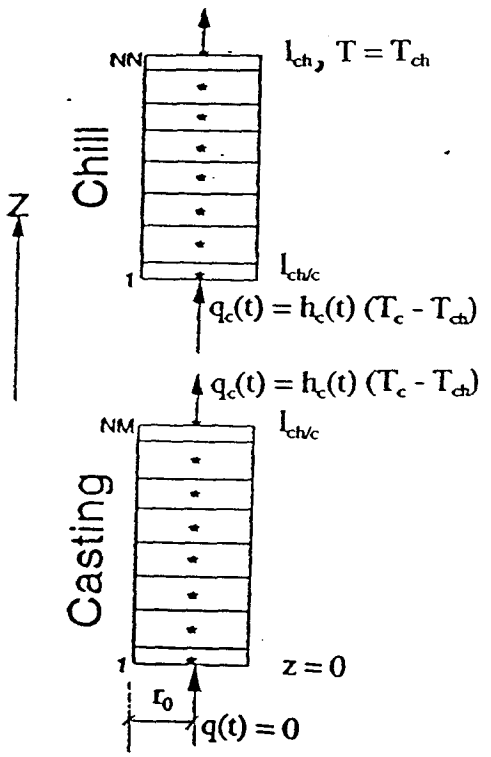

Fig. 5.1 Discretization of both chill and casting.

Table 5.1. Thermophysical properties of materials used in the chill model[45,75,128,135-137].

Chill	Copper	Brass	Carbon Steel	Cast Iron
Density (ρ, Kgm^{-3})	8940	8522	7400	7100
Specific Heat ($C_p, JKg^{-1}K^{-1}$)	384 + 0.0988T	385	456 + 0.376T	514 + 0.38T
Thermal Conductivity ($k, Wm^{-1}K^{-1}$)	400 - 0.0614T	104.93 + 0.3 T - 6.2 x 10^{-4} T^2 + 3.6 x 10^{-6} T^3	59.4 - 0.0418T	43.9 - 0.0131T
Thermal Diffusivity (α, m^2s^{-1})	1.16 x 10^{-4} - 4.42 x 10^{-8} T	3.20 x 10^{-5} + 9.14 x 10^{-8} T - 1.89 x 10^{-10} T^2	1.73 x 10^{-5} - 2.10 x 10^{-8} T	1.19 x 10^{-5} - 1.00 x 10^{-8} T
Average Coefficient of Linear Thermal Expansion ($L_m, \mu m/m.K$)	16.9	19.9	14.5	13.0
Emmisivity of oxidized surface (ε)	0.57	0.63	0.31	0.61

5.2 Casting Heat Flow Model

Although the furnace was turned off before the chill was dipped into the metal, it was found from both measurements and calculations that with adequate insulation around the crucible (> 5mm insulation thickness), the heat flux through the crucible constitutes less than 2% of total heat loss by the casting. Hence, the heat transfer in the casting can also be treated as 1-D case. Heat is extracted from the casting in the following steps:

(i) heat transfer in the liquid pool (convection and conduction)

(ii) heat transfer through the mushy zone (convection and conduction)

(iii) heat transfer through the solidified shell thickness (mainly conduction)

(iv) heat transfer from the casting surface to the chill hot face. Here, the mode of transfer could be conduction, convection or radiation depending on the form of contact between shell and chill.

(v) heat transfer from the casting to the crucible wall (could be convection, conduction or radiation)

(vi) heat transfer from the exposed surface of the casting to the atmosphere (mainly convection and radiation)

As in the chill model, the governing equation for this model is similar to Eq. (5.1) except that a heat source term exists in this case.

$$\frac{\partial}{\partial z}\left(k\frac{\partial T}{\partial z}\right)+L\frac{\partial f_s}{\partial t}=\rho C_p\frac{\partial T}{\partial t} \tag{5.7}$$

<u>Initial and Boundary Conditions</u>

1. Initial temperature of the casting is specified ($0 < z < l_{ch/c}$, $0 < r < r_0$, t)

$$T = T_p = \text{constant} \tag{5.8}$$

2. At the chill/casting interface ($z = l_{ch/c}$, $0 < r < r_0$, t)

$$k\frac{\partial T}{\partial z}=q_c(t)=h_c(t)\,(T-T_{chs}) \tag{5.9}$$

3. At the casting/crucible interface ($z = 0$, $0 < r < r_0$, t)

$$k\frac{\partial T}{\partial z}=q_{cr}(t)\approx 0 \tag{5.10}$$

The discretization procedure is similar to that of the chill model. The values of $q_c(t)$ obtained from the chill model solution were used as input data in the implicit finite difference

casting model to yield values of the nodal temperatures which were then utilized to compute such parameters as shell thickness, heat transfer coefficient, the thermal resistances, solidification times, local solidification times and cooling rate. These parameters were used in the DAS models. The thermophysical properties utilized in the casting and DAS models are summarized in Table 5.2. A schematic illustration of the complete computer implementation of the models is depicted in Fig. 5.2.

Assumptions :

(1) The latent heat evolution during solidification was accounted for by varying the specific heat capacity, C_p.

(2) There are no other sources of heat generation (i.e apart from the latent heat of solidification).

(3) There is no net heat consumption across the chill/casting interface. Hence, the heat flux profile calculated for the chill above was the same as the heat flux extracted from the casting.

(4) The specific heat capacity, thermal conductivity and density are all functions of temperature.

(5) Heat transfer in the liquid by convection is very negligible and is not accounted for in the model.

Table 5.2. Thermophysical properties of materials used in the casting model[45,75,128,135-137].

Casting	Al-7%Si	Al-5%Si	Al-3%Si
Density (ρ, Kgm^{-3})	2680	2690	2695
Liquidus Temperature ($T_l, °C$)	610	632	648
Solidus Temperature ($T_l, °C$)	577	577	577
Latent Heat (L, JKg^{-1})	389000	389000	389000
Specific Heat ($C_p, JKg^{-1}K^{-1}$)	963	963	963
Average Thermal Conductivity ($k, Wm^{-1}K^{-1}$)	90	104	121
Thermal Diffusivity (α, m^2s^{-1})	3.49×10^{-5}	4.01×10^{-5}	4.66×10^{-5}
Volume Shrinkage (%)	3.5	4.8	6.0
Average Coefficient of Linear Thermal Expansion ($L_c, \mu m/m.K$)	23.5	24.0	24.7
Emmisivity of oxidized surface (ε)	0.19	0.19	0.19

Other Parameters	
c_0 (%)	7
c_e (%)	12.3
k_p	0.13
D_l (m^2s^{-1})	3.10×10^{-9}
m ($Kpct^{-1}$)	-6
Γ (mK)	0.9×10^{-7}

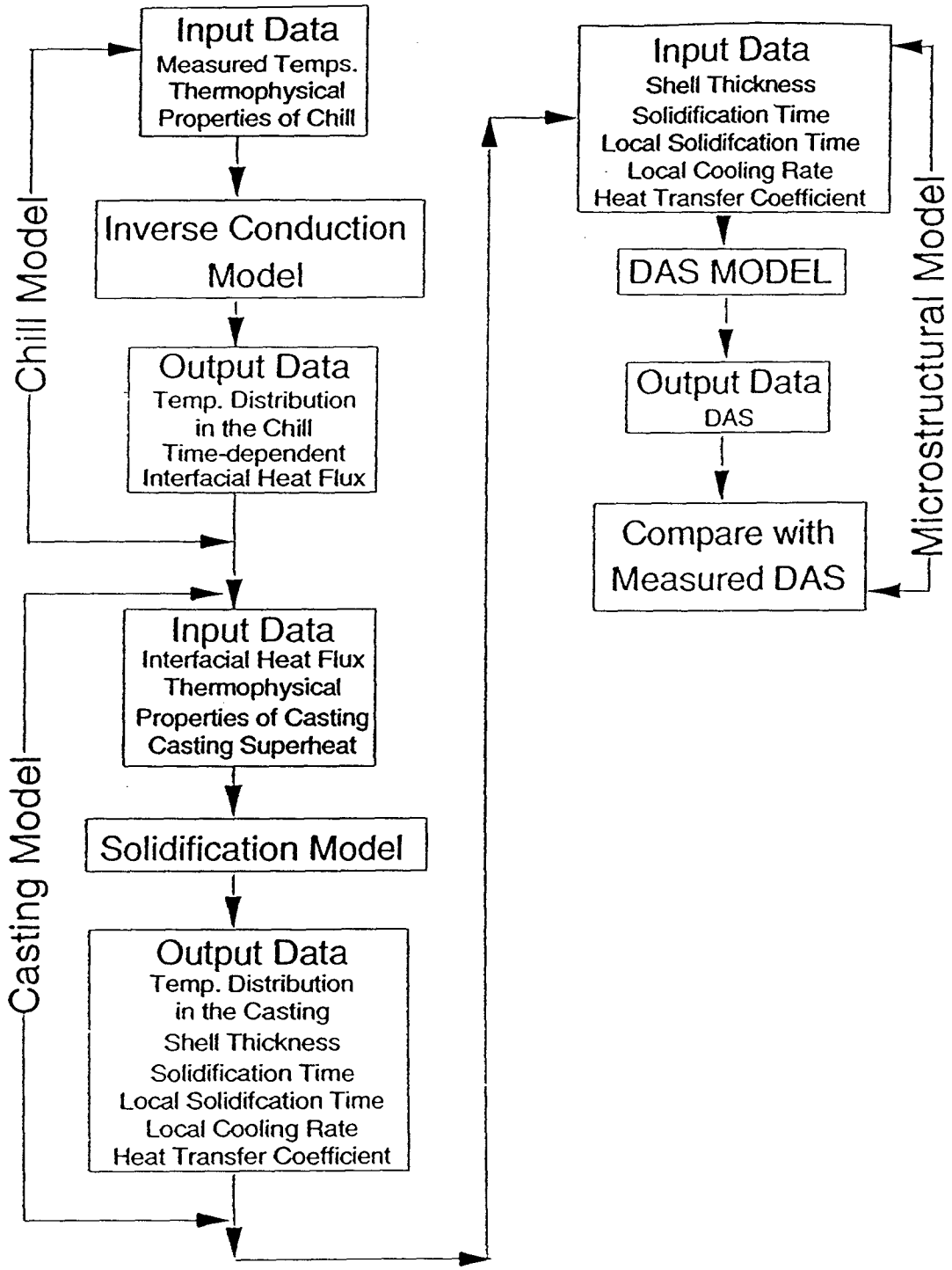

Fig. 5.2 Schematic illustration of the complete computer implementation.

5.2.1 Latent Heat Evolution and Fraction Solid

The effective heat capacity technique discussed in section 2.3.2 was adopted to handle the latent heat evolution. A linear temperature distribution between nodes was assumed and the latent heat release at any node within the vicinity of the mushy zone (illustrated in Fig. 5.3) is evaluated as follows:

$$T_{\uparrow} = \frac{T_I + T_{I+1}}{2} \tag{5.11}$$

$$T_{\downarrow} = \frac{T_I + T_{I-1}}{2} \tag{5.12}$$

Case I. Liquidus Vicinity: Node is above the liquidus while a fraction of its volume lies within the mushy zone ($T_I > T_L$, $T_{\downarrow} < T_L$) or node is within the mushy zone while a fraction of its volume is above the liquidus ($T_S < T_I < T_L$, $T_{\uparrow} > T_L$).

$$C_{eff} = Vfl.C_p(T) + (1 - Vfl).\left(C_p(T) - L\frac{\Delta f_s}{\Delta T} \right) \tag{5.13}$$

where $\quad Vfl = \dfrac{T_L - T_{\downarrow}}{T_{\uparrow} - T_{\downarrow}}$

In this case, $\Delta f_s/\Delta T$ is evaluated at the temperature $T = 0.5(T_L + T_{\downarrow})$

Case II. Complete Mushy: The whole nodal volume lies completely within the mushy zone ($T_{\uparrow} > T_S$, $T_{\downarrow} < T_L$).

$$C_{eff} = C_p(T) - L\frac{\Delta f_s}{\Delta T} \tag{5.14}$$

$\Delta f_s/\Delta T$ is evaluated at the nodal temperature, T_I.

Case III. Solidus Vicinity: Node is above the solidus while a fraction of its volume lies below the solidus ($T_S < T_I > T_L$, $T_{\downarrow} < T_S$) or node is below the solidus while a fraction of its volume is above the solidus ($T_I < T_S$, $T_{\uparrow} > T_S$).

$$C_{eff} = Vf2.C_p(T) + (1 - Vf2).\left(C_p(T) - L\frac{\Delta f_s}{\Delta T} \right) \tag{5.15}$$

where $Vf2 = \dfrac{T_{\uparrow} - T_S}{T_{\uparrow} - T_{\downarrow}}$

In this case, $\Delta f_s/\Delta T$ is evaluated at the temperature $T = 0.5(T_{\uparrow} + T_S)$

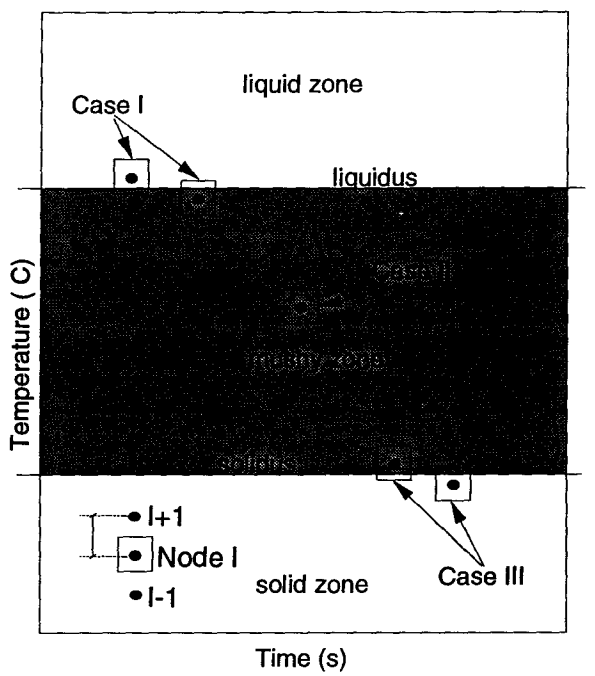

Fig. 5.3 Schematic illustration of the various zones in the effective specific heat method - Case I. liquidus vicinity, Case II. complete mushy and Case III. solidus vicinity.

The solid fraction was initially calculated using the Clyne and Kurz model[125]:

$$f_s = \frac{1}{1-2Fo'k_p}\left[1-\left(\frac{T-T_s}{T_L-T_S}\right)^{\left(\frac{1-2Fo'k_p}{1-k_p}\right)}\right] \tag{5.16}$$

where $Fo' = Fo[1-\exp(-Fo^{-1})] - 0.5\exp(-0.5Fo^{-1})$

and the Fourier Number, $Fo = \frac{D_s t_f}{\Delta z^2}$

Equation (5.17) reduces to the lever rule as Fo approaches infinity and to Scheil model as Fo approaches zero[5]. A value of 3 x 10^{-9} m^2/s has been reported[75] for the liquid diffusion coefficient of Si in liquid Al-Si alloys. Assuming that the solid diffusion coefficient is about one fifth of this value, the Fourier number was found to be so small that the result of Eq. (5.17) was not different from that of Scheil model. Hence, the simpler Sheil model was subsequently used to calculate the solid fraction such that

$$f_s = 1-\left(\frac{T-T_S}{T_L-T_S}\right)^{1/(1-k_p)} \tag{5.17}$$

5.3 Dendrite Arm Spacing (DAS) Models

The secondary dendrite arm spacings were computed using equations (2.37), (2.38), (2.40) and (2.42). The constant C_5 was evaluated using the rate coarsening model due to Mortensen[118].

$$\lambda_2 = C_5\left\{\frac{27\Gamma D_l}{4c_l(-m)(1-k_p)f_s(1-\sqrt{f_s})}t_f\right\}^{1/3} \tag{5.18}$$

The constant C_4 was evaluated by fitting the calculated cooling rate to the measured secondary dendrite arm spacing. The values for the parameters used in these equations were also included in Table 5.1.

5.4 Sensitivity Analysis And Model Validation

Sensitivity analysis was carried out for both the chill and the casting models. For the chill IHCP model, the effect of node size, time step and number of future time steps (a period of time where the heat flux is assumed to be temporarily constant) were studied. The Crank-Nicolson implicit finite difference procedure which was used in this case has an accuracy that varies as $(\Delta z)^2$ and $(\Delta t)^2$ respectively for constant thermophysical properties. By testing the IHCP model for different time steps it was established that the heat flux does not vary appreciably at time steps $\Delta t \leq 0.5s$. A calculational time step of 0.25s was chosen in accordance with the suggestion[112] that the calculational time step be one half or one third of the experimental time (data was recorded at 0.5s interval). A node size of 6×10^{-4}m was also found to be adequate.

The selection of the number of future time steps (see Appendix A) to be used in the program is more complicated. Increasing the number of future time steps has the beneficial effect of reducing the sensitivity of the IHCP algorithm to measurement errors by "smoothing or biasing" the measurements to ensure a more stable output. However, there are two deleterious effects of increasing the number of future time steps. First, there is less agreement between the measured and calculated temperatures at a particular time step. Secondly, sudden changes in heat flux could be missed by biasing. Therefore, a balance must be achieved between two opposing conditions of minimum sensitivity of heat flux to measurement errors and minimum error in heat flux for errorless data. As measurement error increases, the number of future time steps value should increase and vice versa. A value of 2 was found to be adequate for smooth thermocouple readings while a value of 4 was better for readings with appreciable fluctuation. The model is validated by comparing the predicted values at the thermocouple locations with the measured values as shown in Fig. 5.4. A good agreement exists between the measured and model predicted temperatures.

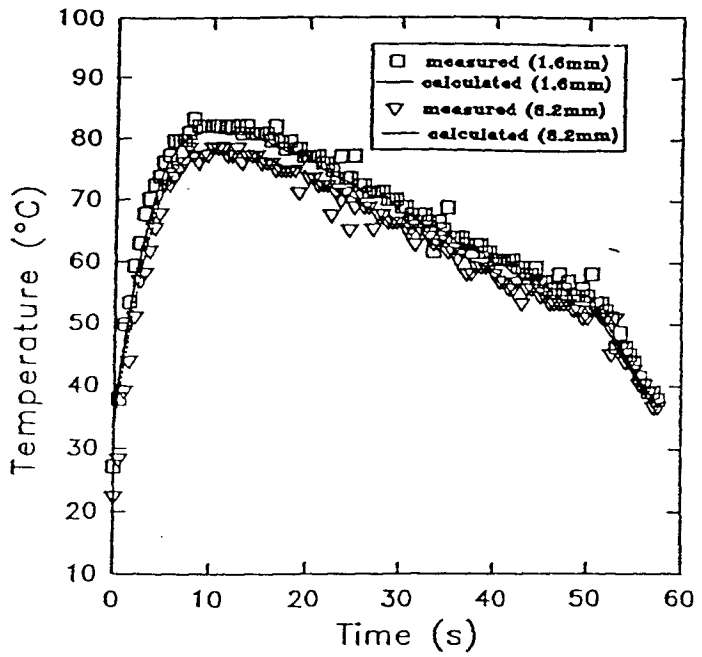

Fig. 5.4 Typical calculated and measured temperature profiles in the chill.

For the casting model, the choice of Δz and Δt was made by comparing the numerical result with an infinite slab analytical predictions for the same boundary conditions. An example of this comparison is shown in Fig. 5.5. Good agreement is seen to exist between the analytical and numerical results. Based on this comparison, a node size of 7×10^{-4}m was chosen while a time step of 0.5s was adopted. Furthermore, the energy balance at each time step was cross-checked by recalculating the surface heat flux from the predicted temperatures and comparing the calculated values with the input values. Table 5.3 depict a typical result of this procedure. Good agreement is also observed between the two values. The model was also validated by comparing the predicted temperature profile at a given location with thermocouple output within the casting as shown in Fig. 5.6 and the predicted results compares well with the

measured ones. Further validation was carried out by comparing the model predicted shell thickness with the measured values. A typical result of this comparison is shown in Fig. 5.7. The predicted shell thickness compares favorably with the measured values.

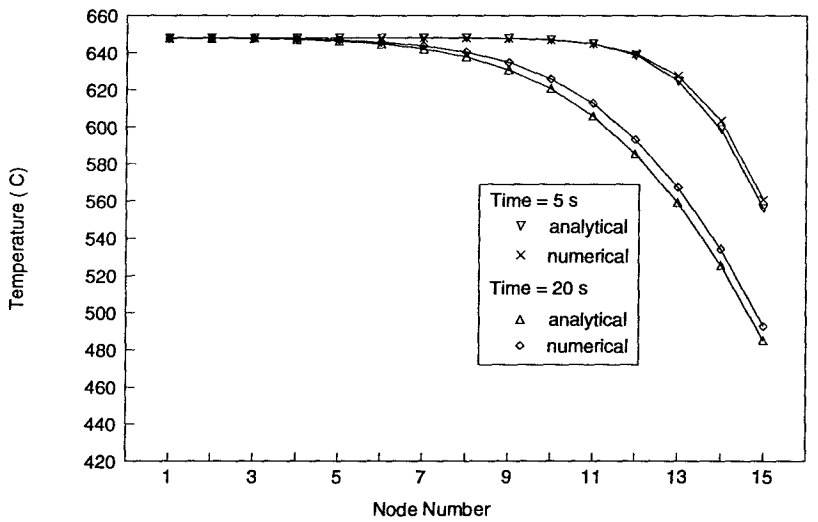

Fig. 5.5 Temperature profile at the same location for both analytical and numerical solutions of the transient infinite slab problem.

Table 5.3. Comparison between the input heat flux and recalculated heat flux.

Time (s)	Surface Temp. (°C)	q input (MW/m^2)	q recal. (MW/m^2)	Standard Deviation
2	635	1.14	1.14	0.03
4	627	1.05	1.05	0.01
6	622	1.00	1.00	0.00
8	618	0.97	0.97	0.01
10	615	0.95	0.95	0.15
12	613	0.95	0.95	0.15
14	610	0.93	0.93	0.17
16	609	0.93	0.93	0.42
18	607	0.91	0.91	0.35
20	605	0.87	0.87	0.42
22	602	0.85	0.85	0.41
24	598	0.81	0.81	0.39
26	594	0.77	0.77	0.33
28	589	0.71	0.71	0.33
30	584	0.66	0.66	0.10

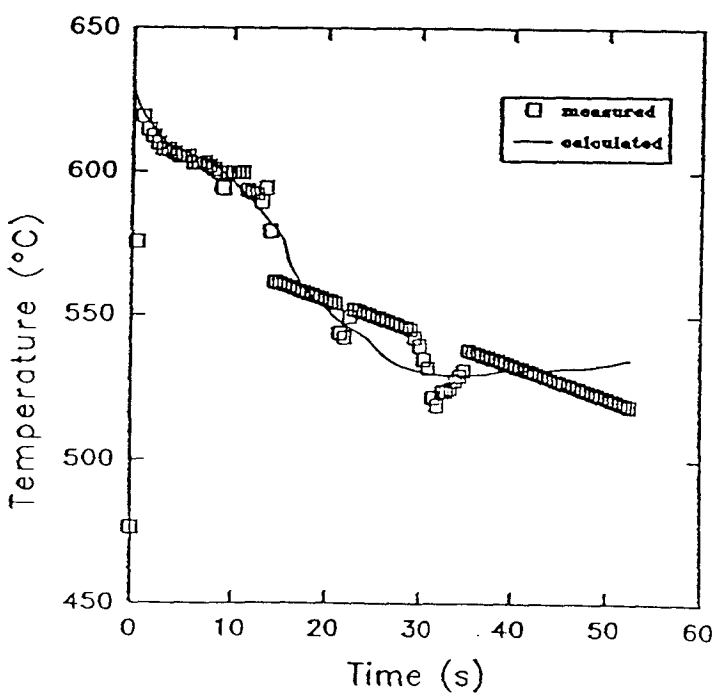

Fig. 5.6 Typical calculated and measured temperature profiles in the casting (10mm depth).

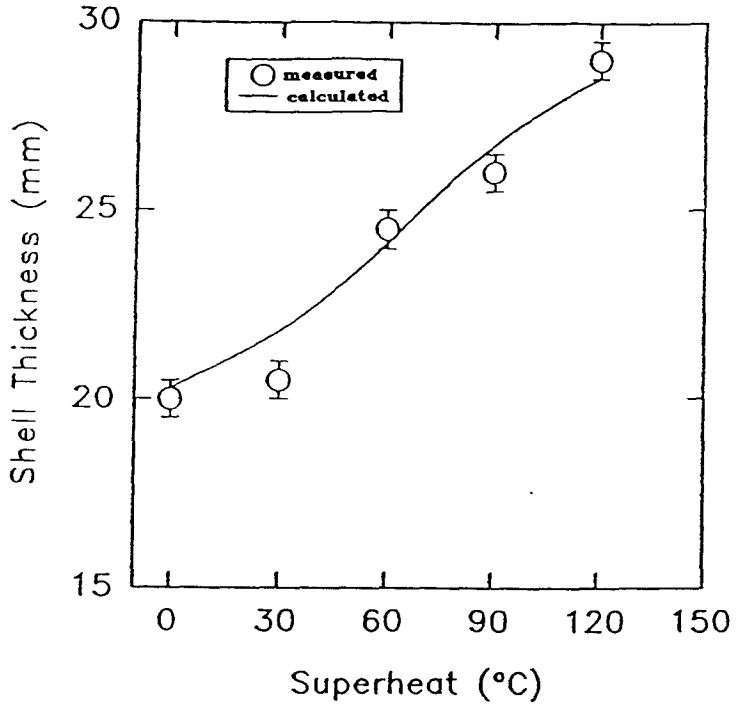

Fig. 5.7 Measured and calculated shell thickness profiles at various superheats.

Chapter 6

RESULTS AND DISCUSSION

6.1 Heat Flow

As indicated in the measured temperature-time profiles (Figs. 4.5-4.11), it is evident that the temperature at any location in the chill increases very rapidly once contact is established with the liquid metal until a peak value is attained. The magnitude and time of attaining this peak value at a given location depend on the casting conditions. As expected, the magnitude of the temperature peak increases while the time of attaining the peak decreases with decreasing distance from the interface due to the chill thermal resistance. From this peak value the temperature drops initially with a steep gradient and finally to a fairly steady value. This result is similar to that observed by Pehlke et al.[47] for the case when the chill is located above the casting.

Typical model predictions for the interfacial heat flux, heat transfer coefficient, shell thickness, interfacial gap and surface temperature profiles are depicted in Figs. 6.1, 6.2 and 6.3 respectively. These profiles correspond to a copper chill dipped into Al-7%Si alloy at a superheat of 30°C and with a chill surface roughness value of 0.03 μm and represent the general trend in the results. It is obvious that the interfacial heat flux and heat transfer coefficient follow the same trend as the measured chill temperatures. The radiation components of the heat flux and heat transfer coefficient which were calculated based on parallel plate assumption are seen to be negligible, contributing less than one percent in each case. Initially, the casting/chill contact is localized according to the asperity profiles in the chill and the wettability of the chill surface by the molten metal, but increases continuously as the liquid metal spreads on the chill surface.

The peak heat flux (q_{max}) occurs at the time when a nearly perfect and continuous contact is established between casting and chill. Thus, the peak heat flux corresponds to the onset of a steadily growing shell.

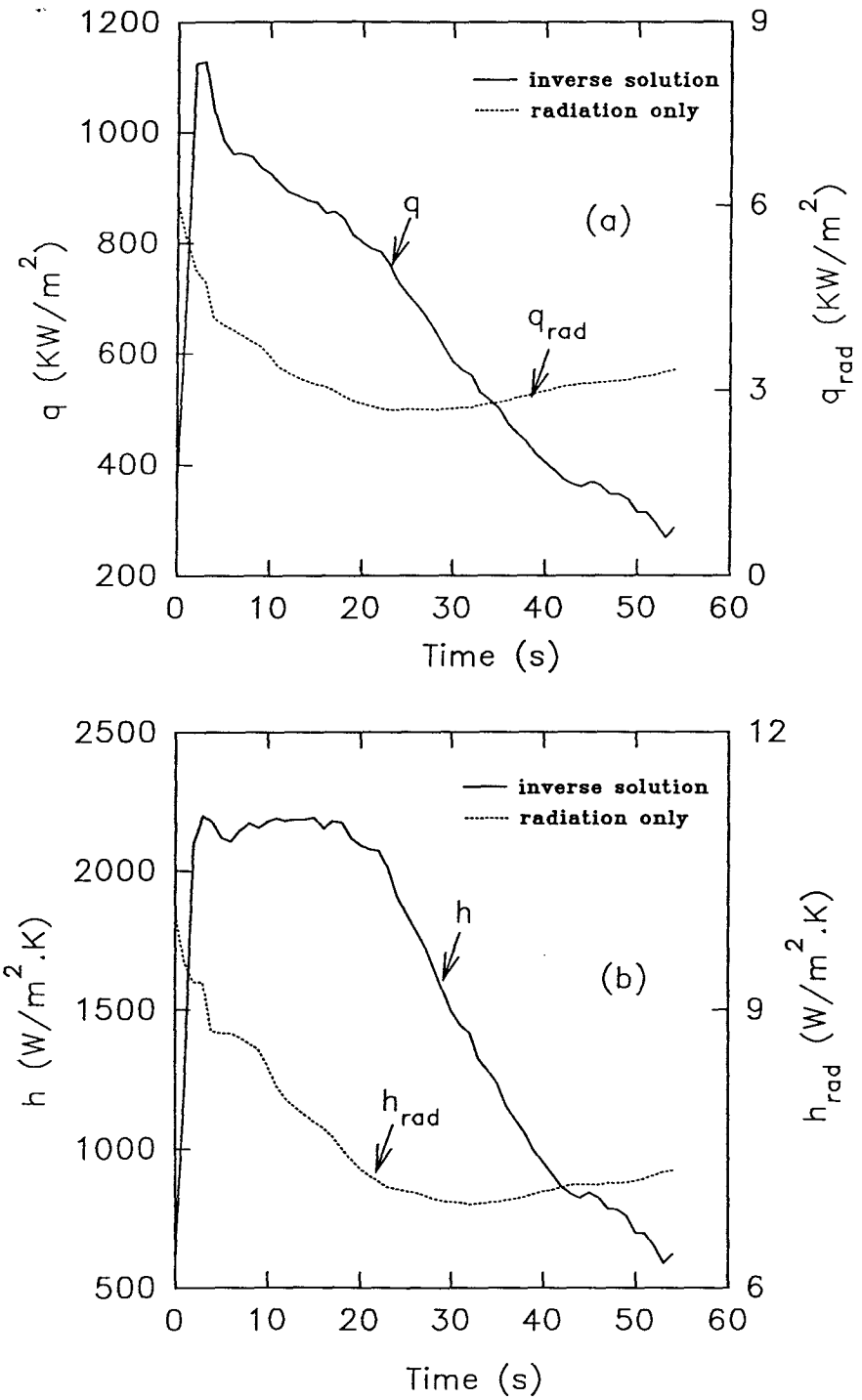

Fig. 6.1 Typical model predictions for Al-7% Si alloy and copper chill - (a) interfacial heat flux, (b) heat transfer coefficient.

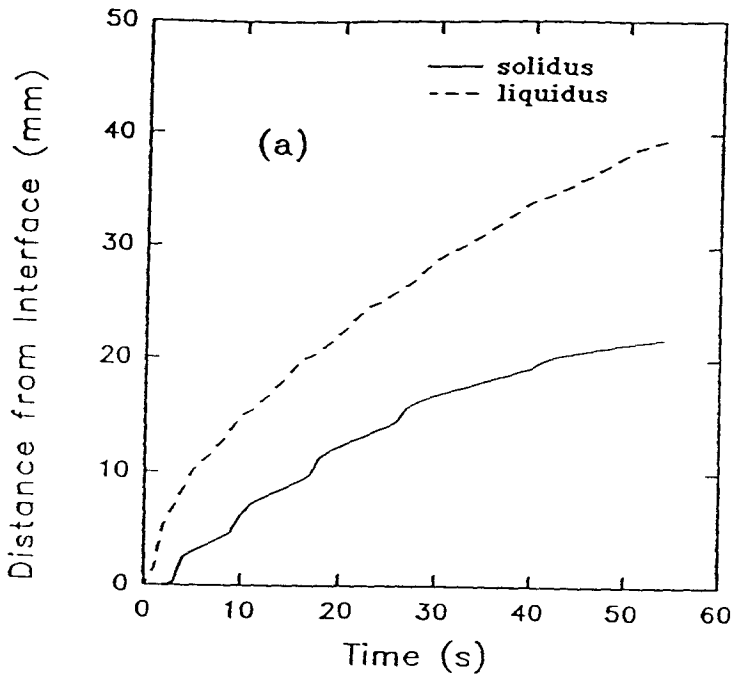

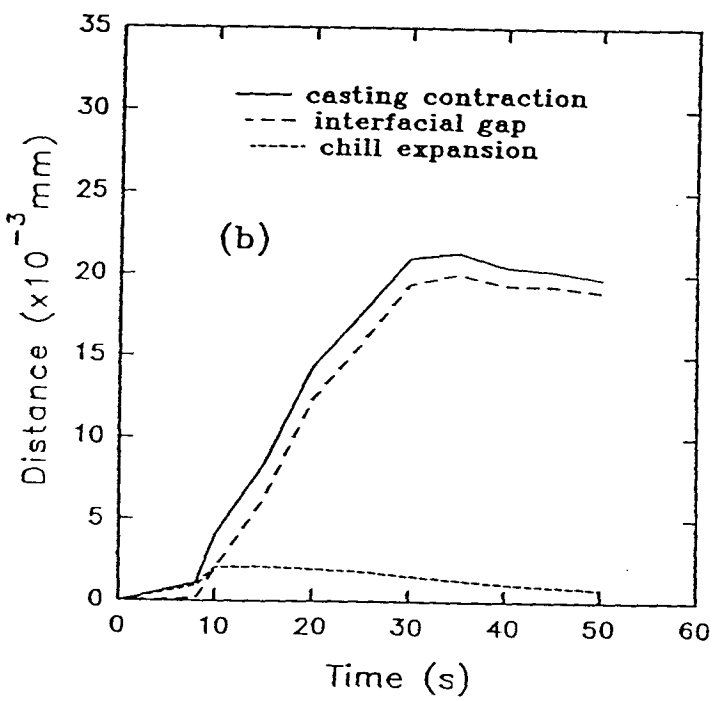

Fig. 6.2 Typical model predictions for Al-7% Si alloy and copper chill - (a) shell thickness (b) interfacial gap.

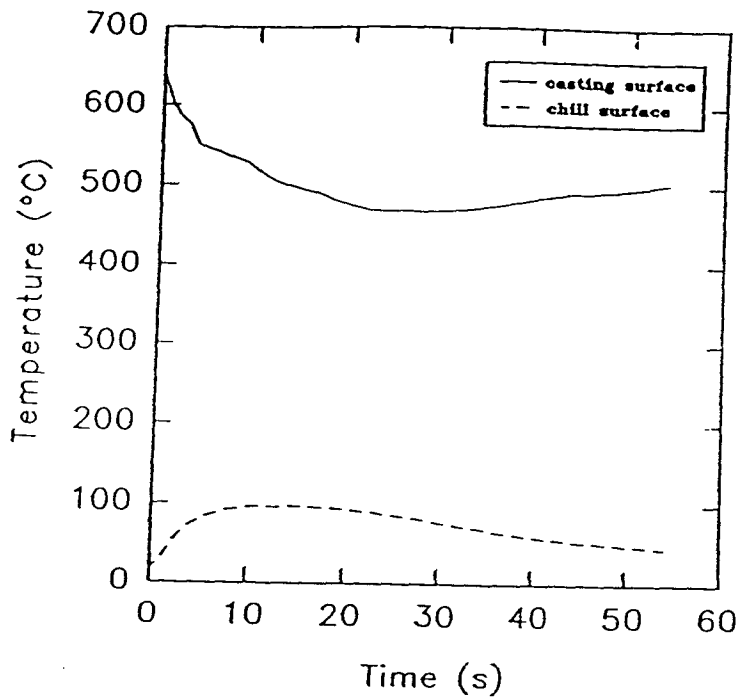

Fig. 6.3 Calculated surface temperature profiles in both chill and casting for Al-7% Si alloy and copper chill.

Within this period, the dominant factors controlling interface heat transfer[39,47,49,50,138] are:

(1) Wettability of Chill Surface: The interfacial heat transfer increases with increasing wettability of the chill surface. This is because wettability is a controlling factor that determines the extent of initial contact between casting and chill.

(2) Chill Surface Geometry: Interfacial heat transfer increases with increasing surface smoothness. The total area in actual contact increases with increasing smoothness of the chill surface.

(3) Chill Thermal Properties: Interfacial heat transfer increases with increasing thermal diffusivity of the chill particularly at the surface.

(4) Initial Chill and Casting Temperatures: The interfacial heat transfer increases with increasing temperature gradient across the interface. It is noted that this gradient provides the driving force for heat flow across the interface. Therefore, interfacial heat transfer increases with increasing casting temperature and decreasing chill temperature[50].

Once the solidifying shell becomes self-supporting, it contracts in accordance with the shrinkage properties of the casting while the chill surface may expand. The relative magnitude of the casting shrinkage and the chill expansion, together with any other pressure acting at the interface determines the type of contact between chill and casting. In most cases, an air gap is formed unless the contact pressure is increased. The extra thermal resistance introduced by the air gap accounts for the decrease in interfacial heat flux. Hence, the drop in heat flux from the peak value corresponds to the onset of a steadily growing air gap. At this point also, both the chill and casting surface may begin to oxidize. This mechanism has been confirmed by Pehlke et al.[47] who used transducers to monitor the electrical continuity between chill and casting. They found that the electrical circuit breaks down at the onset of a sudden drop in interfacial heat transfer. A further drop in interfacial heat flux occurs as the gap grows coupled with increasing thermal resistance of the solidified shell.

From the onset of a steadily growing gap, the following factors become dominant in interfacial heat flow:

(1) shrinkage characteristics of the casting

(2) thermal conductivity and expansion characteristics of the chill

(3) thermal conductivity of the air gap

(4) surface oxidation characteristics of the chill and casting.

(5) thermal properties of surface oxide layers.

(6) temperature gradient across the chill/casting interface

(7) thermal conductivity of the solidifying shell.

It is observed from Fig. 4.3 that the interfacial thermal resistance is the dominant resistance throughout the duration of the experiment. The total thermal resistance decreases sharply from contact as a result of increasing interfacial heat transfer coefficient but starts to rise as the interfacial heat transfer coefficient decreases and shell thickness increases.

6.2 Microstructure Formation

The solidification structure in this work is predominantly columnar dendritic as shown in the microstructures of Fig. 4.11. The dendrite arm spacings were sufficiently distinct for fairly accurate measurements except at distances very near the chill surface where a thin chill zone (<1mm) exists. It is difficult to resolve dendrite arms in the chill zone. The measured dendrite arm spacing ranges from 18μm (at 4mm from the interface) to 80μm (at 20mm from the interface) as shown in Figs. 4.13 to 4.19 and, in all cases, increases with increasing distance from the chill surface. This implies that the secondary dendrite arm spacing (SDAS) increases with decreasing cooling rate since the cooling rate decreases with distance from the chill surface. Therefore, as expected, a higher heat extraction rate leads to a finer microstructure. The predominance of columnar dendritic growth observed in these experiments is an indication of solute diffusion effects during solidification[5,8]. Hence, the incorporation of a solute diffusion model into the solidification model is necessary.

In general, microstructure formation starts at the onset of heterogeneous nucleation at the mold wall asperities. The initial stage is probably pre-dendritic and has been found to consist of solid discs of the same composition as the liquid[139]. The dendritic substructure is established when crystallographic alignment is attained. Although dendritic growth proceeds in three stages

(propagation of primary stems, evolution of side branches or arms, and coarsening and coalescence), the final dendritic structure is controlled mainly by the coarsening and coalescence phenomena.

Table 6.1 compares the various SDAS model predictions with the measured values while Fig. 6.4 depicts this comparison for the particular case of Al-7%Si and copper chill. This table represents the range of SDAS values obtained in this study. It is evident that only three of these models are in consistently good agreement with the measured values - the theoretical model due to Mortensen[118], the empirical cooling rate model and another empirical model due to Bamberger et al.[50] . The constant in the cooling rate was found to be 58.0, compared with a value of 53.0 reported for aluminum copper alloys[123]. The fraction solid just before complete solidification ($f_s < 1.0$) was used to evaluate the coarsening rate parameter in the Mortensen model.

The Hills model[123] underpredicts the SDAS values as the distance from the chill surface increases. It is noted that the Hills model was developed with near-net-shape casting in mind. This implies solidification of relatively smaller casting dimensions which allows for a large influence of interfacial heat transfer coefficient on the SDAS. Based on these results, the Hills model was found to be consistently valid for distances less than 8mm from the chill interface and could therefore be useful for near-net-shape castings. The model due to Shiau et al.[122] was not reasonably consistent in its predictions. This is attributed to the assumption adopted in the development of this model, namely, that both the liquidus and solidus curves obey the square root law. It was observed that this was not the case in most of the results from this work. It has been shown that for most cases where thermal contact resistance exists between casting and mold, the square root law should be modified[33,140-142].

Table 6.1 Measured and typical model predicted values of SDAS.

Distance (mm)	Secondary Dendrite Arm Spacing, SDAS (μm)					
	Measured	Calculated				
		Ref. 107 $\lambda_2 = C(\partial T/\partial t)^{1/3}$ C=58.0	Ref. 118 $\lambda_2 = Ct_f^{1/3}$ C from Eq.(5.18)	Ref. 50 $\lambda_2 = Ct_f^{1/3}$ C=15.0	Ref. 122 $\lambda_2 = CX^{2/3}$ Eq.(2.40)	Ref. 123 $\lambda_2 = f(h,t)$ Eq. (2.43)
Casting: Al-7%Si Chill: Copper	Superheat = 30°C			Surface Roughness = 0.018 μm		
4	18.84	25.5	19.02	26.33	36.79	18.45
8	36.39	43.11	39.45	41.4	41.44	31.38
12	43.43	44.99	41.19	43.67	47.82	38.59
16	49.44	46.73	47.25	45.93	51.78	40.55
20	62.83	51.62	55.13	52.11	56.67	47.62
Casting: Al-7%Si Chill: Copper	Superheat = 30°C			Surface Roughness = 10.560 μm		
4	32.9	39.62	36.27	37.07	44.82	28.52
8	46.56	43.83	41.13	42.23	50.31	33.94
12	54.37	54.75	54.12	56.33	56.45	41.57
16	59.57	65.76	60.2	71.57	72.95	59.62
Casting: Al-7%Si Chill: Brass	Superheat = 30°C			Surface Roughness = 0.030 μm		
4	38.41	39.68	37.34	35.60	42.72	35.53
8	50.24	47.12	49.68	51.28	56.65	46.86
12	54.89	50.45	55.24	57.87	61.57	49.77
16	59.17	58.72	58.65	62.36	67.23	52.18
Casting: Al-3%Si Chill: Copper	Superheat = 30°C			Surface Roughness = 0.030 μm		
8	48.74	45.49	46.60	52.60	40.90	40.43
12	58.84	51.67	59.18	62.18	45.76	47.98
16	71.18	62.07	73.82	77.82	51.50	52.92

In general, the SDAS increases with increasing distance from the chill surface, increasing local solidification time and decreasing cooling rate. The theoretical coarsening model due to Mortensen was used for estimating further SDAS values presented here.

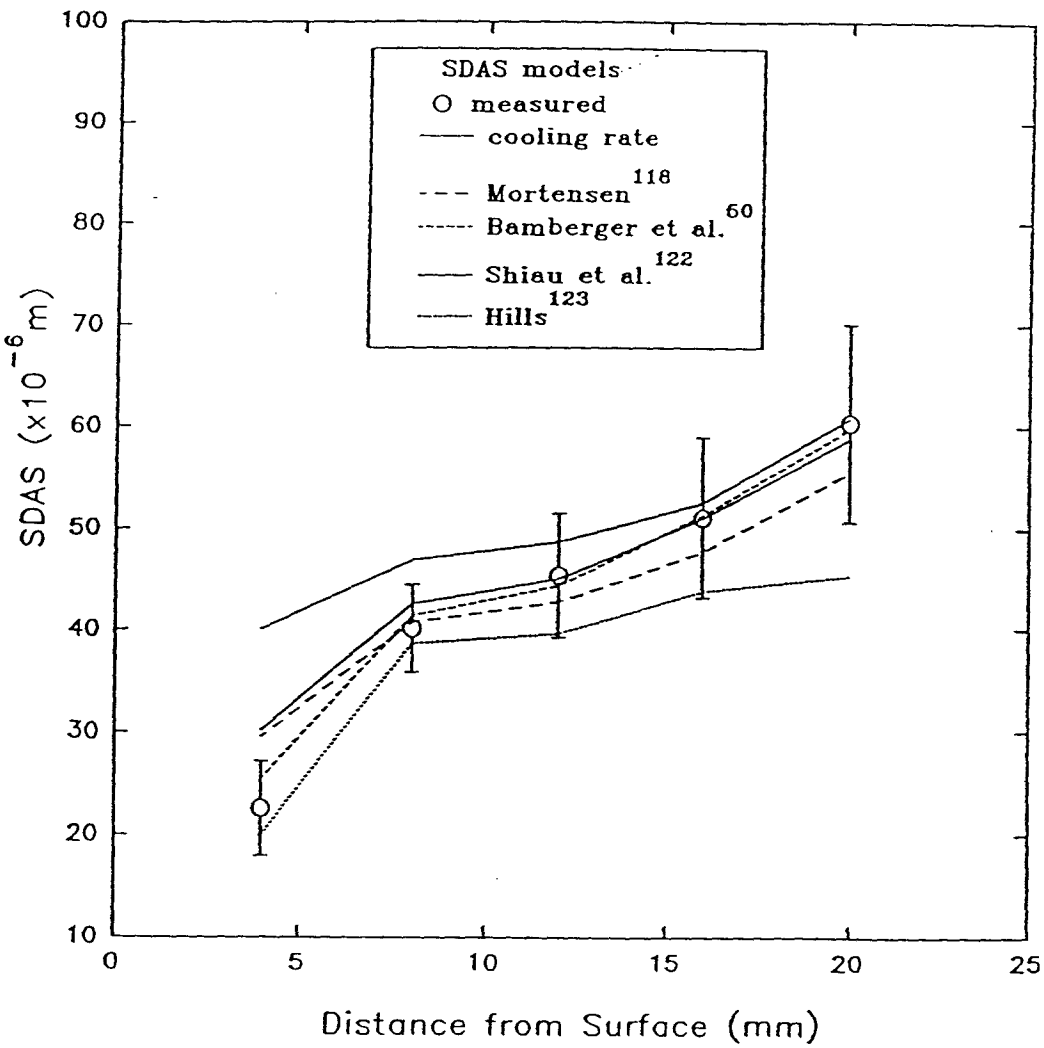

Fig. 6.4 Typical calculated and measured secondary dendrite arm spacing for Al-7% Si and copper chill (superheat=30°C).

6.3 Effect of Process Variables

6.3.1 Effect of Surface Roughness

The effect of surface roughness on heat flow and microstructure formation is shown in Figs. 6.5 and 6.6. It is evident that heat extraction increases with increasing surface smoothness of the chill. This is manifested as increasing shell thickness and decreasing secondary dendrite arm spacing as surface roughness decreases. It is observed that at the lower range of roughness values covered in this study, an increase of roughness from 0.018μm to 0.03μm (~1.67 times) decreases the heat flux by an average of 8.5% while the heat transfer coefficient decreases by 14%. If the surface roughness is further increased to 0.291μm (~16 times), the heat flux decreases by an average of 11% while the heat transfer coefficient decreases by an average of 17%. This result is in agreement with the findings of other researchers[33,35,39,42-44]. Prates and Biloni[33] found that an empirical relationship exists between the surface microprofile and the overall constant heat transfer coefficient in the form:

$$h^2 = CRa^{-n} \tag{6.1}$$

Values of C=4.68 x 10^6 and n=-0.03 reveal a very good fit (R^2=0.96) for h_{max} in the particular case of Al-7%Si and copper chill.

The influence of surface microgeometry on heat transfer and microstructure can be explained by considering the initial contact between the surface layer of a liquid metal and the mold surface. The first grains nucleate at the peaks or cusps of surface microprofile in a predendritic mode, thereby leading to thermal supercooling of surrounding liquid. This thermal supercooling subsequently increases the liquid surface tension. The increase in surface tension reduces fluidity and, coupled with volume contraction as more liquid solidifies, reduces the chances of the liquid contacting the surface valleys. The implication of this is that increasing surface roughness decreases the total casting/mold contact area, thereby leading to lower heat

transfer rate. As a result of the localized solidification at the cusps, the surface roughness of the solidified shell is expected to increase with increasing surface roughness of the chill surface. This was confirmed by measurements of the surface microprofile of the solidified shell and the result is depicted in Table 6.2. It is also observed that when the surface roughness of the chill is low (< 1μm), the solidified shell is rougher than chill surface. On the other hand, at higher chill surface roughness (> 1μm), the surface of the solidified shell is smoother than that of the chill.

Table 6.2 Measured shell surface roughness for various chill surface microprofile.

Chill Surface Roughness (μm)	Shell Surface Roughness (μm)						
	1	2	3	4	5	Mean	Std**
0.018	1.60	1.34	1.07	1.03	1.19	1.25	0.23
0.030	2.01	1.44	1.08	1.58	1.24	1.47	0.36
0.291	2.67	2.39	3.01	2.84	2.23	2.63	0.32
5.61	3.28	3.74	3.07	2.98	3.82	3.37	0.38
10.56	3.53	3.18	3.76	4.03	3.45	3.59	0.32

** Std stands for standard deviation

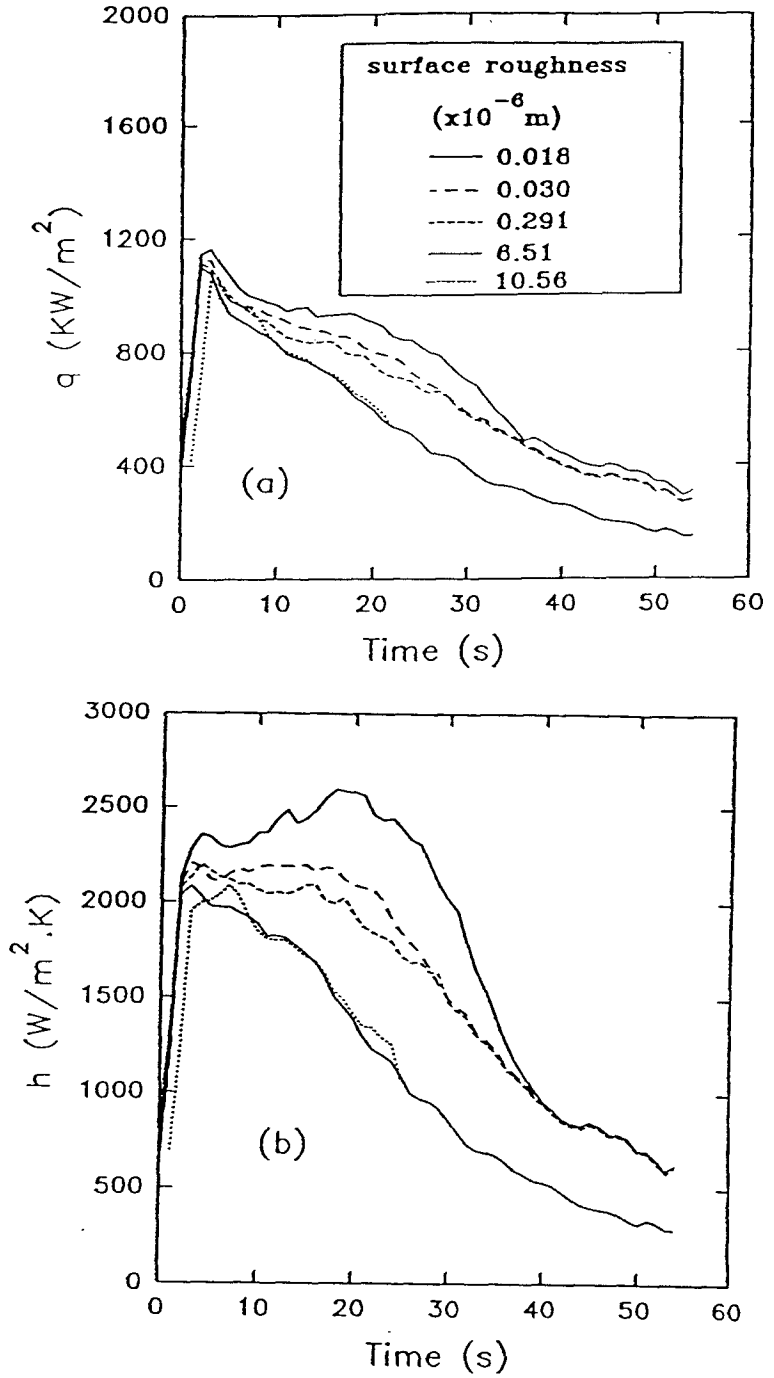

Fig. 6.5 Effect surface roughness on heat transfer for Al-7% Si and copper chill (superheat=30°C) - (a) interfacial heat flux, (b) heat transfer coefficient.

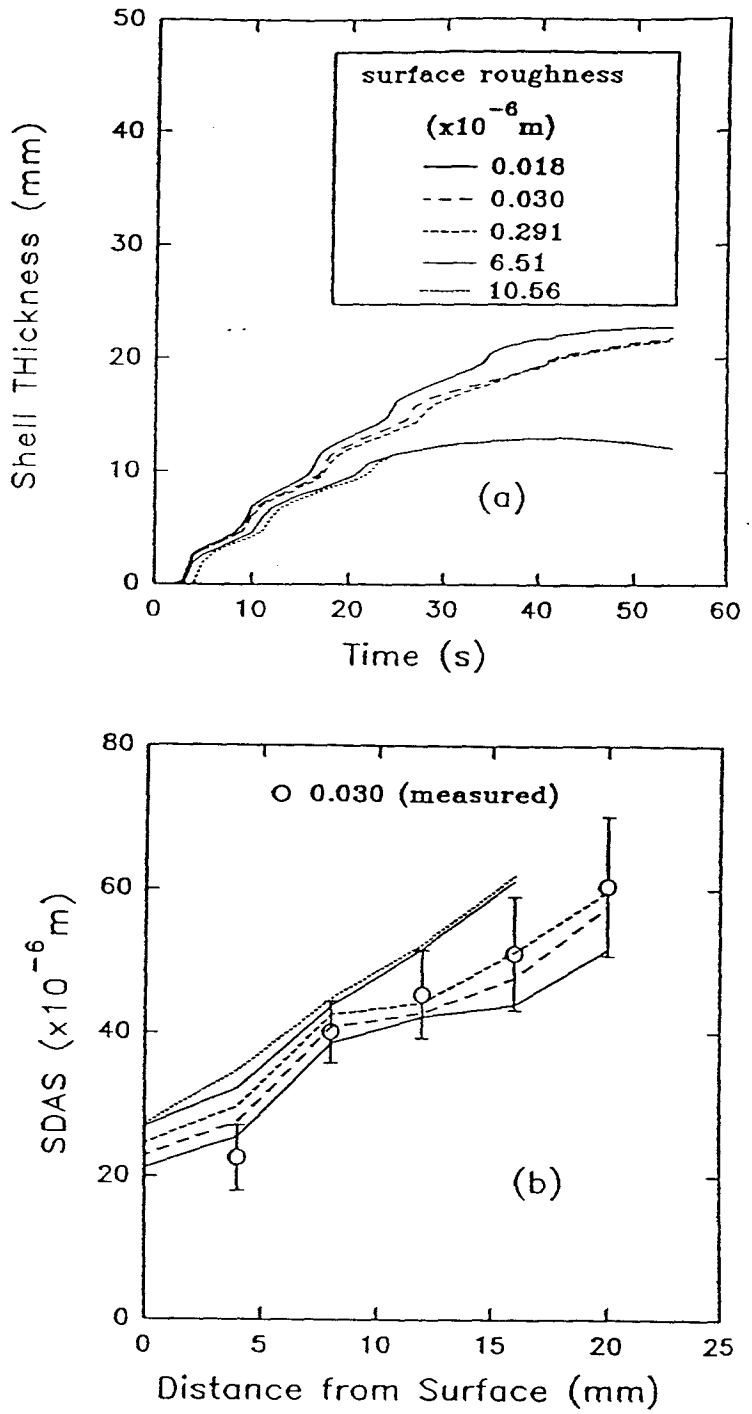

Fig. 6.6 Effect surface roughness on solidification and microstructure for Al-7% Si and copper chill (superheat=30°C) - (a) shell thickness (b) secondary dendrite arm spacing.

6.3.2 Effect of Chill Material

The effect of chill material on heat flow and microstructure formation is shown in Figs. 6.7 and 6.8. The heat flux and heat transfer coefficient increase with increasing thermal diffusivity of the chill material. This result is in agreement with others reported in the literature[33,35,37,39,43,47,49]. Kumar et al.[49] found that the maximum interfacial peak heat flux (q_{max}) can be expressed as a power function of the thermal diffusivity and thickness of chill as shown in Eq. (2.3). A similar expression was found to exist in the present studies. For Al-7%Si, this expression is of the form:

$$q_{\max} = 2520\left(\frac{\alpha_m}{X_m}\right)^{0.107} \qquad KW/m^2 \qquad (R^2 = 0.965) \qquad (6.2)$$

The secondary dendrite arm spacing decreases with increasing thermal diffusivity of the chill material. The effect of chill material on the heat extraction and microstructure can be explained by recalling that the chill thermal properties (thermal diffusivity, expansion coefficient, emissivity and absorptivity) and surface oxidation characteristics are important factors in each stage of the solidification process. The ability of the chill to absorb and transport heat is of paramount importance during the first stage of solidification when there is casting/mold contact. The thermal diffusivity of each of the chills decreases with increasing temperature. The variation of the chill thermal diffusivity with temperature manifests in the chill thermal resistance (X_m/k_m), increasing thermal diffusivity resulting in decreasing thermal resistance. The variation of the thermal resistance of each of the chills with time is depicted in Fig. 6.9. It is obvious that copper has the least thermal resistance among the four materials and therefore, exhibited the highest heat extraction rate. At the onset of the air gap, the radiation properties of the chills could become important although the main mode of heat transfer is conduction of heat across the air gap.

The effect of chill material on the surface roughness of the solidified shell is shown in Table 6.3 for a chill surface roughness of 0.03μm. Unlike the chill surface roughness, it is apparent that the chill material has no pronounced effect on the surface quality of the shell.

Table 6.3 Measured shell surface roughness for different chill materials of similar microprofiles.

Chill Material	Shell Surface Roughness (μm)						
	1	2	3	4	5	Mean	Std**
copper (Ra=0.03μm)	2.01	1.44	1.08	1.58	1.24	1.47	0.36
brass (Ra=0.03μm)	1.58	2.13	1.34	1.17	1.27	1.50	0.38
steel (Ra=0.03μm)	1.23	1.79	1.49	1.36	1.35	1.44	0.21
cast iron (Ra=0.03μm)	1.71	1.58	2.03	1.16	1.07	1.51	0.40

** Std stands for standard deviation

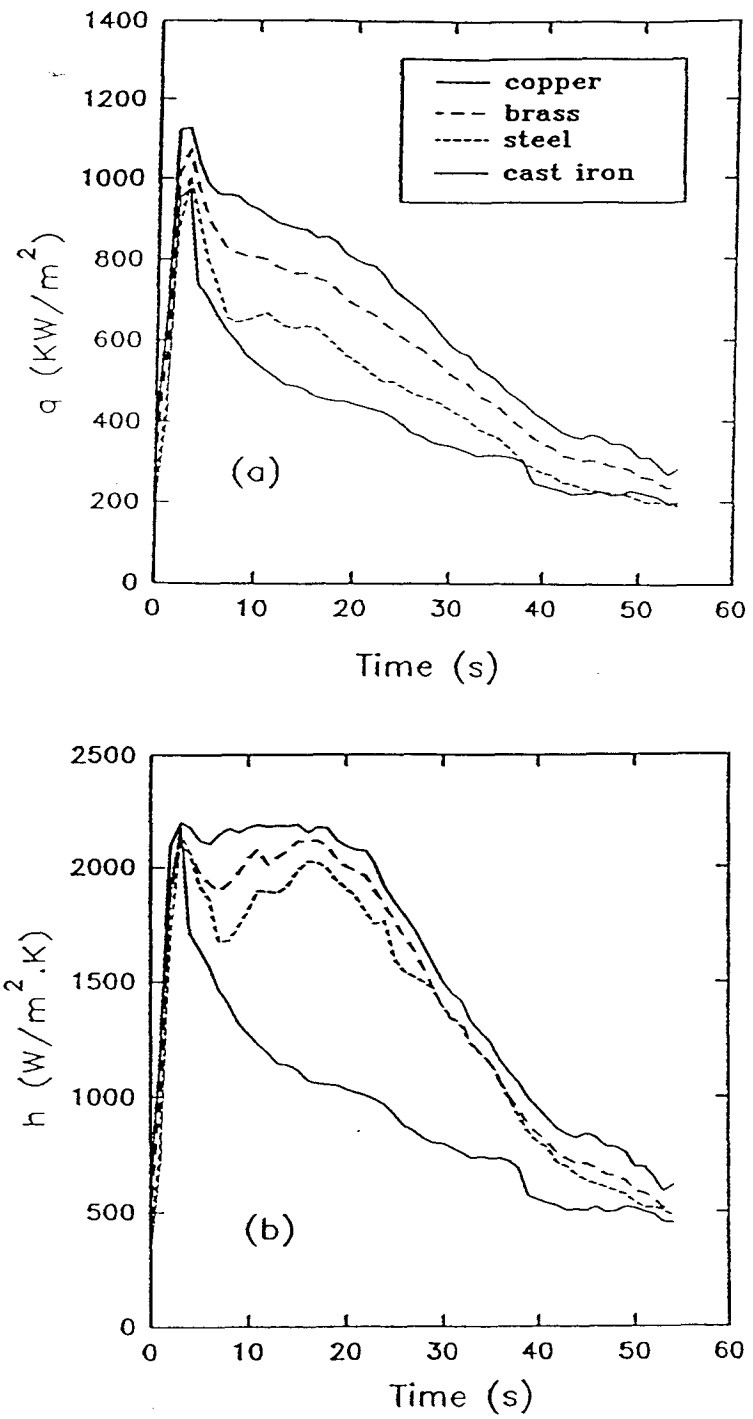

Fig. 6.7 Effect chill material on heat transfer for Al-7% Si (superheat=30°C) - (a) interfacial heat flux, (b) heat transfer coefficient.

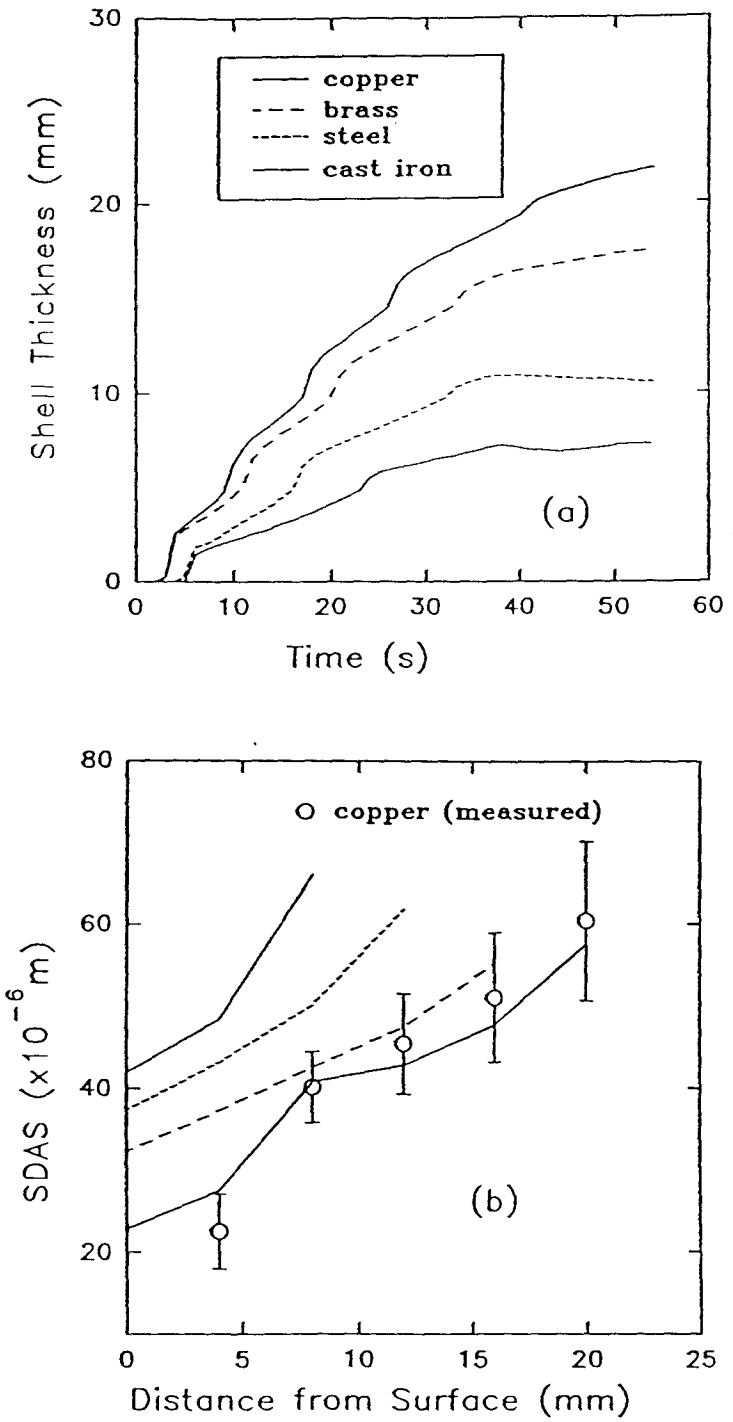

Fig. 6.8 Effect chill material on solidification and microstructure for Al-7% Si (superheat=30°C) - (a) shell thickness (b) secondary dendrite arm spacing.

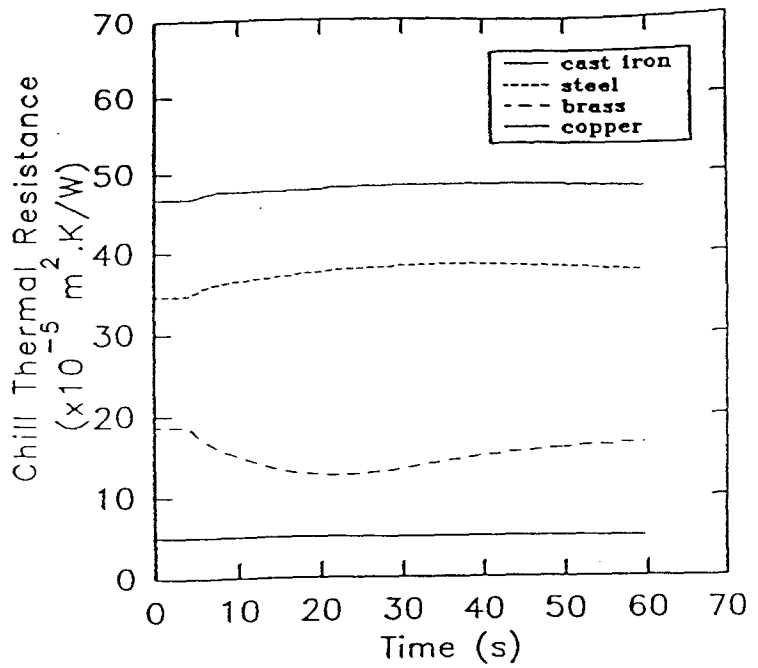

Fig. 6.9 Variation of the chill thermal resistance of with time.

6.3.3 Effect of Superheat

Figs. 6.10 and 6.11 depict the effect of superheat on heat flow and microstructure. The interfacial heat flux and heat transfer coefficient increase with increasing superheat. This higher heat extraction results in greater shell thickness and smaller dendrite arm spacing in agreement with earlier work reported in literature[44-45,143-144]. The influence of superheat on heat extraction can be attributed to an increase in the interfacial contact between melt and chill as the superheat increases. This increase in the interfacial contact with increasing superheat could arise from two sources. Firstly, at higher superheats, the first solid shell that forms is relatively thin and remelts quickly, thereby allowing the melt to spread more uniformly across the surface of the chill. At lower superheats, the initial shell is thick and does not remelt but contracts

away from the chill, creating an interfacial gap which drastically reduce the interfacial heat transfer. Secondly, the fluidity of aluminum alloys increases slightly with increasing superheat[37] and this enhances the spread of the melt across the chill surface such that more surface asperities are filled. Furthermore, the casting superheat determines the extent of the initial driving force (T_c-T_m) for heat transfer across the interface. Increased melt temperature implies an increase in the initial temperature gradient across the mold/metal interface, thereby providing a larger driving force for heat extraction. The increase in interfacial contact area coupled with increasing driving force accounts for the increase in heat transfer with increasing superheat.

The fact that the increase in heat extraction with increasing superheat is due to the nature of the melt/chill interface was confirmed with measurements of the surface roughness of the solidified shell as shown in Table 6.4. It was found that the surface roughness of the solidified shell becomes smoother as the superheat increases. It is noted that the same chill surface microprofile was utilized in all the experiments. The mechanism proposed here is further confirmed by a similar result in literature[45] which showed that the wetting of the mold by the melt is the dominant factor that controls the heat transfer coefficient when liquid tin at different superheats was dropped and solidified on a cylindrical chill of brass, stainless steel, nickel or chromium plated brass.

When solidification recommences after remelting at high superheats, part of the melt superheat would have been lost to the chill and coupled with increased contact at the interface, the interfacial heat extraction increases, leading to the observed increase in shell thickness and the decrease in secondary dendrite arm spacing. The increase in shell thickness with increasing superheat implies that the solidification rate increases as the superheat is increased.

This indicates that higher superheats resulted in higher thermal gradient at the solidification front. It has been shown that under conditions of semi-infinite unidirectional solidification, the motion of the solid/liquid interface can be described by the expression[33]

$$S(t) = A.erf(Bh_i)t^{1/2} - C(T_c - T_L)^{1/2} \tag{6.3}$$

which shows that the shell thickness is a function of both heat transfer coefficient (h_i) and superheat (T_c-T_L). Therefore, the shell thickness can increase with increasing superheat if the increase in heat transfer coefficient supersedes the effect of the superheat and, this is the case in this study.

The decrease in secondary dendrite arm spacing with increasing superheat confirms the existence of higher thermal gradients at the solidification front at higher superheats. It has been found that in unidirectional solidification, the presence of a positive temperature gradient in front of the dendrite tip generally causes the velocity of the tip to be retarded to a greater extent than the root at the commencement of solidification, thereby decreasing the mushy zone length[144]. As solidification progresses, the tip exhibits a speed up effect. The combination of the reduction in mushy zone length and the speed up effect of the dendrite tip reduces the local solidification time. A positive temperature gradient can be maintained in front of the dendrite tips by use of superheat in the absence of convection or by supplying a heat input to the melt in the presence of convection[144]. Hence, the net effect of increasing superheat in the absence of convection is the acceleration of solidification with a consequent refinement of microstructure. The fact that this was the case in our experiments support the fact that the dipping mechanism substantially reduced the effect of liquid convection during solidification.

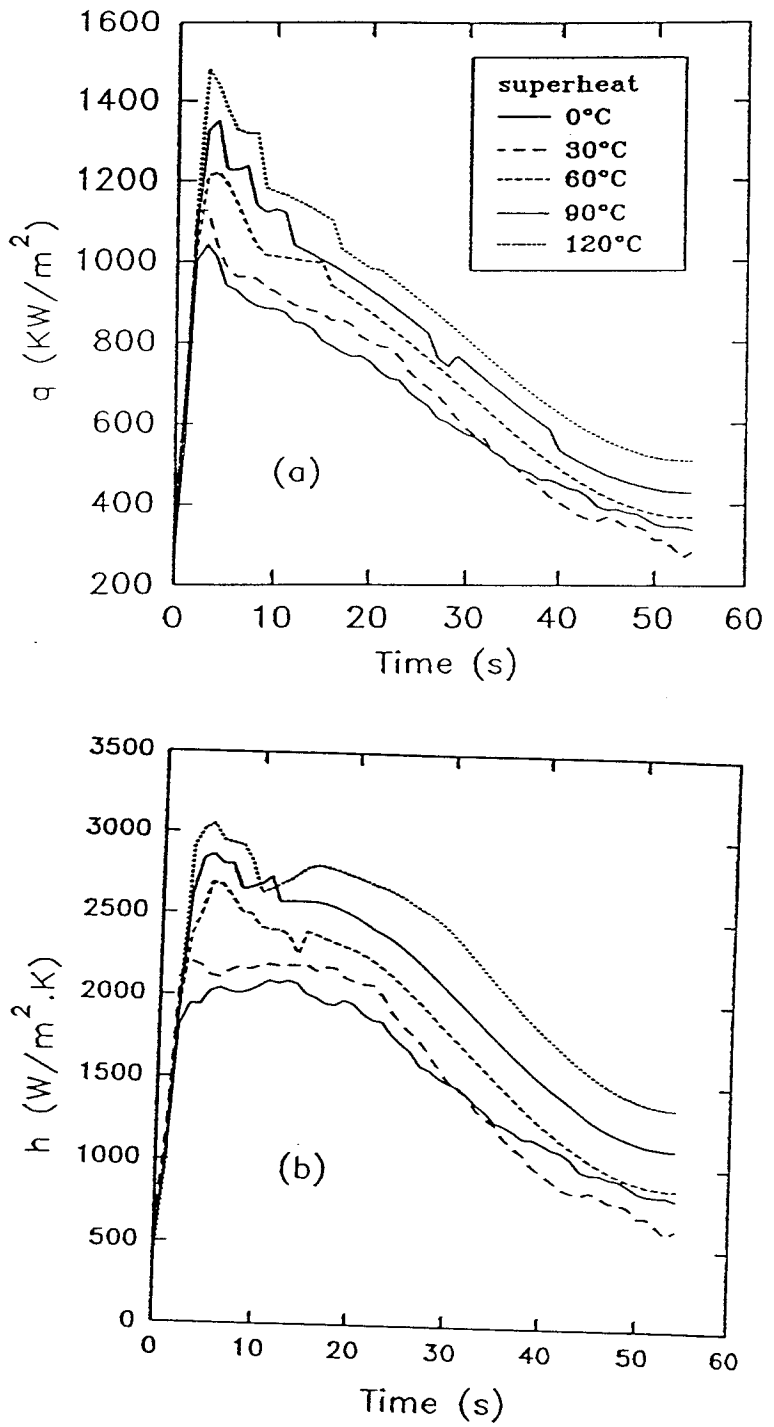

Fig. 6.10 Effect superheat on heat transfer for Al-7% Si and copper chill - (a) interfacial heat flux, (b) heat transfer coefficient.

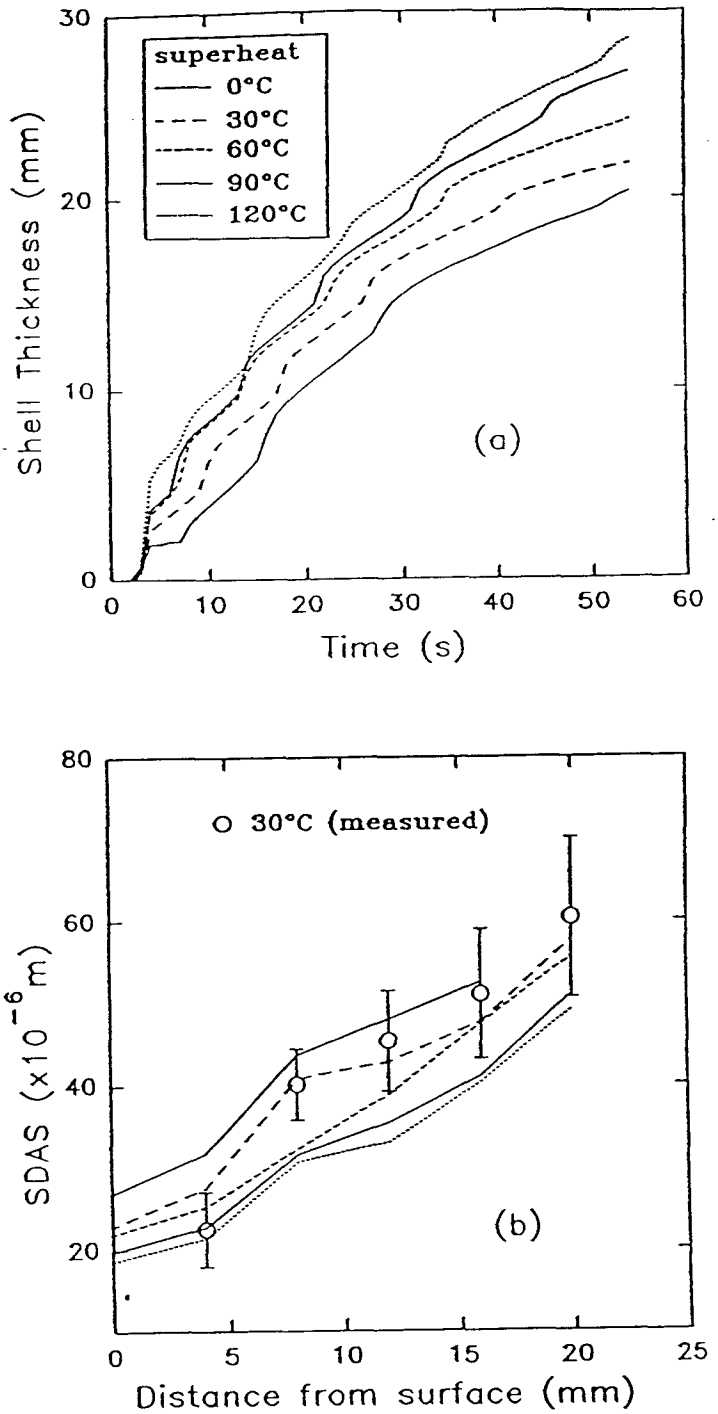

Fig. 6.11 Effect superheat on solidification and microstructure for Al-7% Si and copper chill - (a) shell thickness (b) secondary dendrite arm spacing.

Table 6.4 Measured shell surface roughness for various superheats.

Superheat (°C)	Shell Surface Roughness (μm)						
	1	2	3	4	5	Mean	Std**
0	2.35	2.47	1.98	2.15	2.08	2.21	0.20
30	2.01	1.44	1.08	1.58	1.24	1.47	0.36
60	1.18	1.60	1.51	1.09	1.12	1.30	0.24
90	0.98	1.16	1.34	1.00	1.10	1.12	0.15
120	0.83	1.15	1.29	0.90	0.98	1.03	0.19

** Std stands for standard deviation

6.3.4 Effect of Alloy Composition

Figures 6.12 and 6.13 depict the effect of alloy composition on heat flow and microstructure. With reference to the Al-Si alloys, the heat flux and heat transfer coefficient increase with decreasing silicon content of the alloy. It is noted that the heat flux and heat transfer coefficient for Al-3%Si and Al-5%Si exhibited much steeper gradients at the first 15s than the Al-7%Si. The secondary dendrite arm spacing also increases with decreasing silicon content while the shell thickness decreases. This result is similar to the findings of Bamberger et al.[50] who investigated heat flow and dendrite arm spacings of Al-Si alloys ranging from 3.8 to 9.7%Si. Other results pertaining to secondary dendrite arm spacing in hypoeutectic alloys indicate a decrease in spacing with increasing solute content[108,145-147].

The increase in interfacial heat flux and heat transfer coefficient with a decrease in silicon content resulted from two main factors. Firstly, the casting temperature increases as the silicon content decreases due to the increase in the liquidus temperature. Thus, at a superheat of 30°C, the casting temperature for alloys, Al-7%Si, Al-5%Si and Al-3%Si, were 640°C, 662°C and 678°C respectively. The increase in casting temperature translates to an equivalent increase in the initial driving force for solidification. Secondly, there is an increase in the thermal

diffusivity of the alloys as the silicon content decreases. Both factors allow for an increase in heat extraction as the silicon content decreases such that instant freezing of the first shell around the cusps of surface microprofile is expected to be more prevalent for Al-3%Si than for Al-7%Si. When this happens, uniform spreading of the melt across the chill surface is hampered such that less surface asperities are filled and this reduces the interfacial contact area. The filling of surface asperities is further aggravated by the decreasing fluidity since the fluidity of hypoeutectic alloys is known to be inversely proportional to the freezing range[136]. The initial high heat extraction rate for Al-3%Si and Al-5%Si leads to a relatively thick shell, which subsequently contracts away from the chill surface, creating an interfacial gap. This gap brings about the rapid reduction in interfacial heat transfer and consequently the solidification rate. Measurement of the surface roughness of the solidified shell (Table 6.5) revealed that the shell surface smoothness increases with increasing silicon content and this agrees with the proposed mechanism.

The decrease in the solidification rate with decreasing silicon content can also be attributed to the increase in the mushy zone of these alloys as the silicon content decreases. It has been found that the secondary dendrite arm spacing is directly proportional to the extent of the mushy zone in hypoeutectic binary alloys[145]. This indicates that the solidification rate is inversely proportional to the extent of the mushy zone since the secondary dendrite arm spacing decreases with increasing solidification rate. The increase in mushy zone length as the silicon content decreases implies that the latent heat is released over a longer period, thereby resulting in a decrease in solidification rate that is manifested as reduced shell thickness and coarser microstructure.

The increase in solidification rate and the consequent decrease in secondary dendrite arm spacing have further been explained in terms of the kinetics of dendritic growth[147,148]. It has been proposed that dendritic growth occurs in two different stages - an initial transient

stage followed by a quasi-stationary stage[148]. The initial transient stage starts just behind the dendrite tip and extends until the solute diffusion fields from adjacent dendrites overlap. This stage is characterized by a rapid and dynamic increase in the solid volume fraction and is accelerated by high solute content and/or fast growth rate. The quasi-stationary stage is characterized by the dendritic coarsening and is accelerated by low solute content and/or low growth rate. Therefore, the main effect of decreasing the silicon content in Al-Si alloys is the retardation of transient stage and an acceleration of the coarsening stage, which finally results in an increase in secondary dendrite arm spacing.

Table 6.5 Measured shell surface roughness for different alloy compositions.

Alloy Composition	Shell Surface Roughness (μm)						
	1	2	3	4	5	Mean	Std**
Al-7%Si	2.01	1.44	1.08	1.58	1.24	1.47	0.36
Al-5%Si	2.88	2.45	1.70	2.40	1.98	2.28	0.46
Al-3%Si	2.43	3.02	3.75	3.16	2.99	3.07	0.47

** Std stands for standard deviation

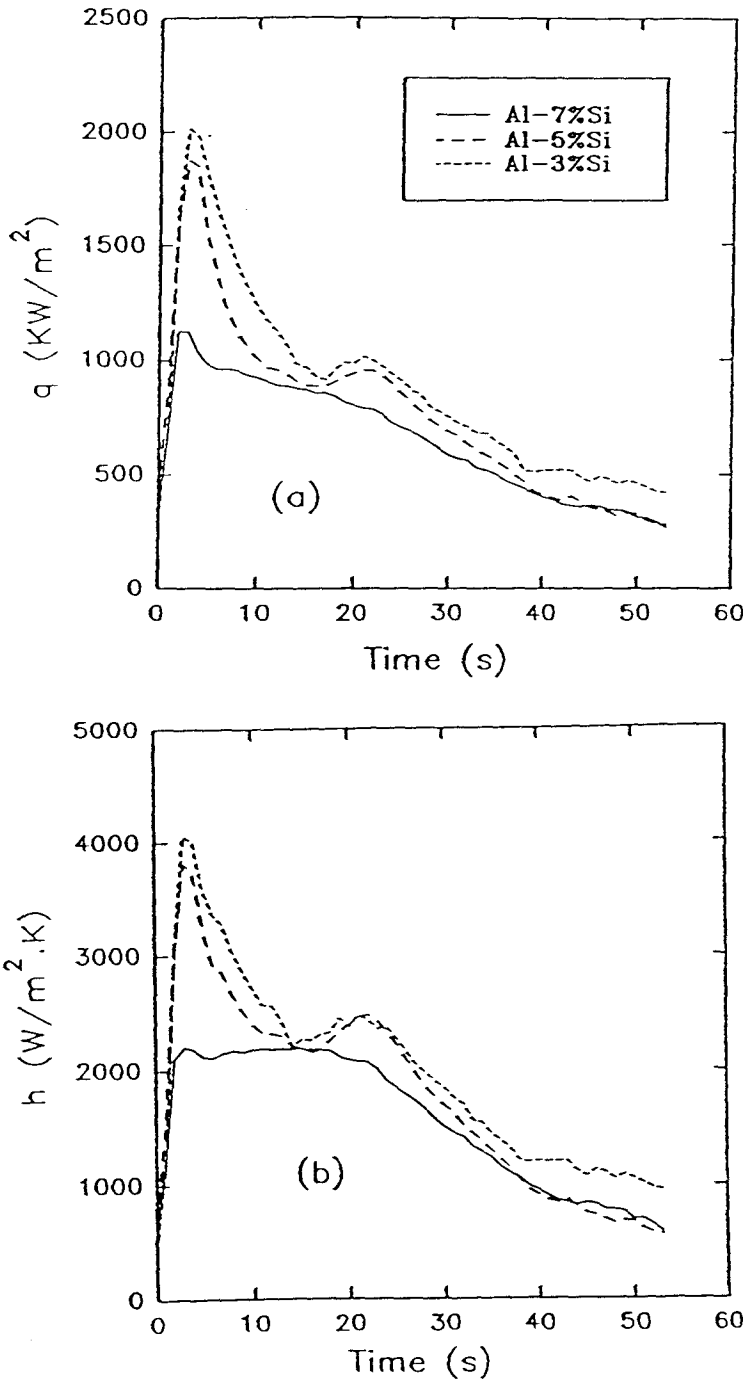

Fig. 6.12 Effect of alloy composition on heat transfer for Al-Si alloys and copper chill (superheat=30°C) - (a) interfacial heat flux, (b) heat transfer coefficient.

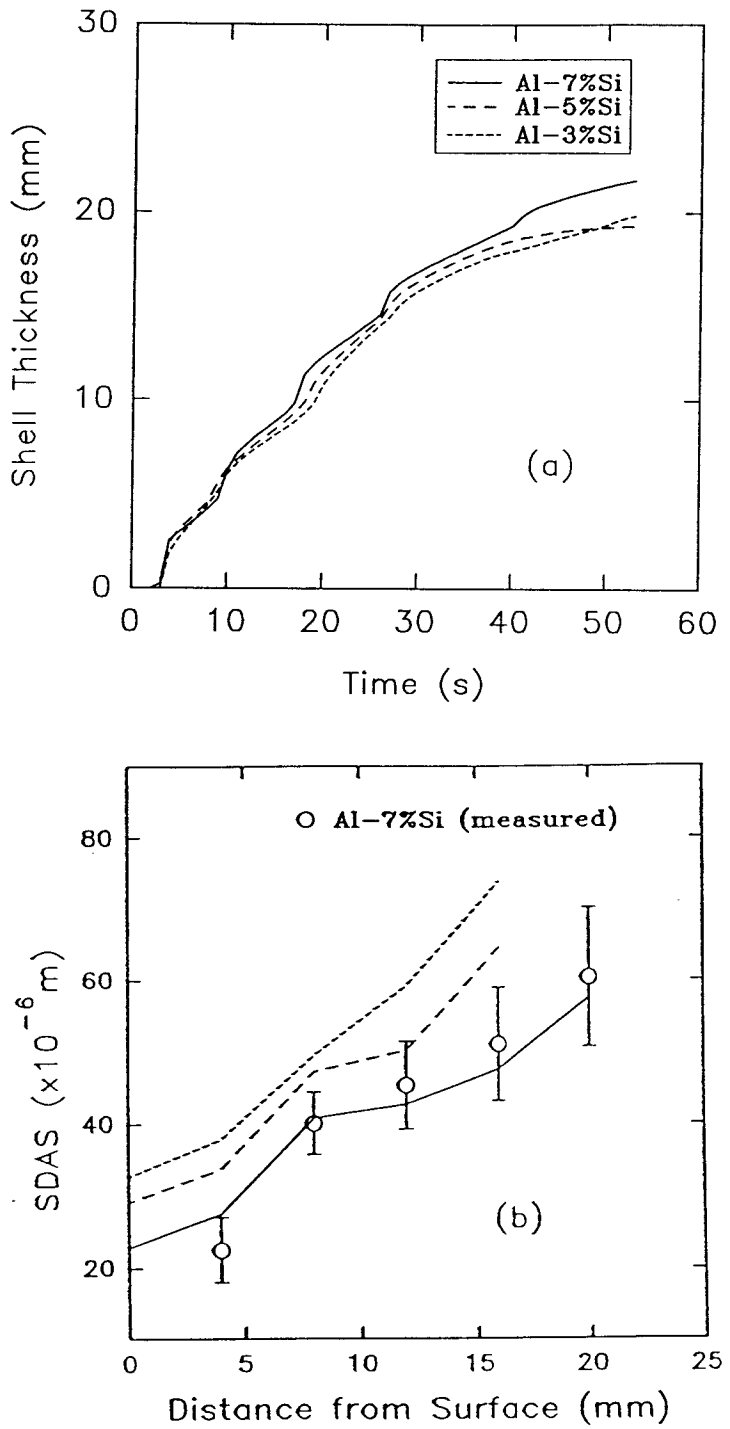

Fig. 6.13 Effect of alloy composition on solidification and microstructure for Al-Si alloys and copper chill (superheat=30°C) - (a) shell thickness (b) secondary dendrite arm spacing.

6.3.5 Effect of Oil Film

The effect of oil film on heat flow and microstructure is presented in Figs. 6.14 and 6.15. It is noted that these oils were developed for, and are being used in, the continuous casting of steel billets as lubricants. Oil films increase the interface thermal resistance at initial contact. This trend is clearly manifested in the first few seconds of solidification for the temperature, heat flux, heat transfer coefficient and shell thickness profiles for the various oils. The maximum heat flux decreases with increasing flash point of oil (see Table 4.3 for the flash points of the oils) while the time to attain this maximum value increases. The heat flux increases with increasing flash point for subsequent times after the peak value. The heat transfer coefficient also increases with increasing flash point of oil. It is noted that flash point of these oils increases with increasing boiling range and decreasing viscosity. The increase in both heat flux and heat transfer coefficient results in increasing shell thickness and decreasing secondary dendrite arm spacing at a given location.

This effect can be explained as follows. The oil film acts as an additional thermal barrier upon contact of the chill by the metal thereby increasing the thermal resistance at the interface. However, within a short time, the oil temperature reaches its flash point, pyrolysing or combusting and, releasing gases into the growing gap at the interface. This was observed to happen during the experiments in the form of oil smoke that appeared a few seconds after dipping. Model predictions of the surface temperature profiles for the chill and solidifying shell (Fig. 6.16) indicate that while the oil layer near the shell surface reaches its flash point, the layer adjacent to the chill does not reach this temperature. This was confirmed by the fact that an oil film somewhat thinner than when first applied, was observed to remain at the chill surface in all cases.

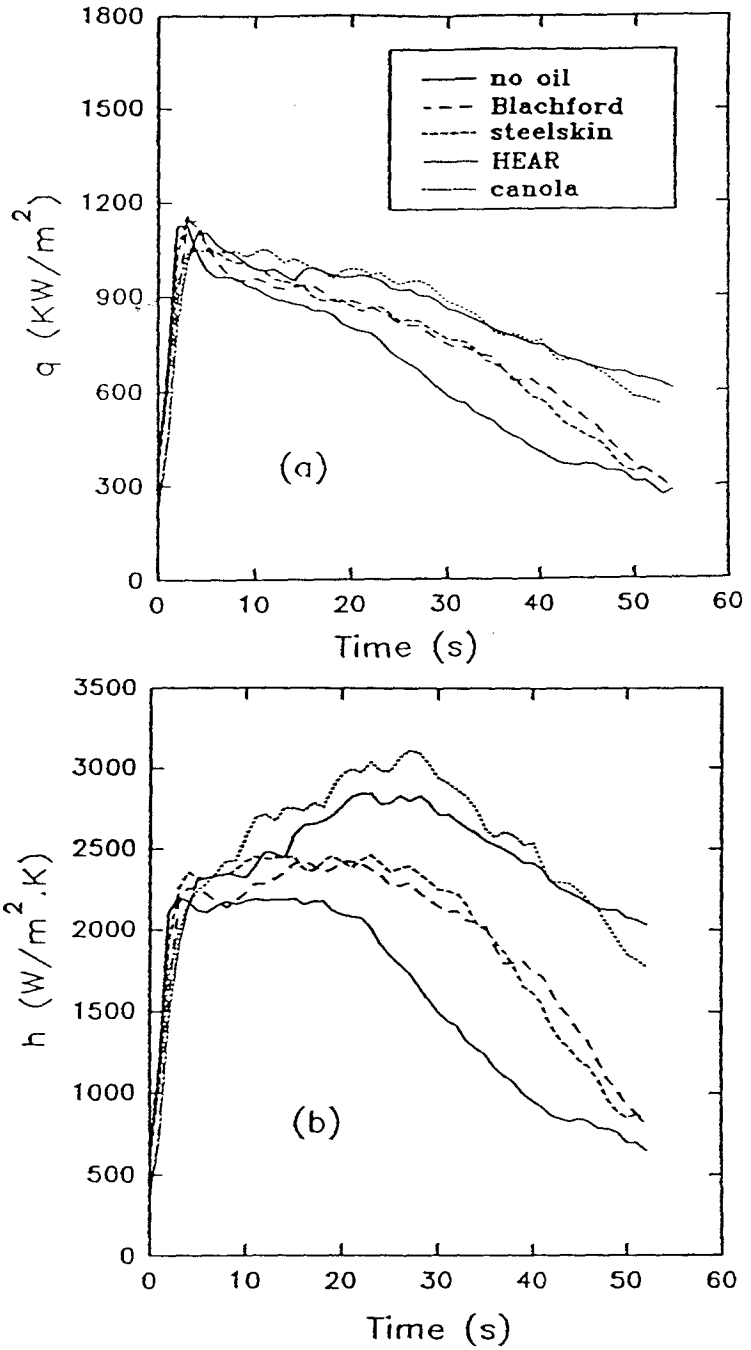

Fig. 6.14 Effect of oil film on heat transfer for Al-7% Si and copper chill (superheat=30°C) - (a) interfacial heat flux, (b) heat transfer coefficient.

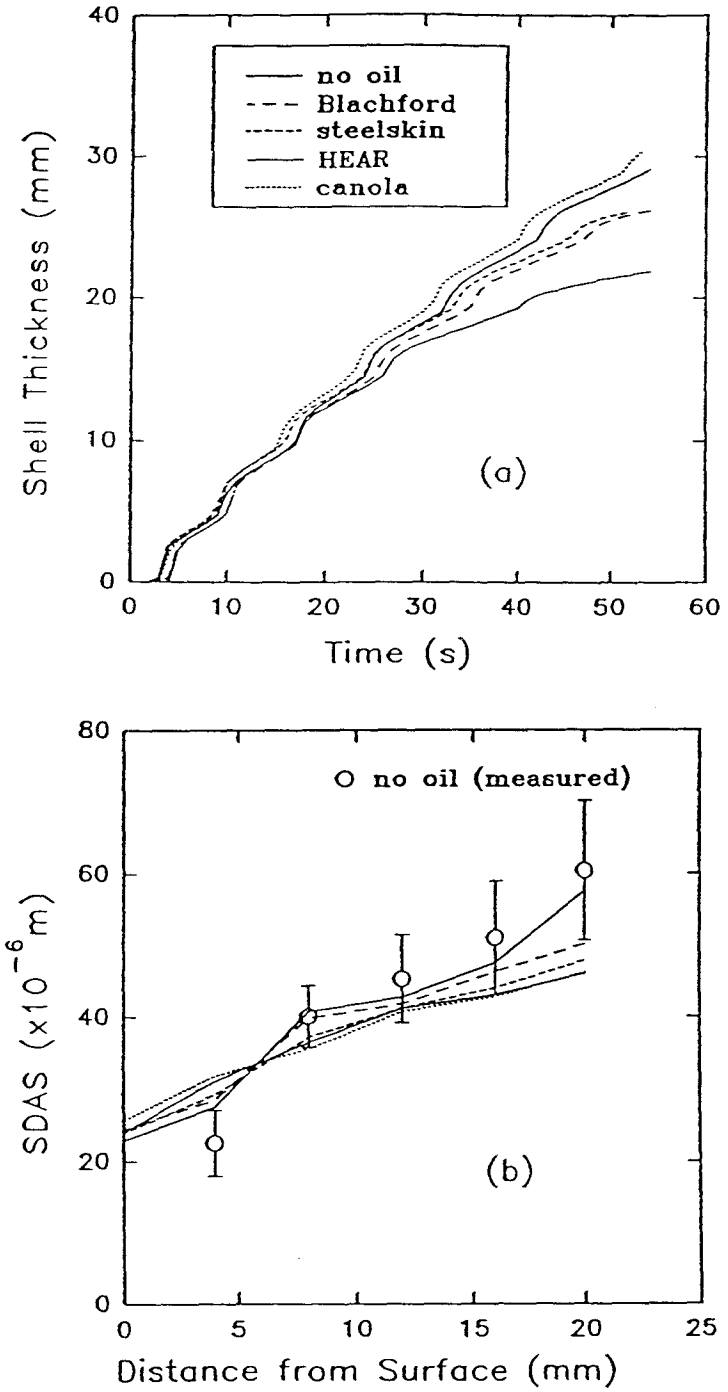

Fig. 6.15 Effect of oil film on solidification and microstructure for Al-7% Si and copper chill (superheat=30°C) - (a) shell thickness (b) secondary dendrite arm spacing.

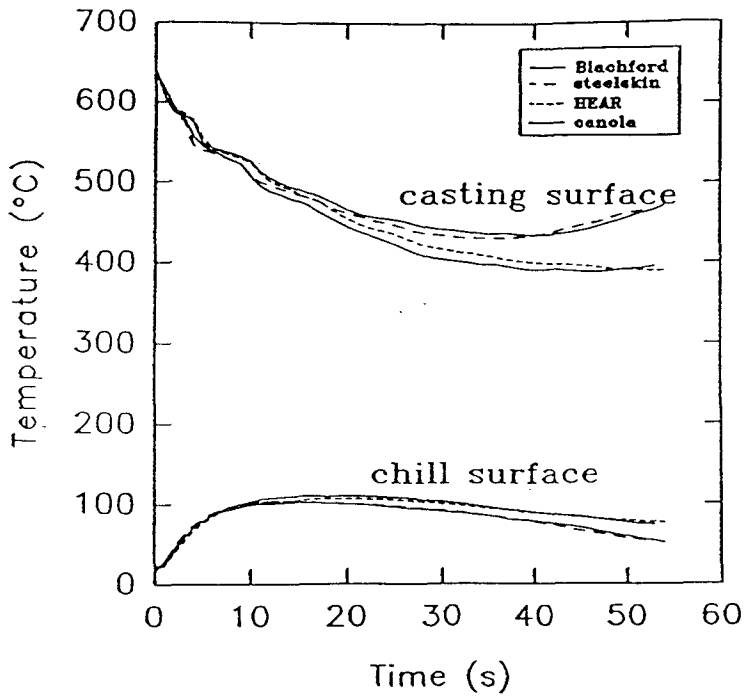

Fig. 6.16 Calculated surface temperature profiles of chill and solidifying shell for the four oils.

The surface roughness of the solidified shell increases slightly with decreasing flash point and boiling range of the oils as shown in Table 6.6. It is also apparent from Table 6.6. that there is a slight increase in the surface roughness of the solidified shell with the oils when compared to the case of no oil. This could be attributed to the pressure exerted on the first semi-solid shell that form by the products of oil boiling and pyrolysis.

In general, oils are esters of fatty acid and glycerol. Fatty acids are long straight chained hydrocarbons having a carboxylic acid group (-COOH) attached at one end while glycerol is a trihydroxy alcohol (CH_2OH-$CHOH$-CH_2OH). The properties of oils depend on the chain length of the molecule, on the degree of saturation, on the geometric isomerism and on the relative positions of the double bonds with respect to the carboxyl group and each other[149]. In

the presence of heat and absence of oxygen, oils undergo thermally induced homolysis, a type of pyrolysis that results in rupture of carbon bonds and fragmentation into smaller units. Once formed, these smaller units or free radicals can enter into typical propagation reactions yielding new free radicals. These chains of reactions continue until a termination stage is attained. The termination steps in pyrolysis of a given free radical may be either the joining together (coupling) of two free radicals or their disproportionate (one is oxidized while the other is reduced).

Table 6.6 Measured shell surface roughness for the four oils.

Oil	Shell Surface Roughness (μm)						
	1	2	3	4	5	Mean	Std**
No oil	2.01	1.44	1.08	1.58	1.24	1.47	0.36
Blachford Oil	1.43	1.58	1.97	1.44	1.34	1.55	0.25
Steelskin Oil	1.49	1.56	1.45	1.62	1.46	1.52	0.07
HEAR Oil	1.18	1.71	1.32	1.48	1.78	1.49	0.25
Canola Oil	1.48	1.33	1.23	1.83	1.53	1.48	0.24

** Std stands for standard deviation

In the presence of heat and a limited amount of oxygen, oils oxidize and undergo incomplete combustion in a number of stages, producing mainly carbon monoxide, water vapour and carbon black or soot. If excess oxygen is available together with heat, oils undergo complete combustion, yielding mainly carbon dioxide and water vapour in the final stage. Combustion of most organic compounds produce energy as a by-product. Thus in the presence of heat and oxygen, oils undergo a complex set of reactions producing H_2, CO, CO_2, H_2O, C, and hydrocarbons. Some of these gases (mainly H_2 and hydrocarbons) have higher conductivity than air and hence, enhances the heat conduction across the air gap.

It is observed that Canola and HEAR oils enhance heat transfer more than the Steelskin and Blachford oils. It is established that the double bonds and the carboxyl groups in oils are the main reactive sites during pyrolysis and combustion. Hence, the rate of reaction increases with increasing number of double bonds (increasing unsaturation) and increasing length of carbon chains. With reference to Table 4.3, all the components of the oils except palmitic acid contain double bonds. Linolenic acid has three double bonds, linoleic acid has two double bonds while the three remaining components have one double bond each. Hence, although the total percentage of unsaturated components are about the same for these four oils (91.5% for Canola, 92.7% for HEAR, 93.8% for Steelskin and 92.1% for Blachford), Steelskin and Canola oils will exhibit greater unsaturation behavior than HEAR and Blachford oils. In terms of the total length of carbon chains, HEAR oil has the longest chain due its high euricic acid content while the chain length for the remaining three are about equal. Therefore, the high heat extraction rate with Canola oil can be attributed to its relatively high unsaturation level. On the other hand, the high heat extraction with HEAR oil can be due to its relatively long carbon chains. Although high heat extraction is expected for Steelskin oil due to its high unsaturation, it appears the length and arrangement of the carbon chains may have superseded this unsaturation factor. Blachford oil has the lowest heat extraction due its modest unsaturation and carbon chain length. Furthermore, the differences in the heat extraction rates of these oils are influenced by the unknown relative arrangement and positions of the reactive sites.

The exact amount of the evolved gases could not be determined due to the complexity of the possible reactions. A rough estimate could however be made if it is assumed that radiation and gas conduction are the main modes of heat transfer when the gap forms. Calculations based on this assumption reveal that the average gap conductivity likely increased from 0.046 W/m.K to 0.091 W/m.K (~97.8%) to account for the increase in heat extraction observed for the Canola and HEAR oils. In the case of Steelskin and Blachford oils, the increase in the

average gap conductivity is about 40%. Therefore, it would appear that Canola and HEAR oils release higher amounts of H_2 and hydrocarbons into the air gap than Steelskin and Blachford oils.

6.3.6 Effect of Bath Height

Figures 6.17 and 6.18 depict the effect of bath height on heat transfer and microstructure and shows a negligible influence on heat extraction and secondary dendrite arm spacing at the early stages of solidification. This is expected for a unidirectional solidification since the casting/mold surface contact area and other boundary conditions remain the same. Furthermore, the casting thermal resistance is small in relation to interfacial thermal resistance. The major effect of increasing bath height under these conditions should simply be a longer duration of dipping. Bath height also has no significant effect on the shell surface roughness as shown in Table 6.7.

Table 6.7 Measured shell surface roughness for different bath heights.

Bath Height (cm)	Shell Surface Roughness (μm)						
	1	2	3	4	5	Mean	Std**
14	2.01	1.44	1.08	1.58	1.24	1.47	0.36
8.5	1.62	1.10	1.23	1.41	1.95	1.46	0.34
6	1.47	1.56	1.09	2.10	1.24	1.49	0.39

** Std stands for standard deviation

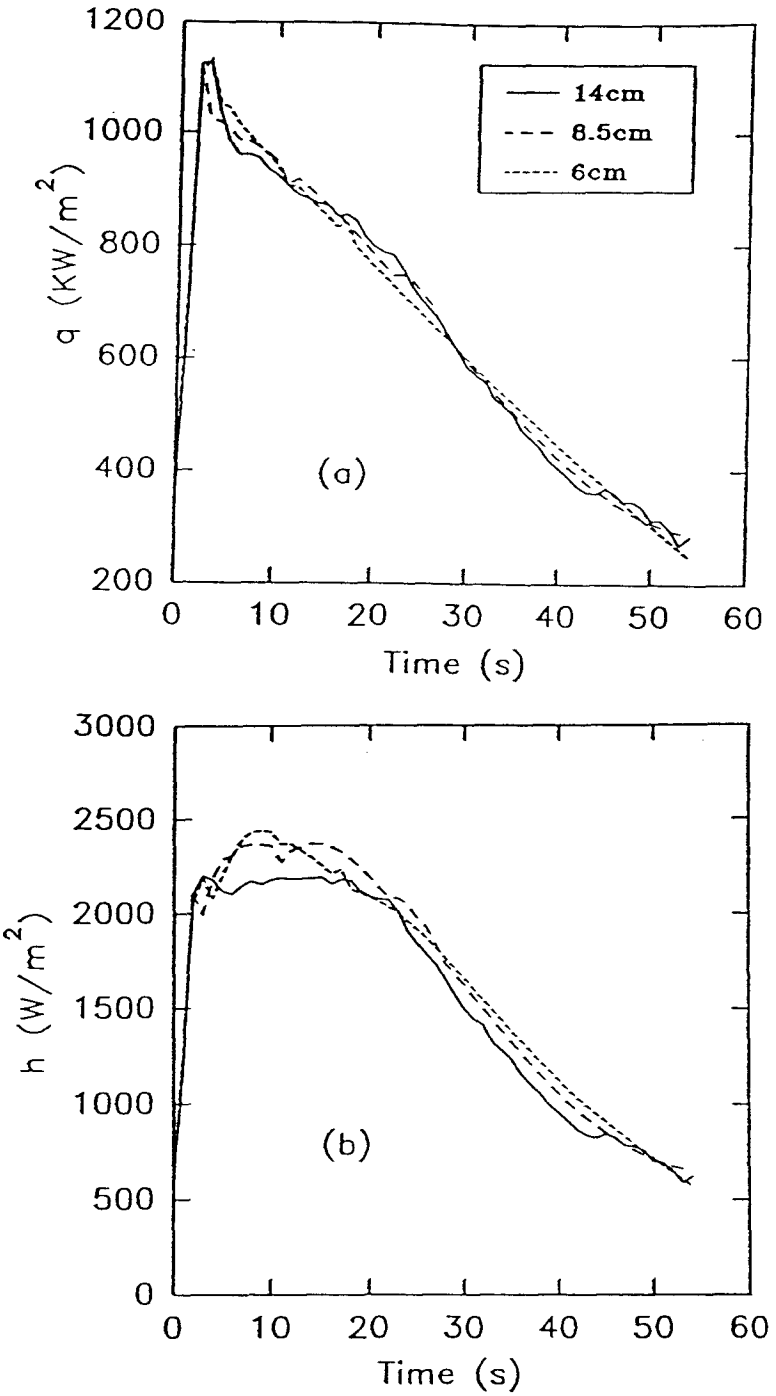

Fig. 6.17 Effect of bath height on heat transfer for Al-7% Si and copper chill (superheat=30°C) - (a) interfacial heat flux, (b) heat transfer coefficient.

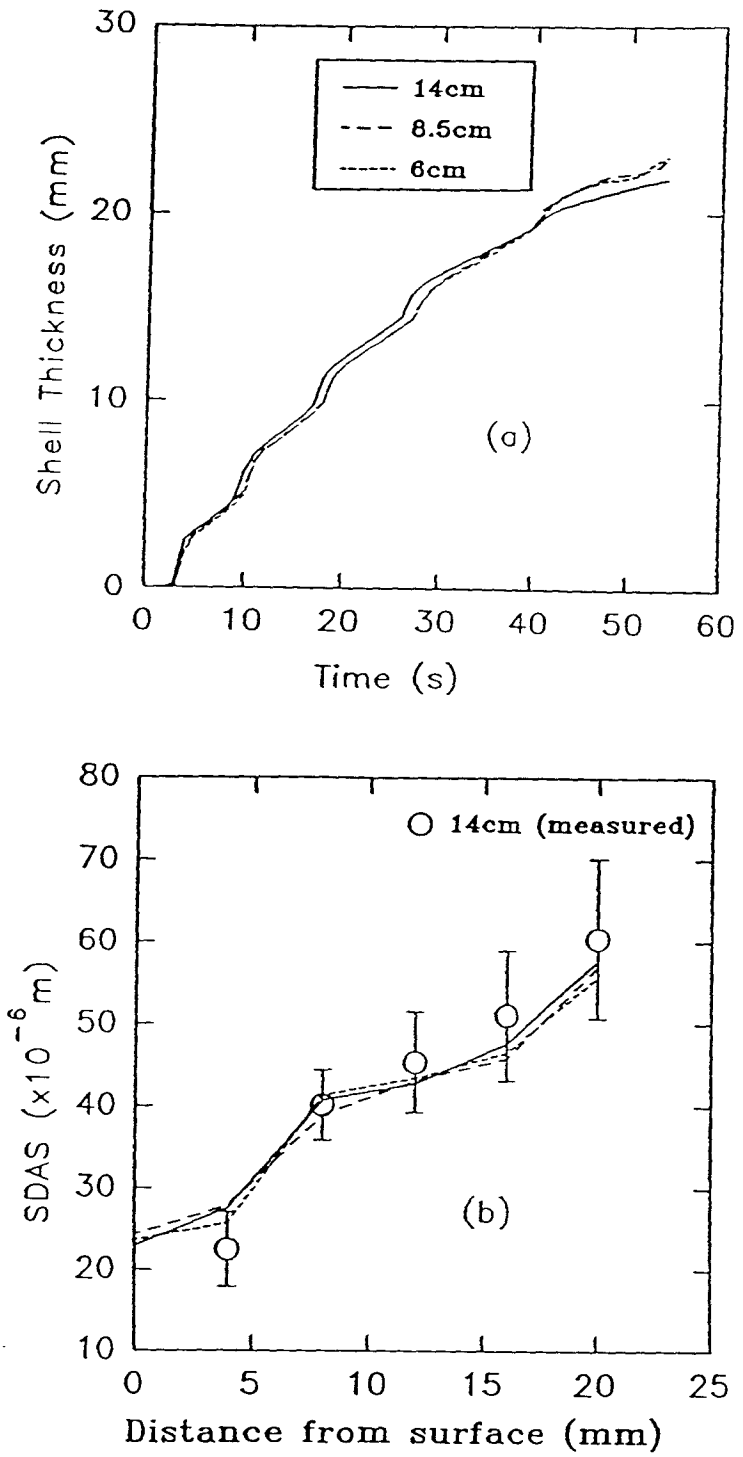

Fig. 6.18 Effect of bath height on solidification and microstructure for Al-7% Si and copper chill (superheat=30°C) - (a) shell thickness (b) secondary dendrite arm spacing.

6.4 Proposed Empirical Model

From these results and the above discussions, it is evident that the interfacial heat flux is dependent on a variety of factors. The individual effects of some of these factors (surface roughness, chill material, superheat, alloy composition, and gap composition) have been highlighted. Following the trend of an earlier analysis by Kumar et al.[49], an attempt was made to develop an empirical interfacial heat flux model to simulate the factors studied. It is envisaged that such a model could provide an estimate of the interfacial heat flux transients that could be utilized for modeling the boundary conditions on the casting side for solidification simulation. The advantage of such a model is that the transient heat flux is estimated purely from the thermophysical properties of the chill and casting.

The model is based on the Al-Si alloys and is divided into three stages as illustrated schematically in Fig. 6.19:

(I) The first stage exhibits a linear relationship between heat flux and time, and covers the period from time zero to the time at which the maximum heat flux is attained. The maximum heat flux can be expressed as follows:

$$q_{\max} = C_0 \left(\frac{T_c}{T_m} \right)^a \left(\frac{\alpha_m}{X_m} \right)^b Ra^c \qquad W/m^2 \qquad (R^2 = 0.99) \qquad (6.4)$$

where $C_0 = 1224\text{-}1988 = 136.50 \times (T_L\text{-}T_S)^{0.6352}$

$a = 1.9344$

$b = 0.0657$

$c = -0.0104$

The flux from onset of contact to the peak value (2 - 5 s in all cases studied) could be estimated by linearizing the flux values from about $0.25q_{max}$ at time zero to q_{max}.

(II) The flux in the intervening period between 10 s and q_{max} could be estimated by linearizing the heat flux values between q_{max} and the q value obtained by Eq. (6.5) for t=10s.

(III) The flux at any time greater than 10 seconds after the q_{max} could be expressed as

$$\frac{q}{q_{\max}} = C_1 \left(\frac{L_m}{L_c} \right)^d \alpha^e t^f \qquad W/m^2 \qquad (R^2 = 0.92) \tag{6.5}$$

where $C_1 = 9.673$

$d = 0.158$

$e = 0.115$

$f = -0.60$

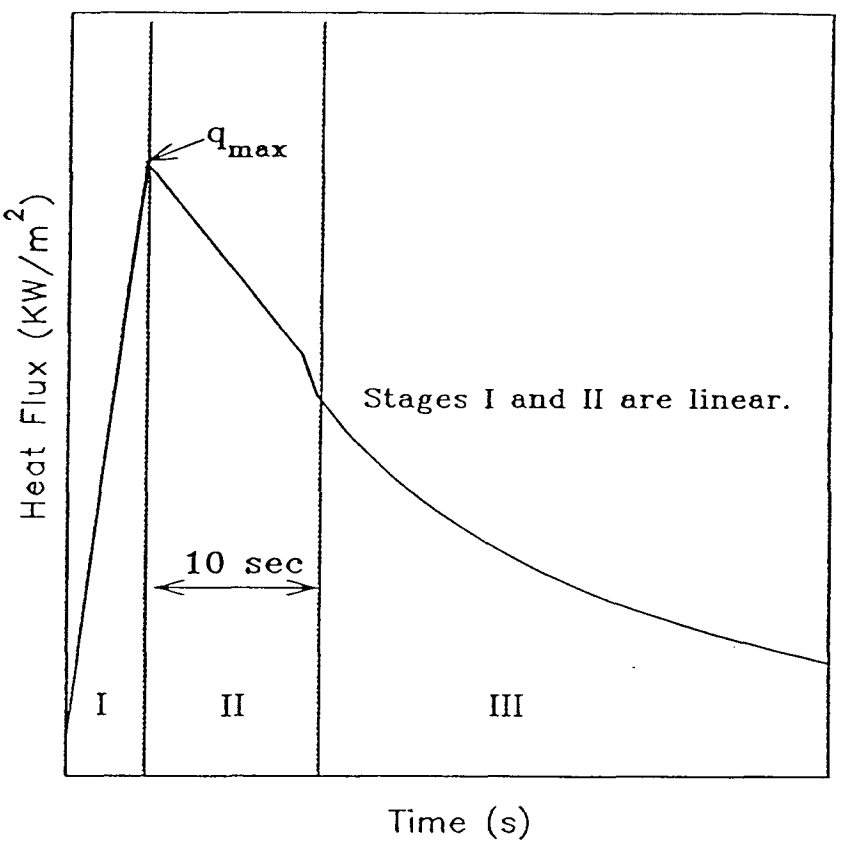

Fig. 6.19 Schematic illustration of the proposed empirical heat flux model.

Figures 6.20 and 6.21 compare the values of the maximum heat flux obtained from Eq. (6.4) with the inverse solution values. Good agreement is observed for all cases considered. A complete simulation based on Eqs. (6.4) and (6.5) is shown in Fig. 6.22 for Al-7% Si. It is observed that the empirical model compares well with the inverse solution. To further test the validity of this model, it was applied to Al-3%Cu-4.5%Si alloy (T_L=627°C, T_S=525°C) under the casting conditions reported by Kumar et al.[49] (T_c=750°C). A value of 1μm was assumed for the surface roughness of the uncoated copper chill. Figure 6.23 depicts the result of this simulation. Good agreement also exists between this model and the results obtained by Kumar et al[42].

Three major factors were not included in Eqs. (6.4) and (6.5) - the latent heat, the thermal diffusivity of the air gap and surface coating/film. It would seem logical to expect the constants, C_0 and C_1, to increase with increasing latent heat of the metal since the latent controls the amount of energy released as a result of solidification. This could not be quantified in the present study due to the fact that all the Al-Si alloys have the same latent heat. The effect of the thermal diffusivity of the gap was demonstrated with the introduction of continuous casting oil films at the surface. The pyrolysis or partial combustion of the oils released gases that enhanced the thermal conductivity of the air gap with a consequent increase in the heat flux. This effect could not be quantified since the actual composition of the released gases is not known. The oil films also demonstrate the effect of surface coating on the heat flux. This could be incorporated into the above expressions in the form of effective diffusivity of the mold. Coatings having a thermal diffusivity smaller than that of the mold material will reduce the effective mold diffusivity and therefore reduce the heat flux value.

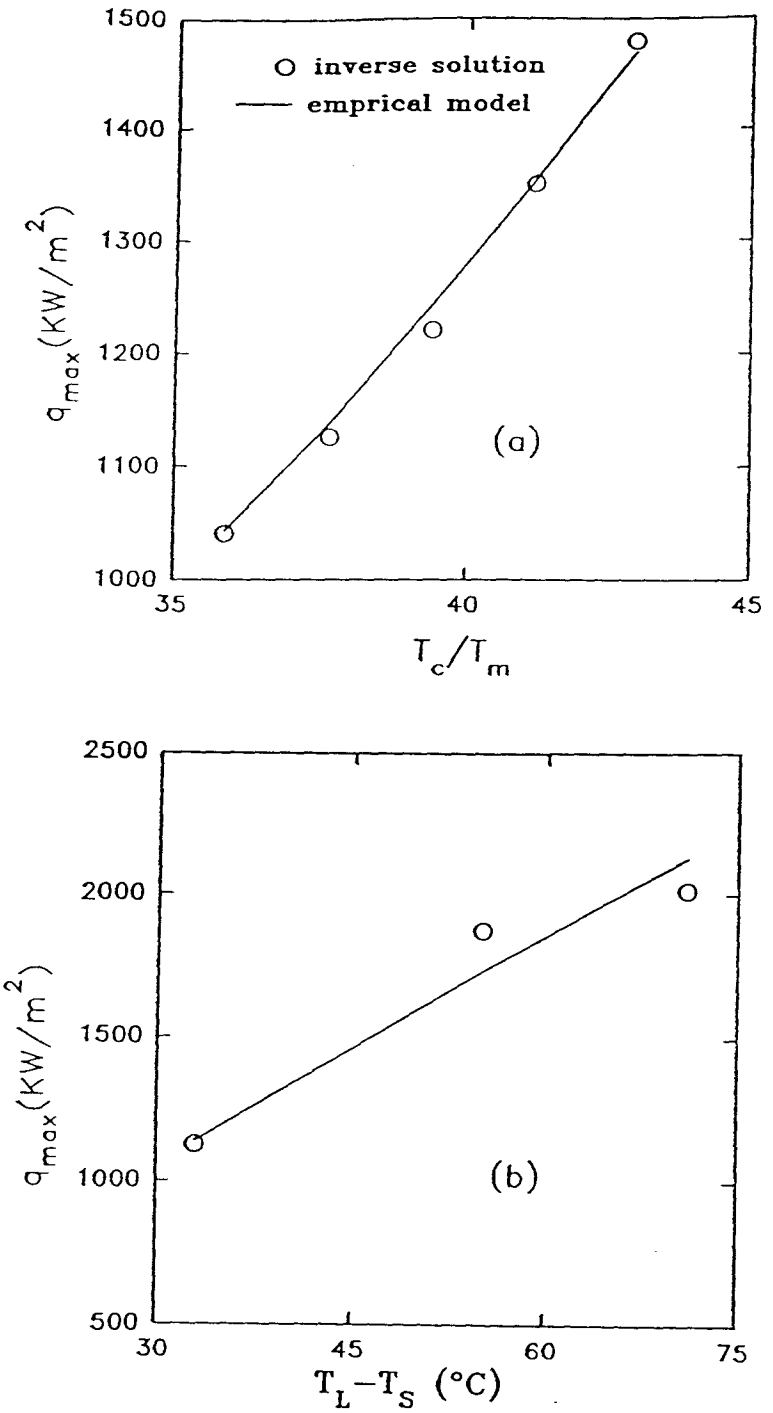

Fig. 6.20 Variation of q_{max} with different process variables - (a) initial temperature ratio of melt and chill, (b) mushy zone.

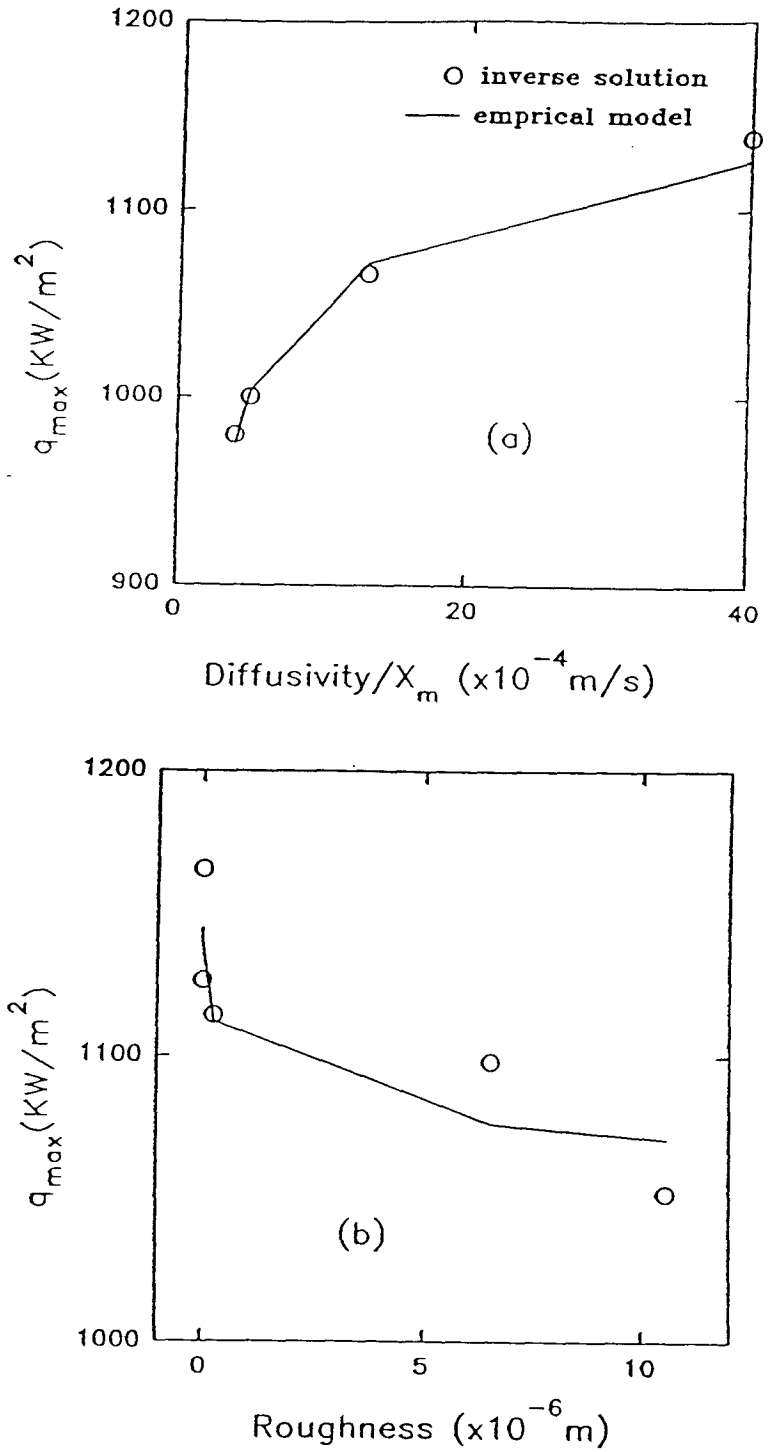

Fig. 6.21 Variation of q_{max} with different process variables - (a) ratio of chill thermal diffusivity to its thickness, (b) chill surface roughness.

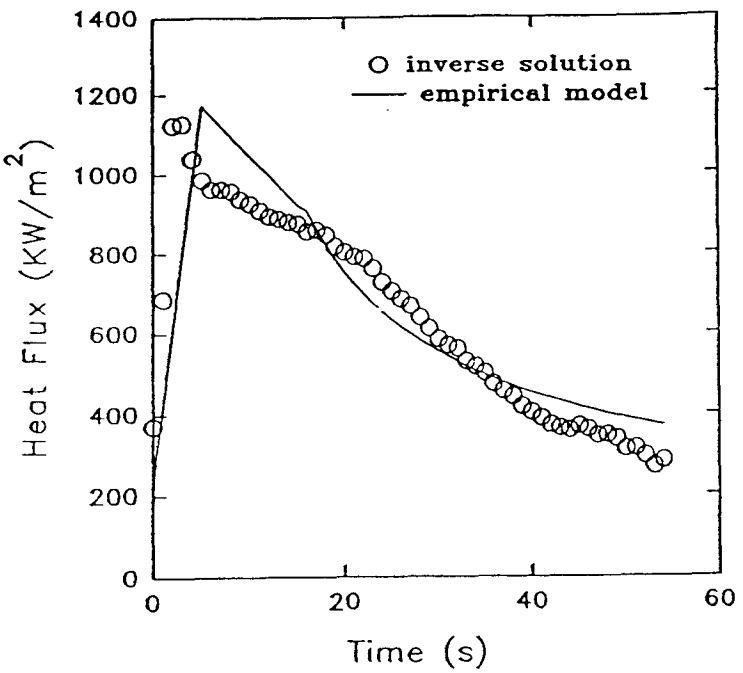

Fig. 6.22 Variation of heat flux with time for Al-7% Si and copper chill (superheat=30°C).

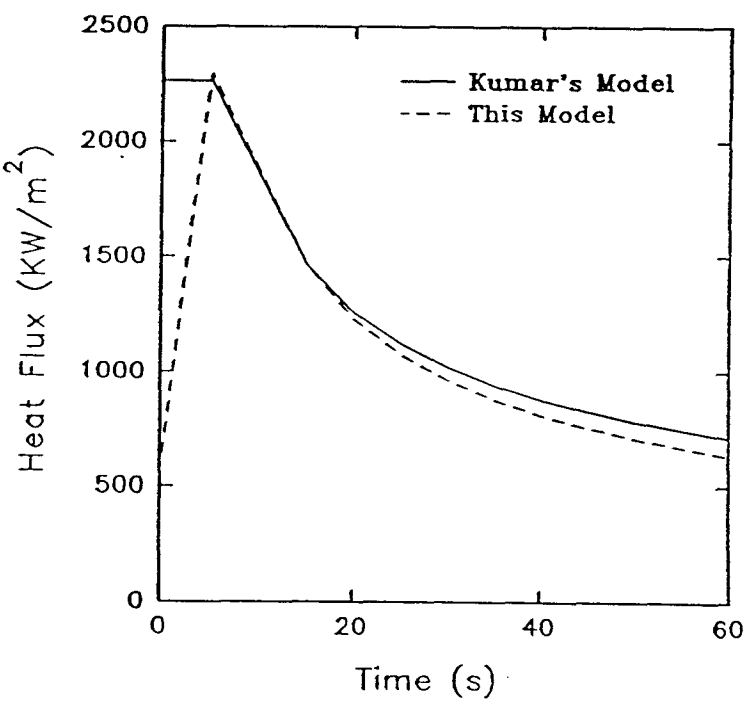

Fig. 6.23 Simulated variation of heat flux with time for Al-3% Cu-4.5% Si (initial casting temperature = 750°C) and a 2.86cm thick copper chill.

6.5 Implications for Continuous and Near-Net-Shape Casting

The interfacial heat flux presented here for Al-Si alloys ranges from 0.97 - 2.0 MW/m^2 while the heat transfer coefficient ranges from 1.95 - 4.30 $KW/m^2.K$. The predicted cooling rate is of the order of 10-100 °C/s at the surface leading to a value of 12-22μm for the secondary dendrite arm spacing very near the surface. These values are comparable to published data on continuous and thin slab casting of aluminium alloys[150,151]. Szczypiorski et al.[150] reported SDAS values of 8-16μm at the surface of a 19mm thick slab cast on a twin-belt Hazelett machine and 18-30μm at the center. The cooling rate and local solidification times calculated here are seen to be in the upper ranges of conventional DC casting and in the lower range of belt/roll casting for alumimium alloys. It is therefore evident that the results obtained here have some implications for continuous and near-net-shape casting processes in general; and the results could be projected to these processes for similar alloy systems.

The observed heat flux transient is typical of any process where initial mold/casting contact is followed by the formation of a clearance gap. It is therefore possible to develop empirical heat extraction models for these processes following the procedure adopted in this study. Of course, the effects of convection in the melt and the relative velocity of casting and mold will have to be included.

It is evident from this study that the biggest variation in interfacial heat transfer occurs in the first few seconds of metal-mold contact (< 45 s). Therefore, the transient nature of interface heat transfer exerts the greatest influence for short dwell times. The implication of this for thin section casting is that the interfacial heat transfer is dynamic throughout the duration of casting. A constant overall boundary condition (h or q) cannot be used in the simulation of the solidification process in this case. This is very relevant for continuous and near-net-shape casting

since the hallmark of these processes is the reduction in section thickness and consequently the shorter dwell times in the heat extraction device. The interfacial heat transfer is controlled by a myriad of factors within this time.

Owing to the lack of directly applicable transient heat transfer data, the heat transfer measurements of Shah et al.[138] for high carbon steel solidifying on a stationary copper chill was employed to estimate the values of the constants in the empirical model in order to apply the model to the prediction of the initial heat transfer transient during twin-roll casting. The results are shown in Fig. 6.24 for a copper roll with a cooling channel located at 50mm below the surface and with the assumption that the steady state value of interfacial heat flux reported in literature[142] corresponds to the attainment of a fairly stable flux after the initial transient. The fact that the interfacial heat flux is inversely proportional to the dwell time[142] was taken into account by adjusting the constant, C_0, in Eq. (6.4). It is observed that the steady state values are about 2-3 times less than the peak flux and are attained after 30-40 seconds of operation.

It has been shown that the mold wall microgeometry as influenced by machining, polishing and coating has a profound influence on the cast structure through heat transfer. Most of the molds used in continuous and near-net-shape casting have fine ground surfaces and in some cases, the surfaces are coated with wear resistance materials. These surfaces are known to have roughness values of 0.2μm to 1μm . This study has shown that further reduction in this range of roughness could be beneficial by increasing the heat extraction rate and further refining of microstructure. It was observed that a reduction of roughness from 0.291μm to 0.018μm could result in a 17% average increase of interfacial heat transfer coefficient. This increment may seem little by itself but for short dwell times and thin sections, it could make the difference between complete solidification and incomplete solidification within the mold. Furthermore, smooth surface finish will be beneficial in reducing the incidence of sticking where this occurs, thereby translating into productivity increase.

In continuous and near-net-shape casting processes, the mold surface could become critical not only in terms of the magnitude but also the distribution across the mold area in contact with the solidifying metal. It has been observed that small local heterogeneity on the microprofile of the roll surface of a single roll caster could lead to local reduction of the solidifying strip thickness by reducing the local heat transfer[152]. Also, complete tearing of the strip surface has been encountered when the roll surface was scratched[152,153]. Perfect replication of the surface microprofile of the roll surface by the cast strip was enhanced by decreasing surface roughness and increasing casting speed[152]. At high values of roll surface roughness, the surface of the cast strip is rough but generally becomes smoother than the roll surface[152] and this observation is similar to the results obtained from this study.

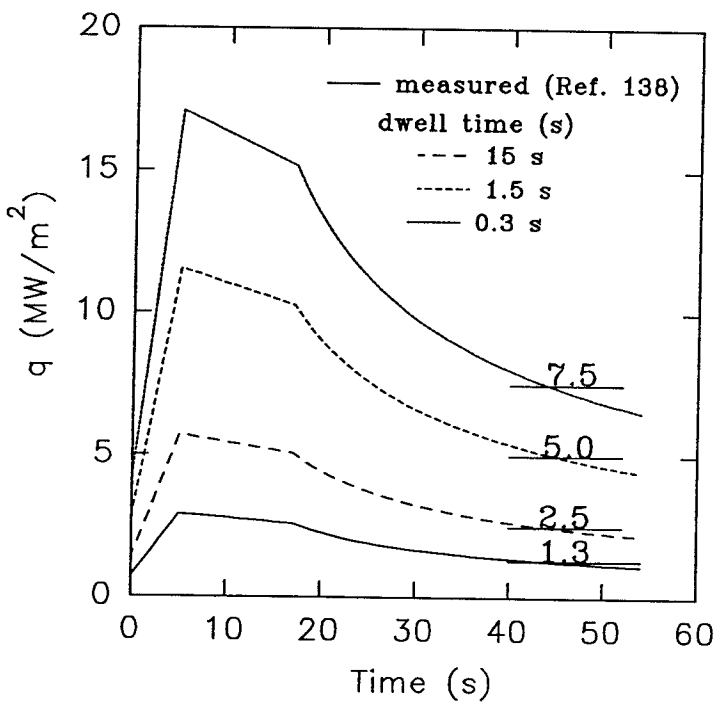

Fig. 6.24 Simulated variation of heat flux with time for high carbon steel (0.8%C) solidifying in a stationary copper chill and in twin-roll caster at various dwell times.

The net effect of surface coating is the decrease in effective thermal diffusivity of the mold since most coating materials have lower conductivity than the mold. The four continuous casting oils investigated in this study increased the heat extraction rate once they attained their flash point by releasing high conductivity gases into the interfacial gap. It is however noted that this effect can only be realized if the oil flow is such that the flash point is reached. A disadvantage of this is the possible increase in gaseous impurities from the casting process. If there is no flashing of oil, the effect of oil lubrication will be similar to surface coating - reduction in interfacial heat transfer.

Four properties of the chill material were shown to affect the interfacial heat extraction - chill thermal diffusivity, thickness, initial temperature and thermal expansion coefficient. Heat extraction increases with increasing thermal diffusivity, decreasing chill thickness and decreasing initial temperature of the chill. Although increasing thermal expansion coefficient may be beneficial by decreasing the air gap size, it is detrimental for thin molds by increasing the tendency towards mold distortion.

The initial effect of cast metal superheat is an increase in heat extraction rate if the mold thermal resistance is small. However, the overall effect will depend on the extent of convection in the melt. With minimal convection in the melt, increasing superheat can accelerate the solidification process but might retard it with increasing convection.

Finally, for thin section castings, the result of this study suggests that a direct relationship could exist between the secondary dendrite arm spacing and the interfacial heat transfer coefficient via the Hills[123] equations. This implies that the effect of the interface is felt at all locations throughout the casting duration.

Chapter 7

SUMMARY AND CONCLUSIONS/RECOMMENDATIONS

A one dimensional implicit finite difference model has been successfully developed to predict heat flow parameters and secondary dendrite arm spacing (SDAS) during unidirectional solidification. The model utilizes the Scheil equation in conjunction with the effective specific heat method to handle the release of the latent heat. Various secondary dendrite arm spacing models were incorporated for the prediction of SDAS. In order to characterize the boundary condition at the mold/casting interface, a dip test was designed and experimental campaigns were carried out by dipping water-cooled cylindrical chills of different materials instrumented with thermocouples into Al-Si melts (3-7%Si). The dip test provided two kinds of measurements:

(a) the thermal histories at thermocouple locations in the chill for about 60 seconds duration

(b) the solidified shell within these short periods

The thermal histories were fed into an inverse heat conduction (IHCP) model for the chill to predict transient interfacial heat flux, chill thermal histories at all locations and also to provide a measure of the variability of the thermocouple readings. The sequential regularization IHCP model developed by Beck[134] was adapted and used for this purpose. The solidified shells were used for metallographic examination and measurement of secondary dendrite arm spacing.

The transient heat flux and chill surface temperature profiles were used as boundary conditions for the casting model. The casting model predicts the interfacial heat transfer coefficient, temperature histories in the casting, cooling rate, local solidification times and secondary dendrite arm spacings. The model is validated with temperature measurements in the casting and the measured secondary dendrite arm spacing. The effects of some process variables

such as chill surface roughness, chill material, superheat, alloy composition, surface film (oil) and bath height were studied. Finally, an attempt was made to provide an empirical transient flux model that will take these variables into account.

From the results of this study the following conclusions can be drawn:

(i) The biggest variation in interfacial heat transfer occurs in the first few seconds of metal-mold contact (< 45 s). The transient nature of interface heat transfer exerts the greatest influence for short dwell times. Therefore, for thin sections castings, the interfacial heat transfer is very dynamic throughout the duration of casting. A constant overall boundary condition (h or q) cannot be used in the simulation of the solidification process in this case.

(ii) The interfacial heat flux, heat transfer coefficient and temperature profiles in the chill exhibit the typical trend common to solidification where the initial contact between mold and melt is followed by the formation of a steadily growing gap. These three parameters increase steeply upon contact up to a certain peak at very short time duration (0-10 s), decrease steeply for a few seconds and then gradually decline to a fairly steady value.

(iii) The peak of the heat flux was found to correspond to the onset of a steadily growing shell and subsequent decrease in heat flux is attributed to the formation of a gap formed as a result of the shell contraction away from the mold which is not balanced by enough mold expansion.

(iv) In general the heat flux increases with increasing mold thermal diffusivity, increasing superheat, increasing thermal diffusivity of the interfacial gap, decreasing mold thickness and initial temperature, and decreasing mold surface roughness. Mold coatings or other surface films such as oil reduce the heat flux at the onset of solidification by acting as an additional thermal barrier since they often have lower thermal diffusivity than the mold. However, any further effect on the heat flux will depend on the nature of the chemical or thermal transformation of

these materials in the presence of heat.

(v) The peak heat flux can be expressed as a power function of the superheat, surface roughness, chill initial temperature and thermal diffusivity of the chill material in the form:

$$q_{\max} = C_0 \left(\frac{T_c}{T_m} \right)^a \left(\frac{\alpha_m}{X_m} \right)^b Ra^c \qquad W/m^2 \qquad (R^2 = 0.99)$$

(vi) It was also found that the heat flux from 10 seconds after the peak can be expressed as power function of time, the chill thermal diffusivity and the ratio of the thermal expansion of the chill to the casting contraction in the form:

$$\frac{q}{q_{\max}} = C_1 \left(\frac{L_m}{L_c} \right)^d \alpha^e t^f \qquad W/m^2 \qquad (R^2 = 0.92)$$

(vii) A three stage heat flux empirical model is proposed. This model could be used as an approximate boundary condition and can easily be evaluated from the knowledge of the thermophysical properties of the mold and casting.

(viii) The secondary dendrite arm spacing depends on the cooling rate and local solidification times in most cases. However at distances very near the surface (<8mm), it could be expressed as a direct function of the heat transfer coefficient and time via the Hills equation.

(ix) Of all the variables investigated, the chill material and alloy composition were found to have the greatest effect on the secondary dendrite arm spacing.

(x) The results of this study have some implications for continuous and near-net-shape casting. It was shown that by allowing for the small thickness of the mold used in these processes, the results presented here fall between the upper range of conventional DC casting of aluminium alloys and lower range of such near-net-shape processes as the twin-belt caster. In these processes, the variables studied here could become critical due to the short dwell times and thin sections

involved.

Finally, it is believed that the objectives of this study have been met substantially. The transient interfacial heat flux has been characterized both numerically and empirically as a function of processing parameters studied. The empirical flux model proposed here has obvious advantages over the earlier model proposed by a Kumar et al.[49] because it incorporates more variables that are known to affect interfacial heat transfer. The secondary dendrite arm spacing has been linked to heat transfer through expressions that utilize the cooling rate, local solidification time and interfacial heat transfer coefficient as variables.

It is recommended that further studies in this direction should include the following:

(1) The effect of latent heat on the interfacial heat flow and microstruture

(2) The effect of convection in the melt on the interfacial heat flux and microstructure

(3) The effect of known air gap composition on heat flux and microstructure.

(4) The time frame of attaining the peak interfacial heat transfer during solidification.

REFERENCES

1. R. Genders: "The Interpretation of Macrostructure of Cast Metals", Journal of Institute of Metals, 1926, Vol. 35, pp.259-265.

2. B. Chalmers: "Principles of Solidification", John Wiley, New York, 1964.

3. J.W. Gibbs: "The Scientific Papers - Vol.1, Thermodynamics", Dover Publications, New York, 1961.

4. K. Ho and R.D. Pehlke: "Mechanisms of Heat Transfer at a Metal-Mold Interface", AFS Trans., 1984, Vol. 92, pp.587-598.

5. M. Rappaz: "Modeling of Microstructure Formation in Solidification Processes", International Materials Reviews, 1989, Vol. 34, No. 3, pp.93-123.

6. D.G.R. Sharma and M.Krishnan: "Simulation of Heat Transfer at Casting Metal-Mold Interface", AFS Trans., 1991, Vol. 99, pp.429-438.

7. I. Minkoff: "Solidification and the Cast Structure", John Wiley & Sons Publishers, 1986, pp.7-12.

8. W. Kurz and R. Trivedi: "Recent Advances in Modeling of Solidification Microstructures", Proc. of International Conference on Solidifcation and Casting, The Metals Soceity, London, 1987, pp.1-12.

9. V. Laxmanan: "Dendritic Solidicfication - Part I. Analysis of Current Theories Theories and Models, Part 2. A Model for Dendritic Growth Under an Imposed Thermal Gradient", Acta Metall., 1985, Vol. 33, No. 6, pp.1023-1049.

10. T.Z. Kattamis and M.C. Flemings: "Dendrite Structure and Grain Size of Undercooled Melts", Trans. AIME, 1966, Vol. 236, pp.1523-1532.

11. M.C. Flemings and T.Z. Kattamis: "Dendrite Arm Spacing in Aluminum Alloys", AFS Trans., 1991, Vol. 99, pp.501-506.

12. R.E. Spear and G.R. Gardner: "Dendrite Cell Size ", AFS Trans., 1963, Vol. 71, pp.209-215.

13. K.J. Oswalt and M.S. Misra: "Dendrite Arm Spacing (DAS: A Nondestructive Test to Evaluate Tensile Properties of Premium Quality Aluminum Alloy (Al-Si-Mg) Castings", AFS Trans., 1980, Vol. 88, pp.845-862.

14. B.G. Mellor and G.A. Chadwick: "Structure and Mechanical Properties of Unidirectionally Solidified Low Alloy Steels", Materials Science and Technology, November 1988, Vol. 4, pp.991-999.

15. D.R. Poirier, M.L. Ebner, M.C. Flemings and W.A. Backoften: "Effect of Processing History on Fracture of Materials at High Strength Levels", Report Number ASD-TDR-63-819, Part 1, M.I.T, Sept. 1963.

16. S. Shivkumar, D. Apelian and J. Zou: "Modeling of Microstructure Evolution and Microporosity Formation in Cast Aluminum Alloys", AFS Trans., 1990, Vol. 98, pp.897-904.

17. C. Yoshida, K. Taniguchi, T. Nakagawa, M. Sudo and T. Nozaki: "Charateristics of Rapidly Solidified Cast Iron and High Carbon Steels", ISS Steelmaking Proceedings, 1986, Vol. 69, pp.855-859.

18. Y.V. Murty, T.Z. Kattamis and O.F. Devereux: "The Effect of Solidification Microstructure on the Corrosion Behavior of a Columnar Aluminum-Copper Alloy", Metall. Trans., 1973, Vol. 4, pp.2575-2580.

19. S.M. Skolianos, T.Z. Kattamis and O.F. Devereux: "Microstructure and Corrosion Behavior of As-Cast and Heat Treated Al-4.5 Wt Pct Cu-2.0 Wt Pct Mn Alloys", Metall. Trans. A, 1989, Vol. 20A, pp.2499-2516.

20. M.C.Flemings: "Process Modeling" Proc. Modeling of Casting and Welding Processes, 1981, pp.533-548.

21. J.K. Brimacombe: "The Extractive Metallurgist in an Emerging World of Materials", Metall. Trans. B, 1989, Vol. 20B, pp.291-313.

22. D.M. Stefanescu, G. Upadhya and D. Bandyopadyay: "Heat Transfer-Solidification Kinetics Modeling of Solidification of Castings", Metall. Trans. A, 1990, Vol. 21A, pp.997-1005.

23. D.R. Croft and D.G. Lilley: "Heat Transfer Calculations Using Finite Difference Equations", Applied Science, London, 1977.

24. B. Carnahan, H.A. Luther and J.O. Wilkes: "Applied Numerical Methods", John Wiley, New York, 1969.

25. J.N. Reddy: "An Introduction to the Finite Element Method", McGraw-Hill, New York, 1985.

26. C.A. Brebbia: "The Boundary Element Method for Engineers", Pentech Press, London, 1978.

27. S.V. Patankar: "Numerical Heat Transfer and Fluid Flow", Hemisphere Publishing, New York, 1980.

28. I. Ohnaka: "Introduction to Analysis of Heat Transfer and Solidification by Computer - Application for Casting Process", Maruzem, Tokyo, 1985.

29. K. Ho and R.D. Pehlke: "Transient Methods for Determination of Metal-Mold Interfacial Heat Transfer", AFS Trans., 1983, Vol. 91, pp.689-698.

30. J.V. Beck , B. Blackwell and C.R. St. Clair, Jr.: "Inverse Heat Conduction : Ill Posed Problems", Wiley-Interscience, New York, 1985, pp.1-15.

31. D.R. Durham and J.T.Berry: "Role of the Mold-Metal Interface During Solidification of a Pure Metal Against a Chill", AFS Trans., 1974, Vol. 82, pp.101.

32. D.R. Durham, D. Verma and J.T. Berry: "Some Further Observations on Freezing from Chills", AFS Trans., 1976, Vol. 84, p.76.

33. M. Prates, J. Fissolo and H. Billoni: "Heat Flow Parameters Affecting the Unidirectional Solidification of Pure Metals", Metall. Trans. A, 1972, Vol. 3A, pp.1419.

34. W.A. Tiller: "Grain Size Control During Ingot Solidification - Part II: Columnar-Equiaxed Transition", Trans. AIME, 1962, Vol. 224, pp.448-459.

35. R.C. Sun: "Simulation and Study of Surface Conductance for Heat Flow in the early Stages of Casting", AFS Cast Metals Research Journal, 1970, , Vol. 6, pp.105-110.

36. A.C. Rapier, T.M. Jones and J.E. McIntosh: "The Thermal Conductance of Uranium Dioxide/Stainless Steel Interface", Int. Journal of Heat and Mass Transfer, 1963, Vol. 6, pp.397-416.

37. M. Prates and H. Billoni: "Variables Affecting the Nature of the Chill Zone", Metall. Trans. A, 1972, Vol. 3A, pp.1501-1508.

38. S.A. Levy, S. Lipson and H. Rosenthal: "Influence of a Locking Chill on Solidification Time and Dendrite Arm Spacing of Cast 7075 Aluminum Alloy", AFS Cast Metals Research Journal, 1969, Vol. 5, pp.9-13.

39. L.D.J. Sully: "The Thermal Interface between Castings and Chill Molds", AFS Trans., 1976, Vol. 84, pp.735-744.

40. Y. Nishida and H. Matsubara: "Effect of Pressure on Heat Transfer at the Metal-Mold Casting Interface", British Foundrymen, 1976, Vol. 69, pp.274-278.

41. R.S. Sayles and T.R. Thomas: "Thermal Conductance of a Rough Elastic Contact", Applied Energy, 1976, Vol. 2, pp.249-267.

42. A. Morales, M.E. Glicksman and H. Biloni: "Influence of Mold Wall Microgeometry on Casting Structure", Proc. of International Conference on Solidifcation and Casting, The Metals Soceity, London, 1979, pp.184-192.

43. E.S. Tillman and J.T. Berry: "Influence of Thermal Contact Resistance on the Solidification Rate of Long Freezing Range Alloys", AFS Cast Metals Research Journal, 1972, Vol. 8, pp.1-6.

44. R.D. Pehlke, J.T. Berry, W. Erickson and C.H. Jacobs: "Simulation of Shaped Casting Solidification" Proc. of International Conference on Solidifcation and Casting, The Metals Soceity, London, 1979, pp.371-379.

45. T. Suzuki, Y. Miyata, H. Sakuta and M. Ohta: "Measurement of Heat Transfer Coefficient between Melt and Chill", ISIJ, 1987, Vol. 73, pp.289-296.

46. H. Jacobi: "Influence of Different Gas Atmospheres in the Gap in the Heat Transfer between Ingot and Water Cooled Mold", Arch. Eisenhuttenwes, 1976, Vol. 47, No. 6, p.441.

47. K. Ho and R.D. Pehlke: "Metal-Mold Interfacial Heat Transfer", Metall. Trans., 1985, Vol. 16B, pp.585-594.

48. J.V. Beck: "Nonlinear Estimation Applied to the Nonlinear Inverse Heat Conduction Problem", Int. Journal of Heat and Mass Transfer, 1970, Vol. 13, pp.703-716.

49. T.S. Prasanna Kumar and K. Narayan Prabhu: "Heat Flux Transients at the Casting/Chill Interface during Solidification of Aluminum Base Alloys', Metall. Trans. B, 1991, Vol. 22B, pp.717-727.

50. M. Bamberger, B.Z. Weiss and M.M. Stupel: "Heat Flow and Dendritic Arm Spacing in Chill-Cast Al-Si Alloys", Material Science and Technology, 1987, Vol. 3, pp.49-56.

51. G.H. Meyer: "An Application of the Method of Lines to Multi-Dimensional Free Boundary Problems", J. Inst. Maths Applications, 1977, Vol. 20, pp.317-329.

52. A. Lazaridis: "A Numerical Solution of the Multi-dimensional Solidification (or Melting) Problem", Int. J. Heat Mass Transfer , 1975, Vol. 13, pp.1459-1477.

53. J.L. Duda, M.F. Malone, R.H. Notter and J.S. Vrentas: "Analysis of Two-Dimensional Diffusion-Controlled Moving Boundary Problems", Int. J. Heat Mass Transfer, 1975, Vol. 18, pp.901-910.

54. D.R. Lynch and K. O'Neil: "Continuously Deforming Finite Elements for the Solution of Parabolic Problems, With or Without Phase Change", Int. J. Numerical Methods and Engineering, 1981, Vol. 17, pp.81-96.

55. D.R. Lynch: "Unified Approach to simulation on Deforming Elements With Application to Phase Change Problems", Journal of Computational Physics, 1982, Vol. 47, No. 3, pp.387-411.

56. D. Poirier and M. Salcudean: " On Numerical Methods Used in Mathematical Modeling of Phase Change in Liquid Metals", Journal of Heat Transfer, 1988, Vol. 110, pp.562-570.

57. G.M. Dusinberre: "Numerical Methods for Transient Heat Flows", Trans. ASME, 1945, Vol. 67, p.703.

58. P.C. Doherty: "Hot Pipe", U.S. Geological Survey Computer Contribution, No. 4, 1970.

59. M. Salcudean and Z. Abdullah: "Numerical Simulation of Casting Processes", Proceedings of the 8th Int. Heat Transfer Conference and Exhibition, San Francisco, CA, August, 1986, pp.459-464.

60. W.D. Rolph and D. Bathe: "An Efficient Algorithm for Analysis of Nonlinear Heat Transfer With Phase Changes", Int. J. Numerical Methods and Engineering, 1982, Vol. 18, pp.119-134.

61. H.T. Hashemi and C.M. Sliepcevich: "A Numerical Method for Solving Two-Dimensional Problems of Heat Conduction with Change of Phase", Chem. Eng. Prog. Symp. Series, 1967, Vol. 63, No. 79, pp.34-41.

62. G. Comini, S. Del Guidice, R.W. Lewis and O.C. Zienkiewicz: "Finite Element Solution of Non-linear Heat Conduction Problems With Special Reference to Phase Change", Int. J. Numerical Methods and Engineering, 1974, Vol. 8, pp.613-624.

63. G.H. Meyer: "Multi-dimensional Stefan Problems", SIAM J. Numerical Analysis, 1973, Vol. 10, No. 3, pp.522-538.

64. N. Shamsunder and E.M. Sparrow: "Analysis of Multi-dimensional Conduction Phase Change Via the Enthalpy Model", ASME Journal of Heat Transfer, 1975, Vol. 97, pp.333-340.

65. J.W. Jerome: "Nonlinear Equations of Evolution and a Generalized Stefan Problem", Journal of Diff. Eq., 1977, Vol. 26, pp.240-261.

66. A.B. Crowley: "Numerical Solution of Stefan Problems", Int. J. Heat Mass Transfer, 1978, Vol. 21, pp.215-219.

67. G.E. Bell and A.S. Wood: "On Perfomance of the Enthalpy Method in the Region of a Singularity", International J. Num. Methods and Engineering, 1983, Vol. 19, pp.1583-1592.

68. K.H. Tacke: "Discretization of Explicit Enthalpy Method for Planar Phase Change", International J. Num. Methods and Engineering, 1985, Vol. 21, pp.543-554.

69. Q.T. Pham: "A Fast Unconditionally Stable Finite-Difference Scheme for Heat Conduction With Phase Change", Int. J. Heat Mass Transfer, 1985, Vol. 28, No. 11, pp.2079-2084.

70. C.H. Su and H.L. Tsai: "A Direct Method to Include Latent Heat Effect for Modeling Casting Solidification", AFS Trans., 1991, Vol. 99, pp.781-789.

71. K. Morgan: In "Computing Methods in Applied Sciences and Engineering", 1981, No. 28, p.275.

72. D.K. Gartling: In 'Computer Methods in Fluids' (ed. by K. Morgan et al.), Pentech, London, 1980, p.257.

73. W.D. Bennon and F.P. Incropera: "A Continuum Model for Momentum, Heat and Species Transport in Binary Solid-Liquid Phase Systems - I II. Application to Solidification in a Rectangular Cavity", Int. J. Heat Mass Transfer, 1987, Vol. 30, pp.2161-2187.

74. V.R. Voller and C. Prakash: "A Fixed Grid Numerical Modeling Methodology for Convection-Diffusion Mushy Region Phase-Change Problems", Int. J. Heat Mass Transfer, 1987, Vol. 30, pp.1709-1719.

75. Ph. Thevoz, J.L. Desbiolles and M. Rappaz: "Modeling of Equiaxed Microstructure Formation in Casting", Metall. Trans. A, 1989, Vol. 20A, pp.311-322.

76. A. Ohno: "Solidification - The Separation Theory and its Practical Applications", Springer-Verlag Publishers Berlin, 1987, pp.113-118.

77 M. Volmer and A. Weber: In Reference 7, p.9

78. J.D. Hunt: "Steady Sate Columnar and Equiaxed Growth of Dendrites and Eutectics", Material Science and Engineering, ASM, 1984, Vol. 65, pp.75-83.

79. W. Oldfield: "Computer Model Studies of Dendritic Growth", ASM Material Science and Engineering, 1973, Vol. 11, pp.211-218.

80. M.E. Glicksman and R.J. Schaeffer: "In Situ Measurements of Dendrite Profiles in Pure Tin", Acta Metall., 1966, Vol. 14, pp.1126-1129.

81. R.J. Schaeffer and M.E. Glicksman: "Direct Observation of Dendrite Remelting in Metal Alloys", Trans. AIME, 1967, Vol. 239, pp.257-260.

82. S. O'Hara: "Controlled Growth of Tin Dendrites", Acta Metall., 1967, Vol. 15, pp.231-236.

83. D.R. Hamilton and R.G. Seidensticker: "Growth Mechanism s of Germanium Dendrites: Kinetics and the Nonisothermal Interface", Journal of Applied Physics, 1963, Vol. 36, pp.1450-1460.

84. M.E. Glicksman and R.J. Schaeffer: In "The Solidification of Metals", Iron and Steel Institute, 1968, Publ. No. 110, p.43.

85. M.E. Glicksman and R.J. Schaeffer: "Investigation of Solid-Liquid Interface Temperatures Via Isenthalpic Solidification", Journal of crystal Growth, 1967, Vol. 1, pp.297-310.

86. M.E. Glicksman, R.J. Schaeffer and J.D. Ayers: "Dendritic Growth - A Test of Theory", Metall. Trans. A, 1976, Vol.7A, pp.1747-1759.

87. S.C. Huang and M. E. Glicksman: "Fundamentals of Dendritic Solidification - I. Steady-State Tip Growth, II. Development of Sidebranch Structure", Acta Metall., 1981, Vol. 29, pp.701-734.

88. M.E. Glicksman, N.B. Singh and M. Chopra: In "Materials Processing in Reduced Gravity Environment of Space (Edited by G.E. Rindone)", MRS Symposium, Elsevier, Amsterdam, 1982, Vol. 9, pp.461-478.

89. M.H. Burden and J.D. Hunt: "Cellular and Dendritic Growth", Journal of Crystal Growth, 1974, Vol. 22, pp.99-116.

90. R. Trivedi: "Theory of Dendritic Growth During the Directional Solid of Binary Alloys", Journal of Crystal Growth, 1980, Vol. 49, pp.219-232.

91. K. Shibata, T. Sato and G. Ohira: "Morphorlogical Stabilities of Planar Solid-Liquid Interfaces During Unidirectional Solidification of Dilute Al-Ti and Al-Cr Alloys", Journal of Crystal Growth, 1978, Vol. 44, pp.419-434.

92. G.R. Kotler, K.W. Casey and G.S. Cole: "Experimental Observations of Dendritic Growth", Metall. Trans. A, 1972, Vol. 3A, pp.723-726.

93. P.K. Rohatgi and C.M. Adams Jr.: "Dendritic Solidification of Aluminum-Copper Alloys", Trans. AIME, 1967, Vol. 239, pp.1739-1746.

94. T.F. Bower, H.D. Brody and M.C. Flemings: "Measurements of Solute Redistribution in Dendritic Solidification", Trans. AIME, 1966, Vol. 236, pp.624-634.

95. H.D. Brody and M.C. Flemings: "Solute Redistribution in Dendritic Solidification", Trans. AIME, 1966, Vol. 236, pp.615-624.

96. T.Z. Kattamis, J. Coughlin and M.C. Flemings: "Influence of Coarsening on Dendrite Arm Spacing of Aluminum-Copper Alloys", Trans. AIME, 1967, Vol. 239, pp.1504-1511.

97. J.S. Langer, R.F. Sekerka and T. Fujioka: "Evidence of a Universal Law of Dendrite Growth Rates", Journal of Crystal Growth, 1978, Vol. 44, pp.414-418.

98. C. Zener: Trans. AIME, 1946, Vol. 167, p.550.

99. J.W. Rutters and B. Chalmers: "A Prismatic Substructure Formed During Solidification of Metals", Canadian Journal of Physics, 1953, Vol. 31, pp.15-39.

100. W.W. Mullins and R.F. Sekerka: "Stability of a Planar Interface During Solidification of a Dilute Binary Alloy", Journal of Applied Physics, 1964, Vol. 35, pp.444-451.

101. M. Hillert: "Diffusion and Interface Control of Reactions in Alloys", Metall. Trans. A, 1975, Vol. 6A, pp.5-19.

102. G.P. Ivantsov: In Reference 7, p.22.

103. R. Trivedi: "Growth of Dendritic Needles from a Supercooled Melt", Acta Metall., 1970, Vol. 18, pp.287-296.

104. G. Horvay and J.W. Cahn: "Dendritic and Spheroidal Growth", Acta Metall., 1961, Vol. 9, pp.695-705.

105. J.S. Langer and H. Muller-Krumbhaar: "Theory of Dendritic Growth: I. Element of a Stability Analysis, II. Instabilities in the Limit of Vanishing Surface Tension, III. Effect of Surface Tension", Acta Metall., 1978, Vol. 26, pp.1681-1708.

106. H. Jacobi and K. Schwerdtfeger: "Dendritic Morphology of Steady State Unidirectionally Solidified Steel", Metall. Trans. A, 1976, Vol. 7A, pp.811-820.

107. K.P. Young and D.H. Kirkwood: "The Dendrite Arm Spacings of Aluminum-Copper Alloys Solidified Under Steady-State Conditions", Metall. Trans. A, 1975, Vol. 6A, pp.197-205.

108. J.A. Spittle and D.M. Lloyd: "Dendrite Arm Spacings in Hypoeutectic Pb-Sb Alloys Directionally Solidified Under Steady and Non-Steady Conditions", Proc. of International Conference on Solidifcation and Casting, The Metals Soceity, London, 1979, pp.15-20.

109. R. Trivedi: "Interdendritic Spacing : Part II. A Comparison of Theory and Experiment", Metall. Trans. A, 1984, Vol. 15A, pp.977-982.

110. J.D. Hunt: "Cellular and Primary Dendrite Spacings", Proc. of International Conference on Solidifcation and Casting, The Metals Soceity, London, 1979, pp.3-9.

111. W. Kurz and D.J. Fisher: "Dendritic Growth at the Limit of Stability : Tip Radius and Spacing", Acta. Metall., 1981, Vol. 29, pp.11-20.

112. G.Y. An and L.X. Liu: "Dendrite Sapcing in Undirectionally Solidified Al-Cu Alloy", Journal of Crystal, 1987, Vol. 80, pp.383-392.

113. P.E. Brown and C.M. Adams: "Rapidly Solidified Alloy Structures", Trans. AFS, 1961, Vol. 69, pp.879-891.

114. A.B. Michael and M.B. Bever: Trans. AIME, 1954, Vol. 200, pp.47-56.

115. J.A. Howarth and L.F. Mondolfo: "Dendritic Growth", Acta Metall., 1962, Vol. 10, No. 6, pp.1037-1042.

116. U. Fuerer and R. Wunderlin: "Einfluss der Zusammensetzung und der Erstarrungsbedingungen auf die Dendritenmorphologie binarer Al-Legierungen", Fabchbericht der Deutschen Gesellschaft fur Metallkunde, Oberursel, 1977.

117. D.H. Kirkwood: "A Simple Model for Dendritte Arm Coarsening during Solidification", Material Science and Engineering, 1985, Vol. 73, pp.L1-L4.

118. A. Mortensen: "On the rate of Dendrite Arm Coarsening", Metall. Trans. A, 1991, Vol. 22A, pp.569-574.

119. P.W. Voorhees: "Coarsening in Binary Solid-Liquid Mixtures", Metall. Trans. A, 1990, Vol. 21A, pp.27-37.

120. M. Wolf and W. Kurz: "Solidification of Steel in Continuous Casting Molds", Proc. of International Conference on Solidifcation and Casting, The Metals Soceity, London, 1979, pp.75-83.

121. J. Szekely and J. Themelis: "Rate Phenomena in Process Metallurgy", Wiley Publishers, New York, 1971.

122. L.F. Shiau, W.G. Lo and A.W. Cramb: "Secondary Dendrite Arm Spacing in Stainless Steel Castings", Iron and Steelmaker, June 1991, pp.57-62.

123. A.W.D. Hills: "Microstructural Engineering of Near-Net-Shape Casting", Proc. 1st European Conf. on Advanced Materials and Processes, 1989, pp.75-86.

124. E.Z. Scheil: In "Zeitschrift fur Metallkunde", 1942, Vol. 34, p.70.

125. T.W. Clyne and W. Kurz: "Solute Redistribution During Solidification with Rapid Solid State Diffusion", Metall. Trans. A, 1981, Vol. 12A, pp.965-971.

126. S.C. Flood and J.D. Hunt: "Columnar and Equiaxed Growth: I. A Model of a Columnar Front with a Temperature Dependent Velocity, II. Equiaxed Growth Ahead of a Columnar Front", Journal of Crystal Growth, 1987, Vol. 82, pp.543-560.

127. M. Solari and H. Biloni: "Microsegregation in Cellular Dendritic Growth", Journal of Crystal Growth, 1980, Vol. 49, pp.451-457.

128. W. Kurz, B. Giovanola and R. Trivedi: "Theory of Microstructural Development During Rapid Solidification", Acta Metall., 1986, Vol. 34, No. 5, pp.823-830.

129. M. Rappaz and Ph. Thevoz: "Solute Diffusion Model for Equiaxed Dendritic Growth", Acta Metall., 1987, Vol. 35, No. 7, pp.1487-1497.

130. M. Rappaz and Ph. Thevoz: "Solute Diffusion Model for Equiaxed Dendritic Growth: Analytical Solution", Acta Metall., 1987, Vol. 35, No. 7, pp.2929-2933.

131. The Temperature Handbook, Omega Engineering Inc., 1989, pp.Z45-Z51.

132. Talysurf 5 System, Operator's Handbook, Rank Taylor Hobson, England, 1981.

133. J.V. Beck, B. Litkouhi and C.R. St. Clair, Jr.: "Efficient Sequential Solution of the Nonlinear Inverse Heat Conduction Problem", Numerical Heat Transfer, 1982, Vol. 5, 1982, pp.275-286.

134. J.V. Beck: "Users Manual for CONTA - Program for Calculating Surfaee Heat Fluxes from Transient Temperatures inside Solids", Michigan State University, SAN83-7134.

135. J.P. Holman: "Heat Transfer", McGraw Hill, 1981, pp.536-537.

136. "Metals Handbook", ASM, 1990, Vol. 2, pp.152-177.

137. B.G. Thomas, I.V. Samarasekera and J.K. Brimacombe: "Mathematical Model of the Thermal Processing of Steel Ingots: Part I. Heat Flow Model", Metall. Trans. B, 1987, Vol. 18B, pp.119-130

138. N.A. Shah and J.J. Moore: "Effect of Thermal Conditions and Alloying Constituents (Ni, Cr) on Macrosegregation in Continuously Cast High-Carbon Low Alloy Steel", Metall. Trans. B, 1989, Vol. 20B, pp.893-910.

139. H. Biloni and B. Chalmers: "Predendritic Solidification", Trans. AIME, 1965, Vol. 233, pp.373-379.

140. C.M. Adams: "Thermal Considerations in Freezing", Liquid Metals and Solidification, American Society for Metals, 1958, pp.187-217.

141. G.H. Geiger and D.R. Poirier: "Solidification Heat Transfer", Transport Phenomena in Metallurgy, Addison Wesley Publishing Co., 1980, pp.329-349.

142. J.K. Brimacombe and I.V. Samarasekera: "Fundamental Aspects of the Continuous Casting of Near-Net-Shape Steel Products", Proc. Of TMS Conference on Casting of Near-Net-Shape Products, 1988, pp.3-24.

143. D.J. Hurtuk and A.A. Tzavaras: "Aberrations Observed in Relationship of Dendrite Size-Alloying Elements for Low-Alloy Steel", Proc. of International Conference on Solidifcation and Casting, The Metals Soceity, London, 1979, pp.21-28.

144. T.W. Caldwell, A.J. Campagna, M.C. Flemings and R. Mehrabian: "Refinement of Dendrite Arm Spacing in Aluminum Ingots Through Heat Flow Control", Metall. Trans. B, 1977, Vol. 8B, pp.261-270.

145. P.C. Dann, J.A. Eady and L.M. Hogan: "Dendrite Arm Spacing in Aluminium-Rich Alloys", Journal of Australian Institute of Metals, 1974, Vol. 19, pp.140-147.

146. B. Alexander and F. Rhines: Trans. AIME, 1950, Vol.188, p.1267.

147. R.N. Grugel: "Secondary and Tertiary Dendrite Arm Spacing Relationships in Directinally Solidified Al-Si Alloys", Journal of Materials Science, 1993, Vol. 28, pp.677-683.

148. D.J. Allen and J.D. Hunt: "Diffusion in the Semi-Solid Region During Dendritic", Metall. Trans. A, 1979, Vol. 10A, pp.1389-1397.

149. R.J. Fessenden and J.S. Fessenden: "Organic Chemistry", PWS Publishers, Boston, 1982, pp.230-234, 887-890.

150. W. Szczypiorski and R. Szczypiorski: "The Mechanical an Metallurgical Charateristics of Twin-Belt Cast Al-Strip Using Current Hazellet Technology", TMS Light Metals, 1991, pp.805-814.

151. B. Frischknecht and K.P. Maiwald: "Roll Caster Applications and Developments", TMS Light Metals, 1988, pp.365-372.

152. J.P. Birat, P. Blin, J.L. Jacquot, P. Riboud and B. Thomas: "Near Net Shape Continuous Casting of Flat Products at IRSID", La Revue de Metallurgie - CIT, 1989, pp.919-930.

153. P. Cremer and J. Bigot: "An Infrared Thermographic Study of the Temperature Variation of an Armophous Ribbon During Production by Planar Flow Casting", Material Science and Engineering, 1988, Vol. 98, pp.95-97.

APPENDIX A

SEQUENTIAL IHCP SOLUTION

In chill casting as in many dynamic heat transfer situations, the heat transfer parameters at the surface (heat flux, heat transfer coefficient and temperature history) are easier to determine from transient measurements at one or more interior locations. Such problems are classified as *inverse heat conduction problems (IHCP).* When the thermophysical properties of the material (density, thermal conductivity and heat capacity) are dependent on temperature, the IHCP is said to be *non-linear.* In most practical IHCP situations, the solution does not satisfy the conditions of uniqueness and stability such that the IHCP is said to be *ill-posed.* This implies that there are infinite number of possible solutions producing almost similar results, and a solution is only accepted by setting limits or defining boundaries.

The various solution techniques currently available for IHCP are shown in Fig. 1A. The discrete value specification method attempts to match predicted and measured temperatures as close as possible with the assumption that all input variables are errorless. On the other hand, the solution stabilization techniques attempts to reduce excessive fluctuations in the solution, thereby stabilizing it.

The method adopted here is the sequential regularization method of Beck[133,134]. It utilizes a *regularizing operator* referred to as the *sensitivity coefficient (SC).* This is defined as the first derivative of the a dependent variable such as temperature, with respect to the unknown parameter of interest (heat flux or heat transfer coefficient).

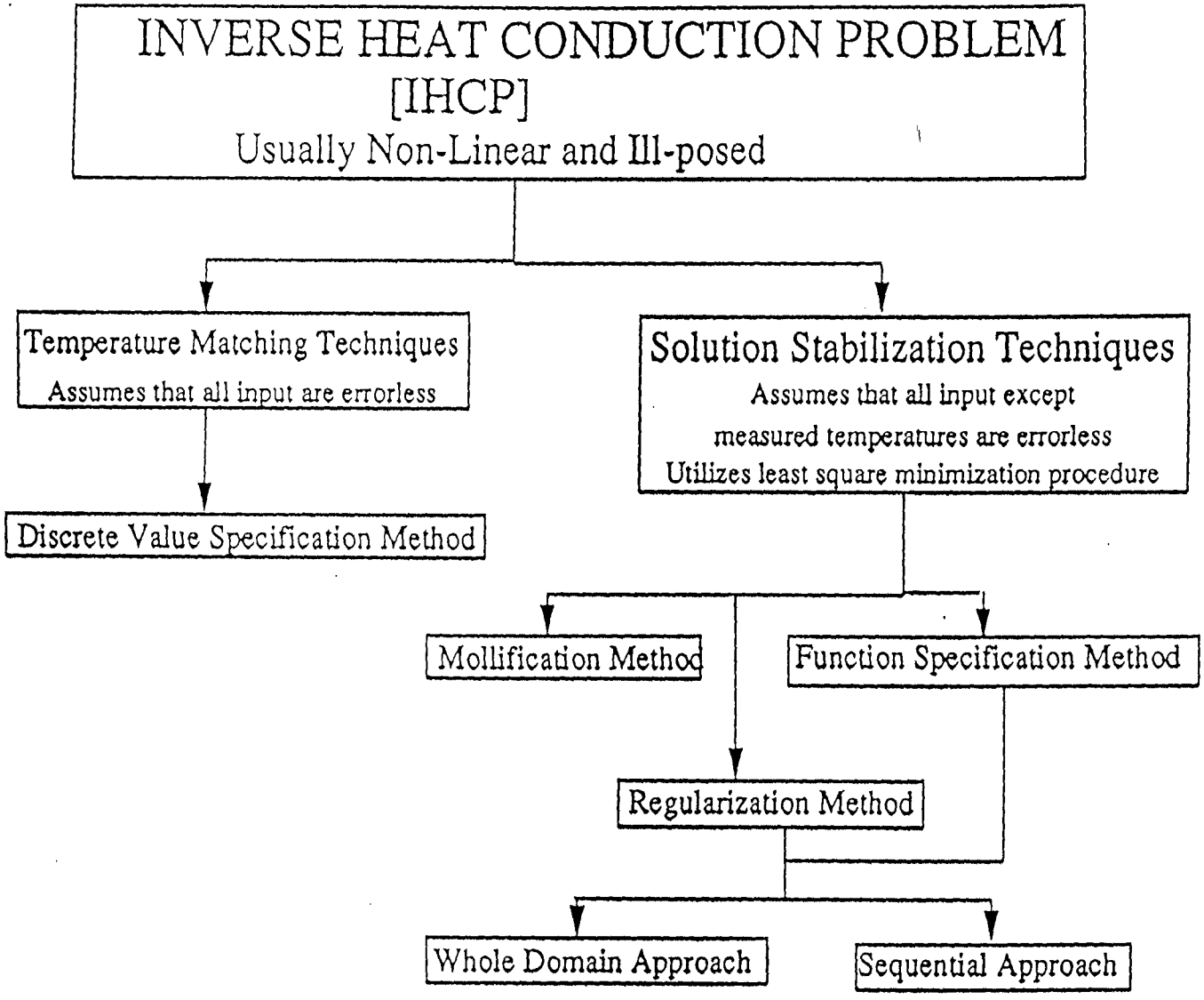

Fig. 1A Schematic illustration of IHCP methods.

$$SC^m = \frac{dT^m}{dq^m} \tag{1A}$$

or

$$SC^m = \frac{dT^m}{dh^m} \tag{2A}$$

Applying this definition to Eq. (5.1), one obtains:

$$\frac{\partial}{\partial z}\left(k\frac{\partial SC}{\partial z}\right) = \rho C_p \frac{\partial SC}{\partial t} \tag{3A}$$

Initial and Boundary Conditions

1. Initial temperature of the chill is specified ($l_{ch/c} < z < l_{ch}$, $0 < r < r_0$, t=0)

$$SC = 0 \tag{4A}$$

2. At the chill hot face ($z = l_{ch/c}$, $0 < r < r_0$, t)

$$-k\frac{\partial SC}{\partial z} = 1 \tag{5A}$$

3. At the chill cold face ($z = l_{ch}$, $0 < r < r_0$, t)

$$SC = 0 \tag{6A}$$

Eqs. (3A) and (5A) were solved with the aid of implicit finite difference formulation similar to Eqs. (5.5) and (5.6).

$$\frac{\alpha\Delta t}{2\Delta z^2}SC_{i-1}^{m+1} - \left\{1 + \frac{\alpha\Delta t}{\Delta z^2}\right\}SC_i^{m+1} + \frac{\alpha\Delta t}{2\Delta z^2}SC_{i+1}^{m+1} =$$

$$\frac{\alpha\Delta t}{2\Delta z^2}SC_{i-1}^{m} - \left\{\frac{\alpha\Delta t}{\Delta z^2} - 1\right\}SC_i^{m} + \frac{\alpha\Delta t}{2\Delta z^2}SC_{i+1}^{m} \tag{7A}$$

At the chill hot face, Eq. (5A) becomes

$$-\left\{1+\frac{\alpha\Delta t}{\Delta z^2}\right\}SC_1^{m+1}+\frac{\alpha\Delta t}{\Delta z^2}SC_2^{m+1}=\frac{2\Delta t}{\rho C_p\Delta z}-\left\{\frac{\alpha\Delta t}{\Delta z^2}-1\right\}SC_1^{m}+\frac{\alpha\Delta t}{\Delta z^2}SC_2^{m} \qquad (8A)$$

Eqs. (7A) and (8A) can be linearized by assuming that for sufficiently small time steps, the thermophysical properties (ρ, k, C_p) do not exhibit any tangible changes from one time step to the next, even though there may be a large variation in such properties from one end of the body to the other. However, the use of small time steps frequently introduces instabilities in the IHCP solution and often require some form of restriction on the time dependence of the heat flux.

In the sequential method used here, it is assumed that the heat flux is temporarily constant for a carefully selected 'r' future time steps as illustrated in Fig. 2A.

$$q^m = q^{m+1} = q^{m+2} = \ldots\ldots\ldots\ldots = q^{m+r-1} \qquad (9A)$$

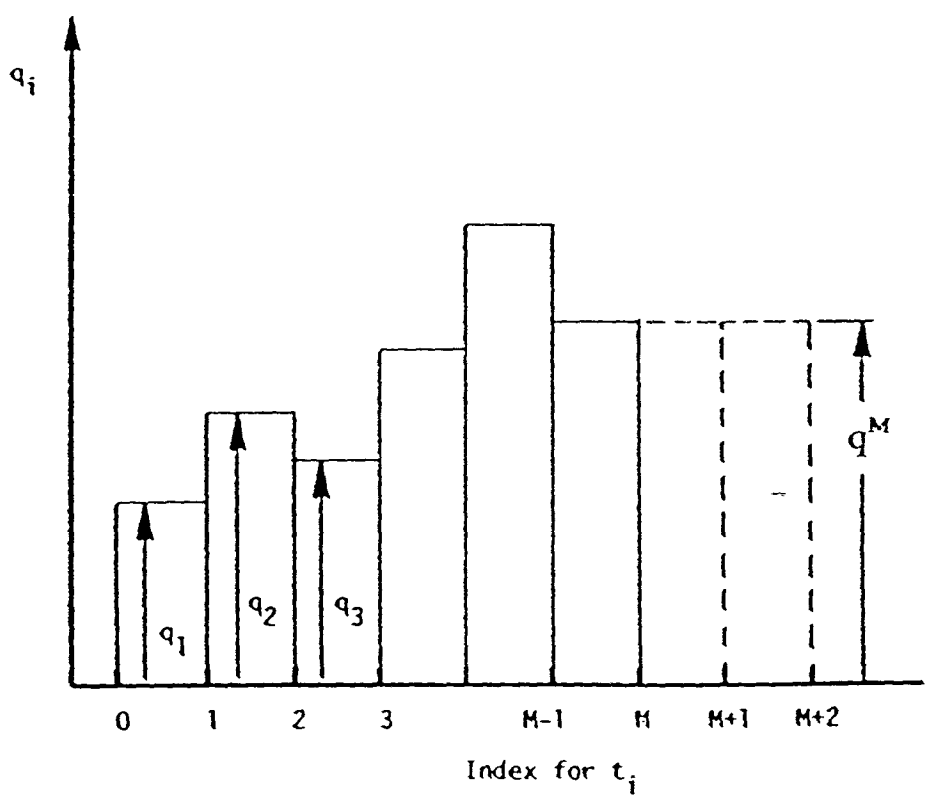

Fig. 2A Schematic illustration of the use of future time step in heat flux calculation.

The use of this future time steps in conjunction with the least square criterion enhances the stability of solution. The least square criterion in this case can be expressed in the form:

$$S_L = \sum_{i=1}^{r} \sum_{j=1}^{ns} (TM_j^{m+i-1} - TC_j^{m+i-1})^2 \tag{10A}$$

The function S_L is minimized with respect to heat flux q^m when

$$\frac{dS_L}{dq^m} = 0 \tag{11A}$$

so that

$$2 \sum_{i=1}^{r} \sum_{j=1}^{ns} (TM_j^{m+i-1} - TC_j^{m+i-1}) \left\{ -\frac{dTC_j^{m+i-1}}{dq^m} \right\} = 0 \tag{12A}$$

For $TC^m = f(q^m)$, the first two terms of the Taylor series expansion will yield

$$TC_j^{m+i-1} = TC_j^{m+i-2} + (q^m - q^{m-1}) \left\{ \frac{dTC_j^{m+i-2}}{dq^m} \right\} + \ldots. \tag{13A}$$

Substituting Eq. (13A) into (12A), the following expression results:

$$q^m = q^{m-1} + \frac{\sum_{i=1}^{r} \sum_{j=1}^{ns} (TM_j^{m+i-1} - TC_j^{m+i-2}) SC_j^{m+i-2}}{\sum_{i=1}^{r} \sum_{j=1}^{ns} (SC_j^{m+i-2})^2} \tag{14A}$$

since $\dfrac{dTC_j^{m+i-2}}{dq^m} = SC_j^{m+i-2}$

Equation (11A) is used to evaluate the heat flux at any given time step. The procedure for the implementation of the IHCP algorithm is shown in Fig. 3A. The sequence of solution involves obtaining the sensitivity coefficients employing Eqs. (6A), (7A) and (8A). The sensitivity coefficients are then utilized in computing the heat flux via Eq. (14A). The heat flux value obtained is finally used to evaluate the nodal temperatures with Eqs. (5.5) and (5.6). The procedure

is repeated when the time is incremented.

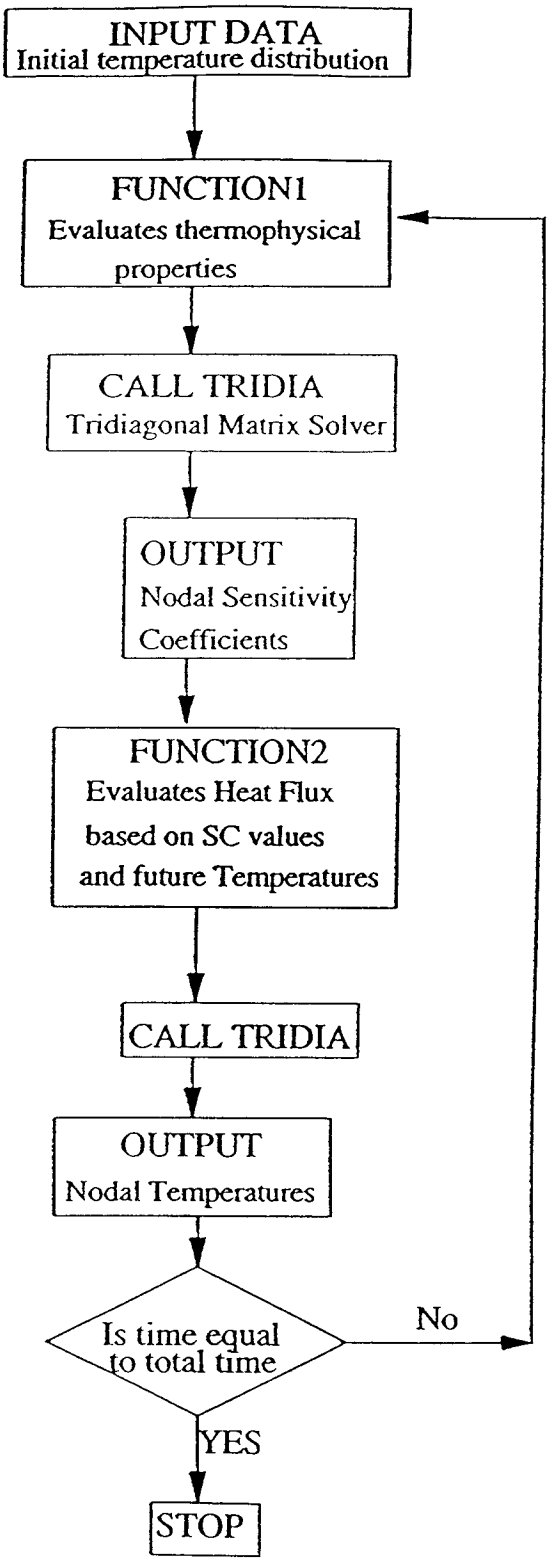

Fig. 3A Flow diagram of the sequential IHCP technique.